SCUOLA DI DOTTORATO
UNIVERSITÀ DEGLI STUDI DI MILANO-BICOCCA

Department of
Material Science

PhD program ***Material Science and Nanotechnology*** Cycle **XXXIII**
Curriculum in Material Science

HETEROSTRUCTURES BASED ON THE LARGE-AREA Sb_2Te_3 TOPOLOGICAL INSULATOR FOR SPIN-CHARGE CONVERSION

Surname **Longo** Name **Emanuele Maria**

Registration number **740619**

Tutor: **Prof. Marco Fanciulli**

Supervisor: **Dr. Roberto Mantovan**

Coordinator: **Prof. Marco Bernasconi**

ACADEMIC YEAR 2019/2020

Contents

Abstract

Spin-based electronic devices constitute an intriguing area in the development of the future nanoelectronics. Recently, 3D topological insulators (TIs), when in contact with ferromagnets (FM), have attracted huge interest in the context of the spin-to-charge conversion efficiency, with an efficiency in FM/TI heterostructures that is potentially higher than that of FM at the interface with heavy metals. The main subject of this thesis is the study of the chemical-physical interactions between the granular and epitaxial Sb_2Te_3 3D-TI with Fe and Co thin films by means of X-ray Diffraction/Reflectivity, Ferromagnetic Resonance spectroscopy (FMR) and Spin Pumping-FMR techniques. Beside the optimization of the materials properties, particular care was taken on the potential technology transfer of the presented results. Therefore, large-scale deposition processes such as Metal Organic Chemical Vapor Deposition (MOCVD) and Atomic Layer Deposition (ALD) were adopted for the growth of the Sb_2Te_3 3D-TI and part of the FM thin films respectively.

A thorough chemical, structural and magnetic characterization of the Fe/granular-Sb_2Te_3 interface evidenced a marked intermixing between the materials and a general bonding mechanism between Fe atoms and the chalcogen element in chalcogenide based TIs. Through rapid and mild thermal treatments performed on the granular Sb_2Te_3 substrate prior to Fe deposition, the Fe/granular-Sb_2Te_3 interface turned out to be sharper and chemically stable. The study of ALD-grown Co thin films deposited on top of the granular-Sb_2Te_3 allowed the production of high quality Co/granular-Sb_2Te_3 interfaces, with also the possibility to tune the magneto-structural properties of the Co layer through a proper substrate selection.

In order to improve the structural properties of the Sb_2Te_3, specific thermal treatments were performed on the as deposited granular Sb_2Te_3, achieving highly oriented films with a nearly epitaxial fashion. The latter substrates were used to produce Au/Co/epitaxial-Sb_2Te_3 and Au/Co/Au/epitaxial-Sb_2Te_3 heterostructures and the dynamic of the magnetization in these systems was investigated studying their FMR response. The FMR data for the Au/Co/Sb_2Te_3 samples were interpreted considering the presence of a dominant contribution attributed to the Two Magnon Scattering (TMS), likely due to the presence of an unwanted magnetic roughness at the Co/epitaxial-Sb_2Te_3 interface. The introduction of a Au interlayer to avoid the direct contact between Co and Sb_2Te_3 layers was shown to be beneficial for the total suppression of the TMS effect.

SP-FMR measurements were conducted on the optimized Au/Co/Au/epitaxial-Sb_2Te_3 structure, highlighting the role played by the epitaxial Sb_2Te_3 substrate in the SP process. The SP signals for the Au/Co/Au/Si(111) and Co/Au/Si(111) reference samples were measured and used to determine the effective spin-to-charge conversion efficiency achieved with the introduction of the epitaxial Sb_2Te_3 layer. The extracted SCC efficiency was calculated interpreting the SP-FMR data using the Inverse Edelstein effect and Inverse Spin-Hall effect models, which demonstrated that the Sb_2Te_3 3D-TI is a promising candidate to be employed in the next generation of spintronic devices.

Acknowledgments

Con questa tesi voglio cogliere l'occasione di ringraziare tutte le persone che negli ultimi tre anni di attività di dottorato sono state parte della mia vita lavorativa e non, poichè è anche grazie a loro che sono arrivato al termine di questo percorso.

Il primo grazie lo rivolgo al Dr. Roberto Mantovan e alla Dott.ssa Claudia Wiemer, i quali sono stati i miei responsabili scientifici nel corso della mia attività di ricerca. Loro mi hanno insegnato il mestiere del ricercatore nella maniera più diretta possibile, introducendomi fin dai primi tempi nel vivo delle attività di laboratorio, spronandomi a scrivere articoli scientifici, proposte di progetto e a partecipare a molte conferenze internazionali, dandomi la possibilità di conoscere un mondo fino a quel momento per me inesplorato. Li ringrazio inoltre per avermi insegnato a concretizzare i risultati ottenuti riponendo piena fiducia nelle mie capacità e lasciando spazio alle mie inclinazioni personali.

Un ringraziamento a tutto il personale scientifico e amministrativo del laboratorio CNR-IMM di Agrate-Brianza, con il quale ho instaurato un rapporto sereno e proficuo, rimasto tale a tutt'oggi. In particolare, vorrei rigraziare il Dr. Massimo Longo, il Dr. Raimondo Cecchini e il Dr. Martino Rimoldi per aver prodotto i campioni di Sb_2Te_3 studiati in questa tesi. Un grazie anche al nostro tecnico di laboratorio Mario Alia, il quale oltre ad aver contribuito alla produzione dell'innumerevole quantità di campioni che ho analizzato durante la mia attività di ricerca, ha saputo ascoltare le mie richieste con grande disponibilità e simpatia. Ringrazio anche profondamente il Dr. Matteo Belli che mi ha trasmesso le sue conoscenze sulle tecniche spettroscopiche di risonaza paramagnetica e ferromagnetica, seguendo con pazienza il processo di analisi dati e supportandomi nell'interpretazione degli stessi. Grazie anche al Dr. Francesco Caruso, mio compagno di scrivania, il quale ha realizzato artigianalmente alcune componenti della strumentazione "home-made" che ho utilizzato per i miei studi di risonanza ferromagnetica, supportandomi in alcuni dei momenti piu complessi di questa attività.

L'ultimo anno della mia attività di ricerca si è svolto principalemte nel Dipartimento di Scienza dei Materiali dell'Università degli Studi di Milano-Bicocca all'interno del laboratorio di ricerca del Prof. Marco Fanciulli, che colgo l'occasione di ringraziare per aver reso disponibili spazi e strumentazione. Un grazie anche alla Dr.ssa Fabiana Taglietti, che da collega e amica ha trascorso con me lunghi periodi in laboratorio, aiutandomi a configurare parte della strumentazione di misura e soprattutto sopportandomi per tutto il resto del tempo.

Il 2020 è stato un anno segnato dallo scoppio di una pandemia mondiale a causa del dilagare del coronavirus, condizione che ha stravolto le vite di tutti noi facendoci vivere un'esperienza surreale, che ha avuto un impatto enorme sulle nostre vite di tutti i giorni. Per poter affrontare tutto questo senza trascurare la mia attività di ricerca, il ruolo della mia famiglia è stato fondamentale. Per questo voglio ringraziare i miei nonni per essere sempre presenti dispensando sicurezza e amore incodizionati. Un grazie speciale va a mio padre, per il semplice fatto di essermi stato accanto da tutta la vita come solo un buon padre sa fare.

Grazie anche ai miei amici di una vita che, in particolare durante l'ultimo periodo di scrittura di questa tesi, mi hanno saputo motivare toccando i tasti giusti. Inutile tentare una lista di nomi perchè sono troppi e lascerei sicuramente fuori qualcuno.

L'ultimo ringraziamento, chiaramente non per importanza, lo rivolgo a Federica, la mia compagna di vita da ormai cinque anni che con me condivide ogni esperienza nel quotidiano. Grazie per ogni giorno passato insieme, grazie per la pazienza infinita che hai e grazie per gli spazi che hai saputo prenderti e lasciarmi. Non avrei sperato in una compagna migliore per tutto questo tempo.

List of Publications

Part of the scientific contents reported in this thesis appeared previously in the following scientific publications:

1. **E. Longo**, C. Wiemer, R. Cecchini, M. Longo, A. Lamperti, A. Khanas, A. Zenkevich, M. Fanciulli, R. Mantovan, *Chemical, structural and magnetic properties of the Fe/Sb2Te3 interface, Journal of Magnetism and Magnetic Materials.* 474 (2019) 632–636. https://doi.org/10.1016/j.jmmm.2018.12.009.

2. **E. Longo**, R. Mantovan, R. Cecchini, M.D. Overbeek, M. Longo, G. Trevisi, L. Lazzarini, G. Tallarida, M. Fanciulli, C.H. Winter, C. Wiemer, *ALD growth of ultra-thin Co layers on the topological insulator Sb2Te3*, Nano Res. 13 (2020) 570–575. https://doi.org/10.1007/s12274-020-2657-4

3. **E. Longo**, C. Wiemer, M. Belli, R. Cecchini, M. Longo, M. Cantoni, C. Rinaldi, M.D. Overbeek, C.H. Winter, G. Gubbiotti, G. Tallarida, M. Fanciulli, R. Mantovan, *Ferromagnetic resonance of Co thin films grown by atomic layer deposition on the Sb2Te3 topological insulator*, Journal of Magnetism and Magnetic Materials. 509 (2020) 166885. https://doi.org/10.1016/j.jmmm.2020.166885.

4. **E. Longo**, C. Wiemer, R. Cecchini, M. Longo, A. Lamperti, A. Khanas, A. Zenkevich, M. Cantoni, C. Rinaldi, M. Fanciulli, R. Mantovan, *Fe/Sb2Te3 Interface*

Reconstruction through Mild Thermal Annealing, Adv. Mater. Interfaces 2020, 2000905, https://doi.org/10.1002/admi.202000905.

5. M. Rimoldi, R. Cecchini, C. Wiemer, A. Lamperti, **E. Longo**, L. Nasi, L. Lazzarini, R. Mantovan, M. Longo, *Epitaxial and large area Sb 2 Te 3 thin films on silicon by MOCVD*, RSC Adv. 10 (2020) 19936–19942. https://doi.org/10.1039/D0RA02567D.

List of abbreviations

MOCVD - Metal Organic Chemical Vapor Deposition
ALD - Atomic Layer Deposition
PLD - Pulsed Laser Deposition
XRD - X-ray Diffraction
XRR - X-ray Reflectivity
ToF-SIMS - Time of Flight Secondary Ions Mass Spectrometry
AFM - Atomic Force Microscopy
MFM - Magnetic Force Microscopy
SEM - Scanning Electron Microscopy
TEM - Transmission Electron Microscopy
CEMS - Conversion Electrons Mossbauer Spectroscopy
FMR - Ferromagnetic Resonance
BFM - Broadband Ferromagnetic Resonance
VSM - Vibrating Sample Magnetometry
TI - Topological Insulator
GMR - Giant Magnetoresistance
TMR - Tunnel Magnetoresistance
STT - Spin Transfer Torque
MRAM - Magnetoresistive Random Access Memory
MTJ - Magnetic Tunnel Junction
CMOS - Complementary metal-oxide-semiconductor
SOC - Spin Orbit Coupling
DW - Domain Wall
RM - Racetrack Memory

SOI - Spin-Orbit Interaction
SCC - Spin-Charge Conversion
NI - Normal Insulator
RT - Room Temperature
OOP - Out-of-Plane
FM - Ferromagnet
NM - Normal Metal
IP - In-Plane
WAL - Weak Antilocalization
fcc - face-center-cubic
bcc - body-center-cubic
hex - hexagonal
hcp - hexagonal-closed-packed
MC - magnetocrystalline
GCPW - Grounded Coplanar Waveguide
SOT - Spin Orbit Torque
SP - Spin Pumping
SP - FMR - Spin Pumping Ferromagnetic Resonance
SHE - Spin Hall Effect
ISHE - Inverse Spin Hall Effect
EE - Edelstein Effect
IEE - Inverse Edelstein Effect
RF - Radio Frequency

Chapter 1

Introduction

Nowadays, the electronic industry, in order to fulfill the increasing demand of new and technologically advanced electronic devices, must face several challenges mainly concerning the volume production and the efficiency of those devices placed on the market. Thus, large-scale production methods and cutting-edge materials must be employed to reach the purpose. Industrial methods and material science advances are not the only elements needed to overcome the limitation of the today's electronic devices, because the exploitation of new physical paradigms turned out to be crucial to reach the goal. The building block of the conventional complementary metal-oxide-semiconductor (CMOS) electronics is the transistor. In a large part of the electronic devices based on the CMOS technology (i.e. the floating gate transistor), the electrons are stored and their charge exploited to create the binary logic states 0 and 1, which are at the base of the computational processes in the conventional electronic devices. In addition to the development of novel and thus more efficient materials, the main requirement for the CMOS technology evolution is the size reduction of the transistors, which consequently leads to the increasing of their density on a single chip. The number of transistors scaling as a function of the time is described by an empirical exponential relation known as the "Moore's law" (Fig.1.1).[1, 2] The latter describes how the newest electronic devices are progressively able to process a higher number of calculations per unit of time, thus been more powerful than the previous one. In addiction to the number of transistors, the performances of a chip are related also to other characteristics such as the number of logic cores, the working frequency of the clock and the power consumption. However, the progressive and very fast shrinking of the transistor size, necessary to fulfill the market request, is approaching its physical limit due to the quantum-mechanical phenomena taking place at the nanometric scale ($\sim 10^{-9} m$) and the industrial difficulties encountered for the production of nanoscaled devices. This condition is slowing down the exponential increasing of the electronic device power, fact which pushed the scientific community towards the investigation of innovative solutions.

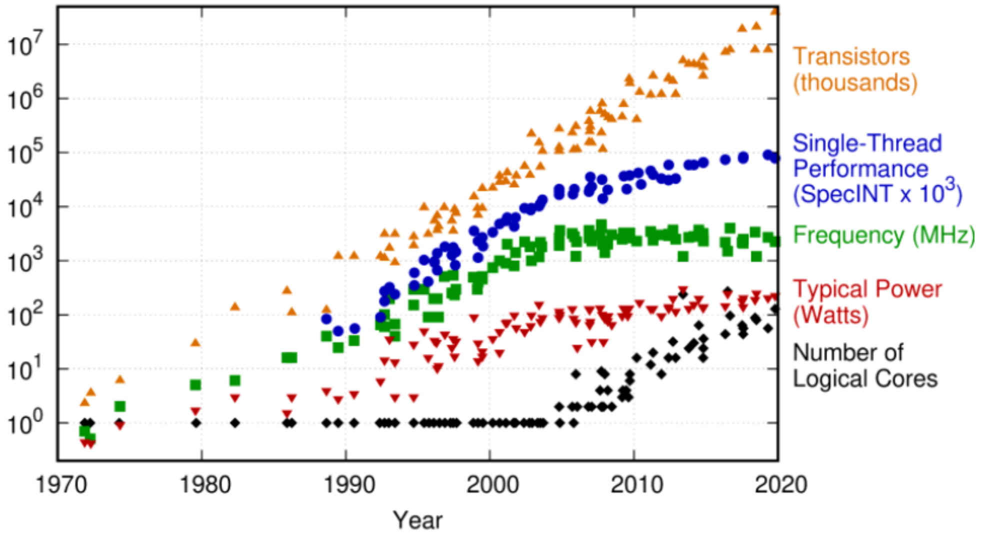

Figure 1.1: Plot of the the main technical features characterizing a microprocessor in the last 50 years represented in a semi-logaritmic scale. The exponential law for the number of transistors (yellow triangles) predicted by Moore in the 80's is reaching its limit, due to the physical constraints occurred in the transistors production. The original plot was created by M. Horowitz, F. Labonte, O. Shacham, K. Olukotun, L. Hammond, and C. Batten up to 2010 and by K.Rupp for 2010-2020.

In the last 50 years, in view of the so called *more than Moore scenario*, new electronic branches emerged, such as optoelectronics, spintronics, quantum computing, neuroelectronics and many others. Thanks to the research activity conducted in these fields, efficient, low-power and ultra-fast devices have been created and progressively introduced in the market. As an example we can count the quantum computer produced by Google, which began a reality in October 2019, or the Spin Transfer Torque – Magnetoresistive Random Access Memory (STT – MRAM), a spintronic device for the memory storage which is nowadays one of the most promising solutions to substitute the conventional electronic memories (i.e. Dynamic Random Access Memory, Flash memories) in the future.

In the next sections of this chapter the main theoretical concepts concerning the physical effects at the base of the modern spintronics will be presented, beside an introductory part concerning the properties of the materials under investigation in this thesis and their location in the related scientific panorama.

1.1 Spintronics

Since the ancient times, due to their controversial nature, the magnetic materials stirred up enormous interest in the people, which started to study their properties from the lodestones, naturally magnetized minerals (magnetite, Fe_3O_4) able to attract iron pieces.[3, 4] Subsequently, there was a transition from the use of a magnetized needle used in a compass to indicate the "true north" during the navigation in the sea (11-th century), to a comprehensive and revolutionary theory of the electromagnetism proposed by James Clerk Maxwell in 1864, which definitely reshaped the relationship between electricity, magnetism and speed of light. More recently, during the first decades of the 20^{th} century, a second scientific revolution took place with the introduction of the theory of quantum mechanics in the scientific panorama. Thanks to quantum mechanics the classical physics was replaced with a modern version of it, full of new and fascinating breakthroughs that in few decades deeply modified our daily life. Among them, the discovery of the intrinsic angular momentum of the electron - the electronic spin- is for sure one of the most important. Indeed, the existence of the spin gave the possibility to the researchers to exploit a further degree of freedom of the electron, in addition to its charge, condition which opened unbounded research and technological fields.

In the micro- and nano-electronics context, to enclose all the spin-related physical phenomena a new field emerged called *spintronics.* [5]In the late 80's, Albert Fert and Peter Grunberg independently discovered the Giant Magnetoresistance (GMR)in Fe/Cr heterostructures, a quantum mechanical effect associated to a relevant change in the electric resistivity of a ferromagnetic material when crossed by a spin-polarized electric current.[5] In properly designed electronic devices, the two regimes of resistivity (high and low) have been associated with the two logic states "0" and "1" and thus exploited for the first prototypes of innovative magnetically controlled electronic devices. This spin-dependent scattering processes deeply revolutionized the electronic industry, to such an extent that earned them the Nobel prize in physics in 2007.[6] The GMR can be considered as the ancestor of all the spintronic effects and its importance can be deduced by the number of industrial applications which are based on it. For instance, in the context of the memory storage, in place of the old devices based on the magnetic induction, the second-generation of the Hard Disk Drives (HDD) read heads used the GMR effect to read and write a single magnetic bit, tremendously improving the read/write speed and the memory density of the HDD memories. A sketch of an HDD read head is depicted in Figure1.2.

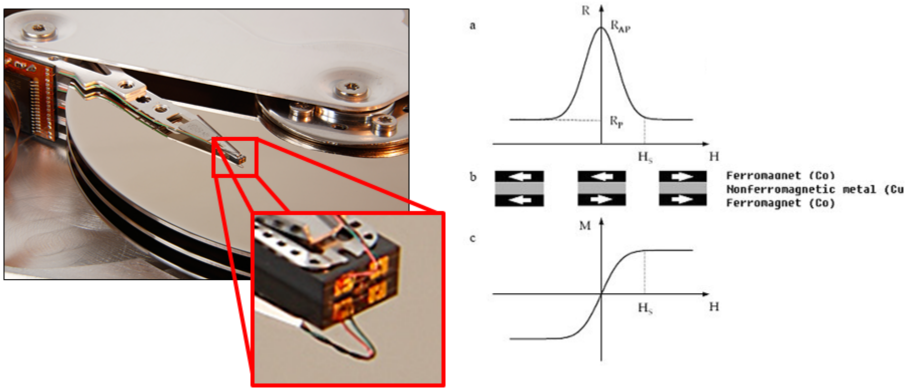

Figure 1.2: (Left) Inside of a commercial HDD memory and a zoom in of the read/write head. (Right) Resistivity (**R**) and magnetization (**M**) of a ferromagnet/normal metal/ferromagnet tri-layer as a function of the magnetic field. According to the mutual direction of the magnetization in the ferromagnetic film the **R(H)** and **M(H)** responses change in accordance to the GMR theory.

A further spin-dependent scattering process, similar to GMR, is called Tunnel Magnetoresistance (TMR), which exploits the electronic tunnel effect across an ultra-thin insulating layer sandwiched between two ferromagnetic layers, where the magnetization of one of them is switchable ("free layer") and one is fixed. The electronic device based on the TMR is known as Magnetic Tunnel Junction (MTJ). In a conventional MTJ the resistivity of the junction is different according to the mutual direction of the magnetization in the two ferromagnetic layers, thus defining two different logic states. The TMR was discovered for the first time by Jullier in 1975, who reported a 14% magnetoresistance gain in Fe/GeO/Fe heterostructures at 4 K. Nowadays, the TMR ratio between the parallel and anti-parallel configuration of the ferromagnetic layers reached the 600% at room temperature (RT) and more than 1000% at 4K in heterostructures where the insulation layer was substituted with MgO. [7] The TMR found its industrial application in memory storage devices such as the Magnetoresistive Random Access Memory (MRAM), memory cells in which the logic state is controlled by a MTJ. The MRAM cells are extremely faster than their electronic counterparts, the Flash memories, (more than 1000 times) and with a lower power consumption.

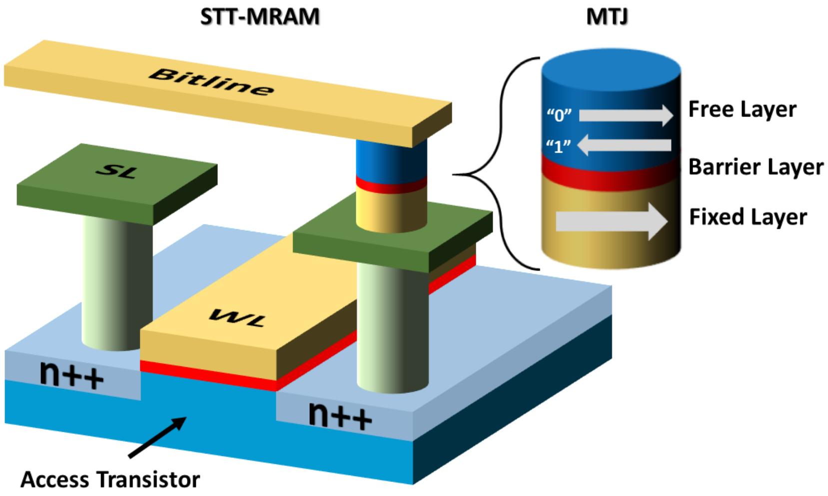

Figure 1.3: Artistic representation of a MTJ and its implementation in a STT-MRAM device. At the bottom of the STT-MRAM a conventional transistor is needed to control the current flow across the junction, limiting the scalability of the memory cell.

Despite these characteristics, MRAM is not the most efficient spintronic device, because the relatively high current needed to write its magnetic state requires additional power, and the presence of a transistor to control each cell affects its scalability. The Spin Transfer Torque – MRAM (STT-MRAM) overcomes this limitation. In a STT-MRAM device, the magnetization of a ferromagnetic layer is flipped using spin-polarized electronic current. Here, the fixed layer of a MTJ is used to polarize the spins of a charge current which is flowing into it, the same current that will subsequently transfer its angular momentum to the magnetization of the MTJ free layer modifying its orientation. The STT effect was reported for the first time in 1996 by the *Slonczewski et al.* paper. [8] As compared to the conventional MRAM cells, the STT-MRAM offers a lower switching energy, thus a lower power consumption, a slightly faster read/write process. However, some limitations occur also in this case, because the current density required to switch the magnetization of the free layer turned out to be detrimental for the devices endurance, making it comparable with the MRAM. A sketch of a MTJ and a STT-MRAM devices is reported in Fig.1.3. Moreover,a list of some relevant quantity to evaluate the efficiency of some of the memory storage devices present on the market are reported in Table 1.4.

Figure 1.4: Mainstream and emerging candidates for memory storage. Table taken from Ref.[9].

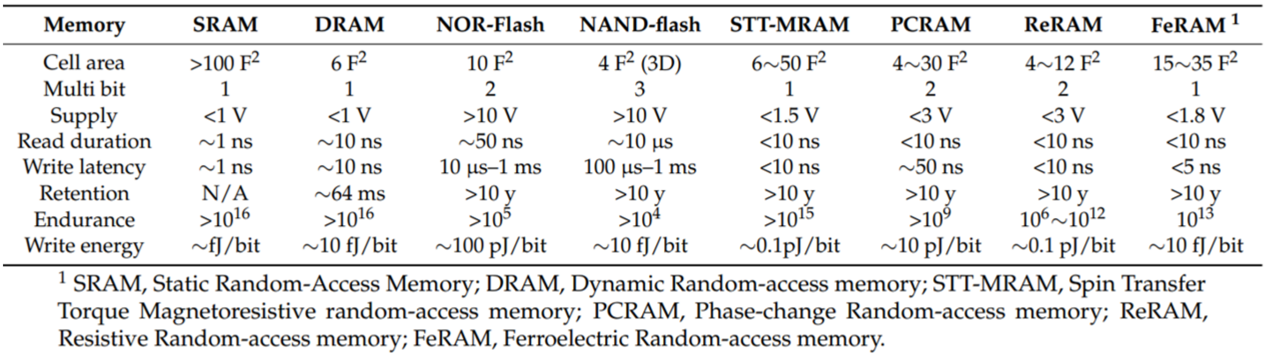

Memory	SRAM	DRAM	NOR-Flash	NAND-flash	STT-MRAM	PCRAM	ReRAM	FeRAM [1]
Cell area	>100 F^2	6 F^2	10 F^2	4 F^2 (3D)	6∼50 F^2	4∼30 F^2	4∼12 F^2	15∼35 F^2
Multi bit	1	1	2	3	1	2	2	1
Supply	<1 V	<1 V	>10 V	>10 V	<1.5 V	<3 V	<3 V	<1.8 V
Read duration	∼1 ns	∼10 ns	∼50 ns	∼10 µs	<10 ns	<10 ns	<10 ns	<10 ns
Write latency	∼1 ns	∼10 ns	10 µs–1 ms	100 µs–1 ms	<10 ns	∼50 ns	<10 ns	<5 ns
Retention	N/A	∼64 ms	>10 y	>10 y	>10 y	>10 y	>10 y	>10 y
Endurance	$>10^{16}$	$>10^{16}$	$>10^{5}$	$>10^{4}$	$>10^{15}$	$>10^{9}$	$10^{6}\sim10^{12}$	10^{13}
Write energy	∼fJ/bit	∼10 fJ/bit	∼100 pJ/bit	∼10 fJ/bit	∼0.1pJ/bit	∼10 pJ/bit	∼0.1 pJ/bit	∼10 fJ/bit

[1] SRAM, Static Random-Access Memory; DRAM, Dynamic Random-access memory; STT-MRAM, Spin Transfer Torque Magnetoresistive random-access memory; PCRAM, Phase-change Random-access memory; ReRAM, Resistive Random-access memory; FeRAM, Ferroelectric Random-access memory.

All the above mentioned memory storage devices can be considered as a collection of two-dimensional arrays of (2D) transistors and magnetic junctions ordered with a specific architecture. For the most of the time the 2D architecture has been considered as the most promising approach for a faster and cost effective size reduction of the single memory cell. But a different solution emerged a decade ago, a 3D structure called "*racetrack*" memory (RM) which was proposed as a candidate for faster, energy efficient and ultra-scaled magnetic memory cells (Fig.1.5).[10]

A RM is constituted by a series of bended ferromagnetic nanowires in which magnetic domains are magnetized in opposite directions forming the magnetic bits. The boundary regions between two magnetic domains are called *domain walls*(DW) and the space occurring between two DWs represents the size of the magnetic bit. By using pulses of spin-polarized currents it is possible to move coherently the whole pattern of DWs along the nanowire length, bringing them in specific regions where the information can be read or written. Studies to improve the RM performances are still in course as demonstrated by recent works. [11] More recently, ultra-thin films showing perpendicular magnetic anisotroy (PMA), such as CoFeB, have been proposed as a step toward narrower DW when compared to in-plane magnetic anisotropy (such as Permalloy).[11–15]

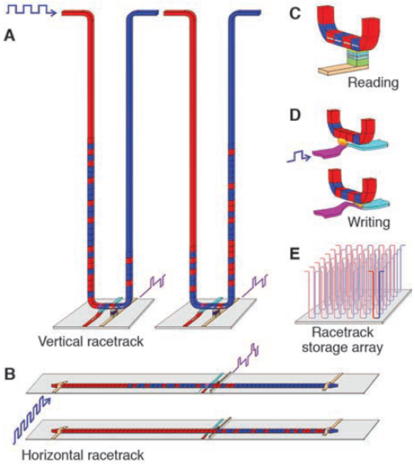

Figure 1.5: In (a) and (b) respectively the vertical and horizontal RM configuration are represented. Here the red and blue colors indicate the opposite magnetized magnetic domains. (c) and (d) shows a sketch of the reading and writing processes of a RM. (e) Example of an arrangement of vertically organized RMs forming a storage array. Figure taken from Ref. [10].

Writing is the problem...

In a magnetic device the writing process of a logic state is accompanied to a loss of a certain amount of energy, which depends on the working principles at the base of the specific device. As we mentioned above, the evolution of the spintronic devices (from the GMR to the STT) pointed towards more energy effective "magnetic writing" of an information. As it is clear by examining the physics behind the proposed magnetic devices, the key point to improve their performances is a combination between the geometrical and physical aspects, which somehow are always related to the interfaces between materials. Indeed, beside the introduction of new geometries and innovative chip architectures, the study of the physical phenomena at the interface between ferromagnetic materials and non-magnetic metals (NM) plays a central role in the modern spintronics. Recently, it has been observed that pure spin currents can be generated inside NM materials through the *spin-Hall effect* (SHE).[16–19] In the SHE a charge current flowing inside a NM is converted into a spin-polarized current as a consequence of spin-orbit interactions (SOI) and a pure spin-current is generated perpendicularly to the current flow. By controlling the intensity and the direction of the charge current also the direction and the intensity of the spin-current can be controlled. The magnetic momentum carried by latter spin-current can be transferred into an adjacent magnetic layer with the aim to manipulate its magnetization and such effect is called Spin Orbit Torque (SOT)[20, 21]. The discovery and the engineering of the conversion mechanisms between a charge current into a pure spin current taking place at the interface between magnetic and NM materials constituted a starting point of a new era of low power, ultra-fast and highly scalable spintronic devices. Being the SOI more intense in materials with high atomic number (SOI $\propto Z^4$) , the first attempts to exploit the SOT effect have been made with Heavy Metals(HM)/Ferromagnets (FM) heterostructure.[22, 23]. More recently, a new phase of condensed matter was theorized and discovered, [24] giving rise to a new class of topological materials.[19, 24–26] Among them, topological insulators (TIs) are nowadays one of the most promising candidates for the future spintronics.[27, 28] Many works demonstrated that, due to the exotic properties of TIs, in TI/FM heterostructures it is possible to obtain a higher spin-to-charge conversion (SCC) efficiency as compared HM/FM bilayers.[16] In the Khang *et al.*(2018)[29] paper an example of the ultra-low current density that can be used to control the FM magnetization through SOT in FM/TI systems is provided. Here, for a MnGa(3 nm)/BiSb(5 nm) patterned heterostructure an average critical current of $J = 1.5 \times 10^6 A\ cm^{-2}$ was demonstrated to switch the MnGa magnetization. The observed current density is found to be one or two order of magnitude lower than in similar MnGa/HM systems ($J \sim 10^7 - 10^8 A\ cm^{-2}$).

Despite a large number of scientific reports about the SOT mechanisms, the huge variety of magnetic effects arising at the interface between magnetic and NM thin films still needs to be completely understood. Moreover, the manipulation of the magnetization through spin-polarized charge currents is not limited to ferromagnetic materials, but on the contrary also anti-ferromagnetic and ferrimagnetic materials can be adopted for the same purpose, opening other fertile and fascinating research areas.[30, 31] Moreover, beyond TIs and HMs, other novel functional materials demonstrated to posses great potentialities for applications in spintronics. The most relevant are for sure the Weyl-semimetals, a transition metal dichalcogenide class of topological materials whose properties can be exploited similarly to TIs. [32, 33]
The race towards the discovery of the best materials able to maximize the SCC at the interface between materials in nanoscaled electronic devices is just at the beginning, making the spintronics field a fertile soil for the future nanoelectronics.

1.2 Topological insulators (TIs)

In the recent years, the discovery of a new class of topological materials exhibiting exotic properties called TIs revolutionized the condensed matter physics by both the theoretical and practical points of view. The topology is a branch of mathematics describing the properties of objects which remain unchanged under the effects of smooth deformations. Usually, such properties are known as *topological invariants* and are labeled by integer number (i.e. the genus). In order clarify the meaning of a smooth deformation, people usually refer to the transformation of a "donut"(a toroid) into a cup, because the two objects possess the same topological invariant. Differently, it does not exist a smooth deformation able to transform a sphere into a cup, because of their different genus (Fig.1.6).

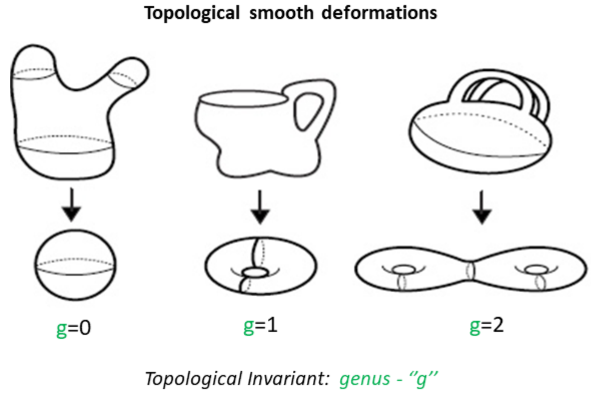

Figure 1.6: In this figure are represented some typical smooth deformations of various objects. Here, the topological invariant is called *genus* and can be roughly associated to the number of holes present in a single object. A transformation is smooth when applied between objects with the same genus. For instance, the sphere (g=0) cannot be smoothly transformed into a cup (g =1) because a hole should be created, causing a not allowed discontinuity in the transformation.

The same concept of a different topological invariant can be exploited to describe TIs and normal insulators(NI). Indeed, by crossing the interface of an hypothetical NI/TI bi-layer what happens is that the topological invariant of the system changes across the junction, thus the interface cannot remain insulating anymore, which is the physical analogous of a non-smooth deformation. As a consequence, the wave function of the electrons on the TI surface become delocalized giving rise to surface metallic states. It turns out that, in the specific case of 3D TIs, in the bulk of the material the band structure has an

insulating character and on the surface a conducting one.
The class of of TIs composed by bismuth and antimony chalcogenides, such as Bi_2Se_3, Bi_2Te_3 and Sb_2Te_3, is considered the second generation of TIs.[34–36] They are narrow-band-gap semiconductors with rhombohedral crystalline structure belonging to the R-3m space group. Being the TI Sb_2Te_3 the material studied in this thesis, all the properties described below refer to this family of TI.
The main unconventional electric properties of TIs are intimately related to their surface states. As reported in the Ando's review [26], the surface states in 2D and 3D-TIs can be depicted as in Fig.1.7. Here, the colored lines represent the boundary topological states, characterized by the so called *helical spin-polarization* or also known as *spin-momentum locking*.

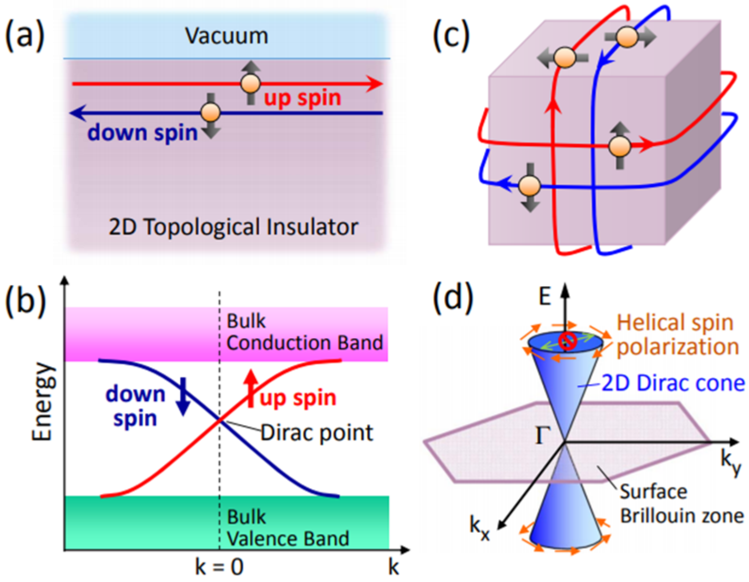

Figure 1.7: Representation of the boundary states in a TI with Dirac-like dispersion. In (a) and (b) the edge states of a 2D-TI and the surface states of a 3D-TI are represented respectively in the real space. The colored lines indicate the spin polarized topological conductive states. In (c) and (d) the energy dispersion of the 2D and 3D TI corresponding to (a) and (b) respectively. Figure taken from Ref. [26].

In the energy dispersion band schemes (Fig.1.7(c) and (d)), the valence and the conduction bands represent the dispersion of the insulating bulk states and the line lying in the bulk band-gap are the linearly dispersed surface states. For the 3D-TI case, the motion of the electrons flowing in such a states is described by the 2D Dirac equation, the same equation adopted to describe massless free fermions in relativistic quantum mechanics (Eq. 1.1). Here, v_F is the electron velocity at the Fermi level, k is the electron momentum, $\hat{z}$ is the unit vector perpendicular to the TI surface and $\hat{\sigma}$ the electron conductivity. Thus, it is usual to mention the energy dispersion of the surface states of 3D-TI as a 2D Dirac cone. As a consequence, the electrons motion across these conductive states is in principle dissipationless, representing one of the most important aspects in adopting TIs for the future ultra-low power nanoelectronics.

$$H_k = v_F(\hat{z} \times \hat{\sigma}) \cdot k \tag{1.1}$$

In Fig.1.7 the 2D and 3D representations of the surface state of a TI are reported. As depicted in the band scheme on the left of Fig.1.7, the red and green arrows indicate the spin of the electrons and that each surface state allows just a single spin orientation. As a consequence of the spin-momentum locking, according to the direction the charge current flowing across the surface states, at the Fermi level the spin degeneracy is removed and only a precise spin polarization is allowed. This characteristics is related to the topological protection of these surface states. Indeed, the electronic transport across the topological states is protected by the time reversal symmetry (no back scattering from **k** to **-k**, Fig.1.7(d) prohibition sign), which make these states robust against the disorder (i.e. dislocations, impurities, etc.) and consequently contributing in a dissipationless electronic conduction. However, the presence of magnetic disorder or the proximity with magnetic materials (e.g. ferromagnetic materials) can modify the topological nature of the TI, which is an important issue in developing spintronic devices based on FM/TI heterostructures.

1.3 Synthesis of TIs: state of the art

As outlined in Section 1.1 and 1.2, the integration of ferromagnetic thin and ultra-thin films with TIs is attracting high interest. The SCC effects arising at the interfaces between materials are at the base of the spintronic devices functionality, thus the production of high quality interfaces is required. Usually, in order to reach structurally ordered materials and chemically sharp interfaces, highly controlled physical deposition methods are adopted. The production of single-crystal TIs is mostly achieved by Molecular Beam

Epitaxy (MBE), an atomically controlled physical deposition process which assure a high crystal quality.[18, 37–40] Unfortunately, the conventional MBE facilities do not allow a straightforward industrial production of TIs, because of the relatively small deposition areas (typically max 1X1 cm^2) and the costly procedure.
In order to pursue the large-scale integration of electronic devices based on these new materials, the use of chemical processes is certainly of interest. When compared to physical methods, the latter are beneficial in terms of augmented deposition area and costs. Even if the chemically-driven growths are usually considered less efficient than the physical counterparts, recently highly controlled Atomic Layer Deposition (ALD) and Metal Organic Chemical Vapor Deposition (MOCVD) growths have been demonstrated to produce high quality TIs, sometimes with a nearly epitaxial order. [41, 42] Moreover, if applied to the deposition of FMs, the adoption of the ALD technique demonstrated how the use of chemical deposition methods facilitated the increase of the electronic devices performances, thanks to the highly pure deposited materials, their excellent conformality and the fine thickness control. [43] As will be discussed in Section 3.1.2 and 3.1.2.1, when compared with physical methods such as the Pulsed Laser Deposition (PLD), the inherent low energetics involved in a chemically-driven growth, could be advantageous for producing high quality interfaces.[44] So far, the use of the ALD in the field of spintronics has been scarcely proposed and very often focused on the growth of ultrathin oxide barriers in magnetic tunnel junctions. [45, 46] However, the use of ALD for the FM deposition could in principle give rise to defect-free FM/TI interfaces, which are obviously of particular interest to prevent spin-memory loss effects across the FM/TI interface. Not to be forgiven, due to the inherent absence of "shadows effect", a chemically-driven deposition can be the only viable solution for the development of complex 3D geometries.

Many aspects have to be considered for the description of the physical effects at the TI/FM interface and most of them are still not completely understood. In the next section a brief summary of the most relevant considerations about the TI/FM interfaces and the more classical HM/FM interfaces are reported.

1.4 Spin-Charge interconversion in spintronic systems

The interfacial spin transport and the relative SCC mechanisms at the interfaces of FM/TI and FM/HM systems can be studied using several techniques, which are based on as many physical effects such as SOT [20, 23, 47], spin Seebek effect [48], spin pumping (SP)[49, 50],etc. Moreover, similar studies can be extended on magnetic systems of different nature (i.e. antiferromagnets, ferrimagnets, ferroics materials, etc.), pushing the spintronic applications beyond the FM materials. Generally, for a deeper understanding of the physical aspects and for future applications in micro and nanoelectronics, a thorough evaluation of the interfacial SCC efficiency is required. In the above mentioned techniques and in many others, the SCC efficiency is obtained from the analysis of DC voltage signals (i.e. SP and SOT measurements) acquired in particular conditions (see Section 2.2.3.5). Here, the interpretation of the extracted data is generally based on two main physical effects and their reciprocal: the SHE/Inverse Spin Hall Effect (ISHE) [17] and the Edelstein Effect (EE)/Inverse Edelstein Effect (IEE) [51] (Section 2.2.3.5). In these SCC mechanisms a charge current is converted into a pure spin current (or viceversa) exploiting the properties of the bulk or of the surfaces/interfaces of a FM/NM systems. As it is explained further in Section 2.2.3.5, the SHE/ISHE exploits the bulk SOC to generate a spin accumulation at the boundaries of a thin NM film and, as a consequence, is more relevant in heavy materials (e.g. Pt, Pd, Ta, etc.). In the SHE/ISHE case, the SCC efficiency is associated respectively to the so called spin-Hall angle (θ_{SH})/Inverse Spin Hall Angle (θ_{ISHE}), a fundamental figure of merit for the estimation of the SCC efficiency in this context. Differently, the EE and IEE involve only the surface or interfacial states present in a FM/NM heterostructure and the relative SCC efficiency figure of merit is the EE/IEE length q_{EE}/λ_{IEE} (see Section 2.2.3.5). In this thesis we evaluated the SCC efficiency trough SP measurements, thus the ISHE and IEE are the figure of merit of interest in order to evaluate the SCC efficiency in the presented FM/TI systems.

As introduced in Section 1.2, TIs are heavy materials with spin-textured electronic surface states. For that, the SCC efficiency in TIs can be possibly enhanced by the presence of these states, providing a better solution as compared HMs. A careful characterization of the SCC efficiency in TI-based system is challenging. Indeed, disentangling the ISHE from the IEE in this materials is not straightforward, and requires detailed measurements. Indeed, in literature, for SP experiments conducted on a single FM/TI system, it is often given a double interpretation of the SCC mechanisms, both in terms of ISHE and IEE. For instance, in Jamali et al. (2015) [52] the authors used the ISHE model to interpret the SP data on CoFeB/Bi_2Se_3 systems, avoiding to isolate the contribution of the Bi_2Se_3 TSS. Here, for different structural quality of the Bi_2Se_3 substrate different θ_{SHE} were extracted in the range of 0.021 - 0.43. On the other hand, in the paper of Mahendra *et. al* (2019)[53], despite the similarities with the FM/TI system investigated in the Jamali's paper, the DC signal acquired from the $Co_{20}Fe_{60}B_{20}/granular - Bi_{43}Se_{57}$ heterostructure was interpreted in terms of IEE, even if, as declared by the authors, the λ_{IEE} evolution as a function of the $Bi_{43}Se_{57}$ thickness did not match the prediction of the IEE theory. The fact that such a similar systems are treated with different theoretical approaches by many research groups, makes the identification of a proper strategy in order to judge the efficiency of SCC in TI-based systems difficult. For that, also in this thesis a tentative interpretation of the SP measurements is given both in terms of ISHE and IEE (see Section 3.4).

A further critical issue for the extraction of the SCC efficiency in FM/NM systems is the adopted measurement technique. In principle, the possible methods (i.e. SOT, SP, etc.) used for the evaluation of the SCC efficiency should be all equivalent. However, in literature there is a huge discrepancy among values calculated with different methods for similar FM/NM systems. As it is reported by Wu *et al.*(2019) [38], the θ_{SHE} calculated for TIs in different configurations can vary from 0.047 to 425. The latter condition can have many origins. For instance, the position of the Fermi level in TIs is often not considered, but, as demonstrated in Ref.[38], it is strongly related to the nature of the conductive states involved in the SCC, thus strongly influencing its efficiency and the theoretical interpretation of the data. Another fundamental source of under- or overestimation of the SCC efficiency is for sure the intermixing between materials. Indeed, in several works a deep characterization of the interface quality is missing, despite the presence of elemental intermixing and morphological and magnetic interface roughness were largely demonstrated to have a central role for the determination of the SCC efficiency. [32, 52–57]

In order to investigate on the role of the intermixing in FM/TI systems, many groups tried to decouple the FM/NM interface introducing an interlayer between the FM and NM layers. For instance, in the seminal work of Roja-Sanchez et al. (2016)[49] the introduction of a Ag interlayer in the Au/Fe/Ag/$\alpha - Sn$ structure was demonstrated to be beneficial for enhancing the SCC efficiency in this system, reporting a $\lambda_{IEE} = 2.1$ nm extracted by SP measurements at RT. This value is quite large as compared several systems without interlayer. As an example, in the Mahendra's paper (2019) [53] $\lambda_{IEE} = 0.32$ nm and in the the Mendes *et al.* (2017) [58] and (2018) [59] papers $\lambda_{IEE} = 0.075$ nm and λ_{IEE} = 0.4 nm for $(Bi_{0.22}Sb_{0.78})_2Te_3$ and MoS_2 materials respectively. Similar estimations of the SCC efficiency are reported in a very recent paper of Bonell *et al.* (2020) [60], where a thorough study on the SOT response in different Py/Interlayer/$(Bi, Sb)_2Te_3$ systems has been reported. Here, the introduction of different metallic spacers (i.e. Te, Ag, Al) with different thicknesses has been demonstrated to dramatically enhance the SCC efficiency in these systems, likely due to the suppression of the interface intermixing and band-bending. In the latter work a particular care is given in the chemical-structural description of the Py/Interlayer/$(Bi, Sb)_2Te_3$ interfaces, evidencing the criticalities concerning the Te out-diffusion from the $(Bi, Sb)_2Te_3$ substrate. Similar considerations on the Te interdiffusion in Fe/Sb_2Te_3 (antimony telluride) structures are also discussed in this thesis, together with a strategy to eliminate or dramatically reduce this effect. As emerged from the latter considerations, the theoretical description and the experimental studies of FM/TI systems for the optimization of the SCC efficiency are not trivial.

Given the above summarized scientific context, one of the main focus of this thesis is to provide further insights on the benefits and the criticalities of both physical and chemical deposition methods for the production of high quality FM/TI heterostructures to optimize the SCC at the FM/TI interface. In Sections 3.1 and 3.2, the focus is on the coupling between the Sb_2Te_3 3D-TI with ferromagnetic Fe and Co thin films, with particular care on the description of the interface between the materials. Aware about the importance of the possible industrial transfer of the studied technology, almost the entire samples production has been performed using large-scale deposition processes (4 inch wafers), as discussed in Chapter 2. Moreover, in Chapter 3 a description of the magnetization dynamic in Co/Sb_2Te_3 and Co/Au/Sb_2Te_3 heterostructures is provided, together with the estimation of the SCC efficiency in these systems trough SP measurements.

Chapter 2

Experimental Techniques

2.1 Samples Preparation

The growth methods adopted for the production of the samples analyzed in this thesis are reported below. For each material a dedicated explanation of the specific deposition technique is reported, highlighting the main pros and cons and the eventual collaboration with external groups. My personal contribution for the samples synthesis was different according to the material. In the case of the production of Sb_2Te_3 substrates, I assisted the work of my colleagues growers by measuring the chemical-structural properties of the materials by XRD/XRR measurements. The ALD deposition of Co thin films was performed directly by me during a two months at the Wayne State University in Detroit, where I was introduced in the use of the ALD reactor present in the laboratory. For the optimization of Fe and Co thin films deposited by e-beam evaporation in our home laboratory, I followed for several months the activity of our technician by performing XRR/XRD and FMR measurements in order to identify the best growth parameters.

2.1.1 MOCVD of TI

As demonstrated in several works [36, 61], the topological properties of the Sb_2Te_3 TI are related to its chemical-structural nature, thus during the optimization of the Sb_2Te_3 thin films deposition several attempts have been made to improve their crystalline quality and surface flatness. In particular a proper selection of substrates and pre- and post-thermal treatments have been performed in order to obtain the best chemical-structural

quality, as will be discussed in Section 3.2.1.
The whole Sb_2Te_3 production has been entirely carried out at the CNR-IMM Unit of Agrate Brianza (Italy) laboratory using the thermal reactor Aixtron AIX 200/4 MOCVD tool equipped with an IR-heated 400 rotating graphite susceptor. The precursors adopted for the MOCVD processes were provided by Air Liquid Electronics.
Within this thesis activity, the Sb_2Te_3 thin films are grown on top of two different substrates, the amorphous SiO_2/Si and the crystalline Si(111), which are found to tune the Sb_2Te_3 structural properties, starting from a granular continuous film (Section 3.1.1) towards an epitaxial one respectively (Section 3.2.1).
A polycrystalline, granular and structurally continuous 30-35 nm thick Sb_2Te_3 thin film is grown on top of SiO_2/Si substrates by using the antimony trichloride ($SbCl_3$) and bis(trimethylsilyl)telluride (Te$(SiMe_3)_2$) electronic grade precursors at RT, where the low-temperature deposition is reached by the Lewis hard-soft acid-base reactions. Here, the deposition pressure is maintained at 50 mbar and deposition time is 60 min long.
In the case of the Sb_2Te_3/Si(111) structures, prior to the Sb_2Te_3 deposition, the Si(111) substrates is treated with HF(5% in deionized H_2O) for 3 min, rinsed with deionized H_2O and dried with N_2. Subsequently, the samples is quickly loaded into the atmosphere controlled glove box of the MOCVD chamber. Once again, the $SbCl_3$ and Te$(SiMe_3)_2$ precursors are adopted and loaded into bubblers thermalized at 20.0 ± 0.1 °C and delivered to the MOCVD chamber through a vapor-saturated ultra-pure N_2 carrier gas. The depositions are carried out at 25 °C for 90 min at 15 mbar pressure, with a total flow of 5.575 l min^{-1}, and setting the precursors vapor pressures at 2.28 and 3.32 $\times 10^{-4}$ mbar respectively for $SbCl_3$ and Te$(SiMe_3)_2$. In order to obtain the best crystalline quality, the Sb_2Te_3 films were subjected to two thermal processes. The first one is carried out prior to the Sb_2Te_3 deposition on the Si(111) substrate and performed in situ at 500 °C for 60 min at 20 mbar, with a total N_2 flow of 11.000 l min^{-1}. The second thermal treatment (post-growth) is performed in situ on the pre-annealed Sb_2Te_3/Si(111) structure according to the following recipe: (1) heating ramp: 5.575 l min^{-1} N_2 flow, 900 mbar, from RT to 300 °C in 10 min; (2) annealing: 5.575 l min^{-1} N_2 flow, 900 mbar, 300 °C, 15 min; (3) cooling ramp: 1.500 l min^{-1} N_2 flow, 990 mbar, from 300 °C to 200 °C in 20 min, from 200 °C to 100 °C in 35 min, from 100 °C to 50 °C in 20 min. As a result, a 30 nm thick highly crystalline Sb_2Te_3 thin films are obtained.

2.1.2 Heavy Metals

The production of HMs is often performed by means of RF magnetron sputtering deposition, because of the high homogeneity and good crystals quality achieved with such technique. In the context of a short term scientific mission I performed during the 1st year of my PhD activity at the Winter Laboratory in the Wayne State University (Detroit - Michigan - U.S.), industrial Pt thin films have been used. The Pt substrates used are grown on top of a 12 inch wafer in a Pt(70 nm)/SiO2(100 nm)/Si stack and in this case the polycrystalline Pt film is mostly out-of-plane oriented along the [111] crystalline direction.

2.1.3 Synthesis of ferromagnetic thin films

2.1.3.1 Co by Atomic Layer Deposition

The Co films were grown at the Winter laboratory with a Picosun R-200 BE reactor for thermal ALD, connected to a in-house N_2 source and equipped with a SAES in-line purifier for a 99.99999% N_2 quality. The precursors used are the bis(1,4-ditert-butyl-1,3-diazadienyl)cobalt (Co(t-Bu2DAD)2),(1), and tertbutylamine(tBuNH2), (2), which favored a highly controllable ALD process in the 170–200 °C ALD thermal window.[62] The ALD of Co metal films is carried out by alternating a saturative pulsing sequence of (1) (4 s), N_2 purge (10 s), (2) (0.1 s) and N_2 purge (10 s) at 180 °C. We performed three different deposition runs of 100, 250 and 1.000 cycles. For each run a Co deposition on 1.5 cm × 1.5 cm samples is simultaneously deposited on top of the Sb_2Te_3(30-35 nm)/SiO_2(50 nm)/Si and the Pt(70 nm)/SiO_2 (100 nm)/Si substrates, which gives the possibility to investigate the effect of the substrate on the Co structural properties.

2.1.3.2 Fe by Pulsed Laser Deposition

In the context of a collaboration with the Moscow Institute of Physics and Technology (Dolgoprudny - Russian Federation) the Pulsed Lase Deposition (PLD) technique was exploited for the production of part of the Fe thin films investigated in this thesis. In particular, $^{54}Fe(10nm)/^{57}Fe(1nm)$ bilayers were grown at RT in a home-made setup with a base pressure of 10^{-6} Pa on granular Sb_2Te_3 substrates by using a YAG:Nd laser

($\lambda = 1064nm$) operating in the Q-switched regime ($\tau = 15ns$) with the variable output energy E= 50÷ 200 mJ and repetition rate $\nu = 5 - 50Hz$.

2.1.3.3 Fe and Co by e-beam Evaporation

The Edwards Auto306 e-beam evaporation facility is used for the growth of Au, Fe and Co thin films in the CNR-IMM Unit of Agrate Brianza laboratory. Here, a systematic activity is conducted in order to optimize the reliability of such deposition process, which led to the production of evaporated ultra-thin films (down to 2 nm) on top of multiple substrates (SiO_2, Pt, Sb_2Te_3). In all the processes the starting value of the vacuum in the deposition chamber is in the range of $5 \cdot 10^{-7} - 10^{-6}$ Pa. For each evaporated element the electronic gun deposition current and the value of the vacuum in the growth chamber during the process are: Au 120 mA - $7.8 \cdot 10^{-6}$ Pa; Fe 80 mA - $4.6 \cdot 10^{-6}$ Pa and Co 55 mA -$4.6 \cdot 10^{-6}$ Pa.

2.2 Measurement techniques

In this chapter the analysis techniques exploited for the chemical-structural and magnetic characterization of the samples investigated in this thesis are reported. The first and the second sections are dedicated to X-ray and ferromagnetic resonance based techniques, which constitute my main activity in the context of this thesis. In Section 2.2.4 a brief description of additional experimental methods employed to get a full understanding of the chemical, structural and magnetic properties of the materials of interest in this thesis are presented. I was personally not carrying out those measurements (Section 2.2.4), but I worked in a tight connection with the responsible researchers in order to fully comprehend the materials properties as it will be substantiated along the thesis (Chapter 3). For each complementary technique, the eventual collaboration with external research groups is also indicated.

2.2.1 X-Ray Diffraction

The chemical-structural quality of the samples is investigated by both X-ray Diffraction (XRD) and X-ray Reflectivity (XRR) techniques and conducted at the CNR-IMM Unit of Agrate Brianza.

The XRD patterns of the samples were acquired using an HRXRD IS2000 four circle goniometer equipped with a Cu K_α radiation ($\lambda = 1.5406Å$) and a curved 120° position sensitive detector (Inel CPS-120)(Fig.2.1(a)). During all the measurements the X-ray tube is maintained at 40 kV and crossed by a current of 9 mA. The high versatility of this instrument allows multiple measurement configurations such as the Grazing Incidence X-ray Diffraction (GIXRD), the XRD in Bragg-Brentano geometry (BBXRD) and the φ - scan XRD ($\varphi - XRD$).

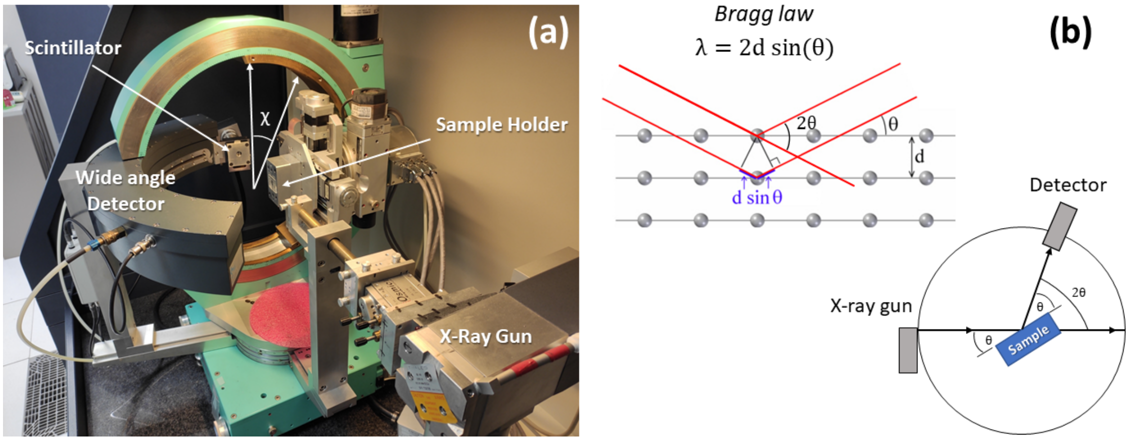

Figure 2.1: (a) Image of the HRXRD IS2000 four circle goniometer present in the CNR-IMM Unit of Agrate Brianza laboratory. (b) Sketch of the diffraction of X-ray by a crystal and configuration of a conventional XRD experiment.

In a GIXRD measurement a crystal is placed on the sample holder with an arbitrary orientation of the crystalline planes with respect the x-ray beam. Once the sample is properly aligned to reach the best sensitivity, in order to collect the signal from a larger sample volume, a small angle between the sample surface and the beam is established (ω) and the diffracted x-ray photons are collected, in this case, by the wide angle gas detector. If the lattice parameters a, b, c and the crystalline symmetry are known the instrument can be calibrated to observe specific (h, k, l) reflections, where h, k and l represent the Miller indices. Each set of indices represents a diffraction plane and a collection of characteristic diffraction planes constitutes a diffraction pattern, which can be associated to specific crystalline structures and materials. The diffraction process is essentially a scattering phenomenon between waves and the crystalline planes in a crystal lattice. When the X-ray waves travels inside the crystals they make different paths, and the difference in the length of these paths produces a difference in their phase. This phase difference leads to constructive and destructive interference between waves, thus only few waves escape from the sample giving rise to a diffraction peak. The diffraction process occurs when the wavelength of a wave is of the same order of magnitude as the periodical distance (d) between two centers of scattering (i.e. crystalline planes). This follows by the Bragg law, which links the X-ray wavelength λ, the distance between planes (d) and the X-ray beam incidence angle θ (Fig.2.1(a)), and it is generally written as

$$\lambda = 2dsin(\theta) \tag{2.1}$$

In order to properly interpret a generic XRD measurement, it is fundamental to highlight two main concepts: the incident beam, the diffracted beam and the normal to the reflecting plane are always coplanar; the angle between the diffracted and the transmitted beam is always 2θ and this is the real quantity measured during the experiments (Fig.2.1(b)). Indeed, in a conventional GIXRD pattern on the x-axis are reported the 2θ values and on the y-axis the intensity of the diffracted X-ray photons. The relationship defining the possible 2θ angles in which a crystal can diffract a X-ray beam is obtained combining the equation 2.1 with the plane-spacing equation, which is specific for each crystal symmetry. In this thesis we study materials with face center cubic (fcc) and hexagonal (hex) symmetry, thus the general relations which predict the diffraction angles for the cubic and the hexagonal crystals are

$$sin^2(\theta) = \frac{\lambda^2}{4a^2}(h^2 + k^2 + l^2) \quad Cubic \tag{2.2}$$

$$sin^2(\theta) = \frac{\lambda^2}{3}\left(\frac{h^2 + hk + k^2}{a^2}\right) + \frac{l^2}{4c^2} \quad Hexagonal \tag{2.3}$$

Further relations used in this thesis define the angle ϕ between two generic crystalline planes (h_1, k_1, l_1) with spacing d_1 and (h_2, k_2, l_2) with spacing d_2. The following are the expressions for the cubic and hexagonal cases

$$cos(\phi) = \frac{h_1h_2 + k_1k_2 + l_1l_2}{\sqrt{(h_1^2 + k_1^2 + l_1^2)(h_2^2 + k_2^2 + l_2^2)}} \quad Cubic \tag{2.4}$$

$$cos(\phi) = \frac{h_1h_2 + k_1k_2 + \dfrac{1}{2}(h_1k_2 + h_2k_1) + \dfrac{3a^2}{4c^2}l_1l_2}{\sqrt{\left(h_1^2 + k_1^2 + h_1k_1 + \dfrac{3a^2}{4c^2}l_1^2\right)\left(h_2^2 + k_2^2 + h_2k_2 + \dfrac{3a^2}{4c^2}l_2^2\right)}} \quad Hexagonal \qquad (2.5)$$

The GIXRD is a volume measurement in which a large portion of the sample is involved and, as a consequence, the information obtained must be interpreted as averaged over this volume.

The same principles introduced above for the GIXRD configuration are valid also for the XRD in Bragg-Brentano geometry. The difference here is that the incidence angle (or rocking angle) ω is no longer fixed but it is varied and only the symmetric reflections are collected (Fig.2.2(a)).

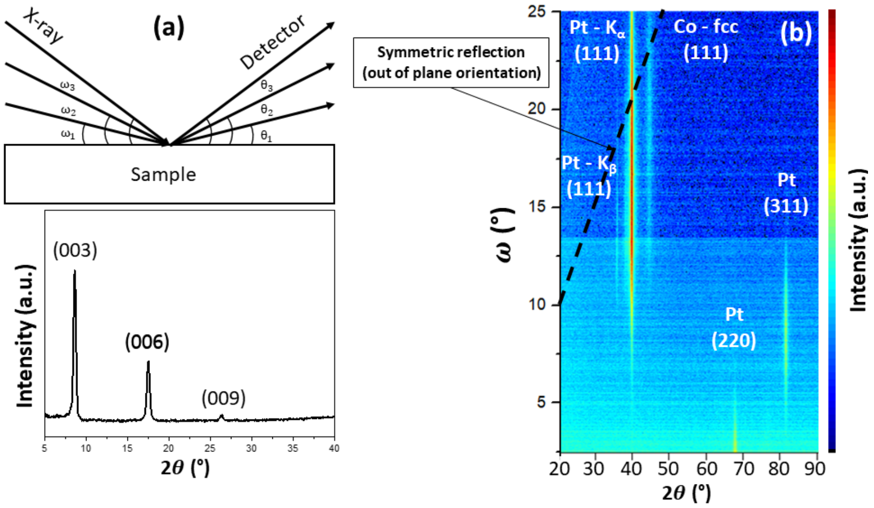

Figure 2.2: (a) Relative positions of an X-Ray beam and a single point detector in a Bragg-Brentano XRD measurement. In this configuration only the crystalline planes oriented along the out-of-plane direction can be detected and the XRD pattern below represents a generic pattern. (b) A BBXRD map acquired by the wide angle detector is reported for a Co(35 nm)/Pt(70 nm) bilayer.

A conventional BBXRD pattern has the same aspect as in GIXRD experiments, but in this configuration only the planes oriented along the out-of-plane (OOP) direction are diffracting, thus lying parallel to the sample surface (Fig.2.2 (a) below). In our specific case, we are not limited to the symmetric reflection, because for each ω value the wide angle detector collects the diffracted photons over a 120° angle, forming an XRD map which gives access to the so called *non-symmetric* reflections. An example of a BBXRD pattern of a Co(35 nm)/Pt(70 nm) bilayer is reported in Fig.2.2(b). In this BBXRD map, the ω and 2θ value are reported respectively on the x- and y- axes. For each ω value a 120° wide XRD pattern is collected. Here, the Bragg-Brentano condition is fulfilled only when $\omega = \theta$, condition which is represented by the dashed line in Fig.2.2(b). According to the theory, for a single crystal sample the Bragg-Brentano signal on a BBXRD map should be indicated by points lying on the Bragg-Brentano line. On the contrary, in Fig.2.2(b) there are broadened lines. The angular extension of such a broadening represents the deviation of the planes orientation from the OOP direction and it is called *mosaicity*, which provides a more detailed picture of a crystalline structure.

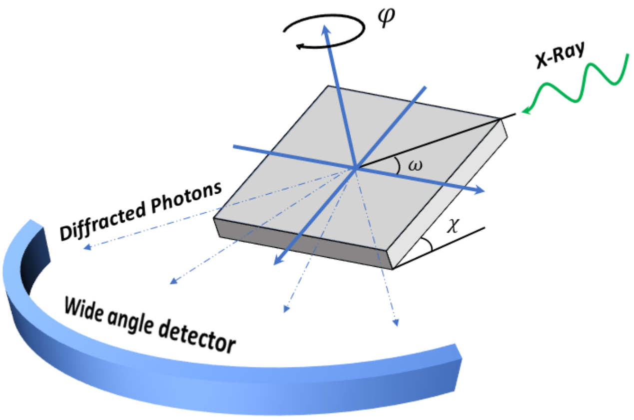

Figure 2.3: Generic representation of the mutual positions between the X-ray beam, sample and detector in a $\varphi - XRD$ measurements. Once the ω and χ angles are fixed, the sample is rotated of an angle φ and the diffracted photons are collected. In this configuration the in-plane orientation of the crystalline grains present in a film can be identified.

Similarly to the BBXRD, the $\varphi - XRD$ is exploited to investigate on eventual in-plane (IP) orientation of a film.[42, 63] In this configuration, the sample is rotated around an axis pointing towards a specific OOP orientation as depicted in Fig.2.3. A common practice in this kind of measurements is to place the sample in a very specific position where possibly a strong reflection is present. Usually, a main diffraction peak present in the XRD pattern is chosen to ensure an intense signal. During this procedure an ω and χ alignment is performed, where the χ angle is indicated both in Fig.2.1(a) and Fig.2.3. After this, the φ scans are recorded, one for the film and one for the substrate. Once the mutual position of the peaks between the film and the substrate is defined, it is possible to determine if any IP preferential orientations of the film are present with respect to the substrate and, consequently, the epitaxial relations can be determined.

2.2.2 X-Ray Reflectivity

When the X-ray are employed to study samples composed by layered thin films, they allow also the determination of the thickness, roughness and electronic density of each layer composing the stack. To describe the interaction between a sample and an X-ray beam impinging on its surface, similar consideration applicable for optics with the visible light can be done. A generic X-ray beam is an electromagnetic radiation with wavelength of the order of 1Å and, similarly to optics, the most relevant parameters to take into account are the wave vector $k = \frac{2\pi}{\lambda}$ and the index of refraction n, defined as

$$n = 1 - \delta + i\beta \tag{2.6}$$

where

$$\delta = \frac{\lambda^2}{2\pi} r_e \rho_e \tag{2.7}$$

and

$$\beta = \frac{\lambda}{2\pi} \mu_x \tag{2.8}$$

Here, $r_e = 2.818^{-15}m$ is the classical radius of the electron, ρ_e in the electron density of the material and μ_x the absorption length. Usually, δ is bigger than β, thus the latter is often neglected in the calculations. δ is related with the so called critical angle (θ_c) which is defined by the relation

$$cos(\theta_c) = n = 1 - \delta \tag{2.9}$$

In a XRR measurement the X-ray are reflected at the interface between the air ($n = 1$) and a material with $n < 1$ but anyway often close to the unit. As a result, $\delta \sim 10^{-5} - 10^{-6}$, thus typical values for θ_c are in the 0.1 - 0.5° range. Being δ small, the equation 2.9 can be approximated by using the Taylor expansion as $\theta_c = \sqrt{2\delta}$. If $\delta > 0$ consequently $n < 1$ and a phenomenon called *total external reflection* takes place for angles $\theta_i < \theta_c = \sqrt{2\delta}$ (Fig.2.4). Thus, in the simplified case of a single layer film, for angles $\theta_i > \theta_c$ it is possible to extract the electronic density of a layer using the equation

$$\theta_c = \frac{\lambda^2 r_e}{\pi}\rho_e \tag{2.10}$$

For a Cu K_α X-ray radiation a useful formula to convert the critical wave vector extracted from the fit of the collected data is

$$\rho_e = 711 q_c^2 \tag{2.11}$$

For the same single layer example, due to the interference effect occurring between X-ray reflecting from the surface and from the bottom of the layer, the thickness of the layer can be calculated measuring the angular distance between the maxima of the so called "Kiessig fringes" (Fig.2.4) by using the equation

$$d \approx \frac{\lambda}{2}\frac{1}{\theta_{m+1} - \theta_m} \tag{2.12}$$

In a real sample obviously the flatness of the layers is not ideal, but the presence of a surface roughness is observed. A rough surface gives rise to diffuse scattering effects which reduce the intensity of the specularly reflected beam. As a consequence, the Fresnel relation from an homogeneous slab, which links the X-ray wave vector component orthogonal to the sample surface (q_z) with the reflected beam (R_{q_z}), is corrected with an exponential part called Nevòt-Croce factor. In this context, the layers thickness is considered non-homogeneous and the roughness is included in the description introducing a Gaussian distribution of the thickness as the following equation

$$R^{flat}(q_z) = \left| \frac{q_z - \sqrt{q_z^2 - q_c^2 - \frac{32 i \pi^2 \beta}{\lambda^2}}}{q_z^2 + \sqrt{q_z^2 - q_c^2 - \frac{32 i \pi^2 \beta}{\lambda^2}}} \right| exp\left(-\frac{d}{2\sigma^2{}_m}\right) \tag{2.13}$$

where d and σ are respectively the average and standard thickness deviations. The argument exposed above to describe the XRR technique must be considered just a very general introduction of the argument. For real stratified materials the complexity of the structure requires the introduction of more complex models known as *dynamical theory of reflection.* For instance, in such a theory, the interfaces between materials are modeled themselves with a high number of layers with constant density, which is necessary to describe their continuous density profile. Here, the overall reflectivity response is obtained calculating the boundary condition of the electric and magnetic fields for each slab, which is mathematically represented by a product of matrices. For a more accurate description of both XRR and XRD techniques it is possible to refer to Ref. [64] and Ref. [65].

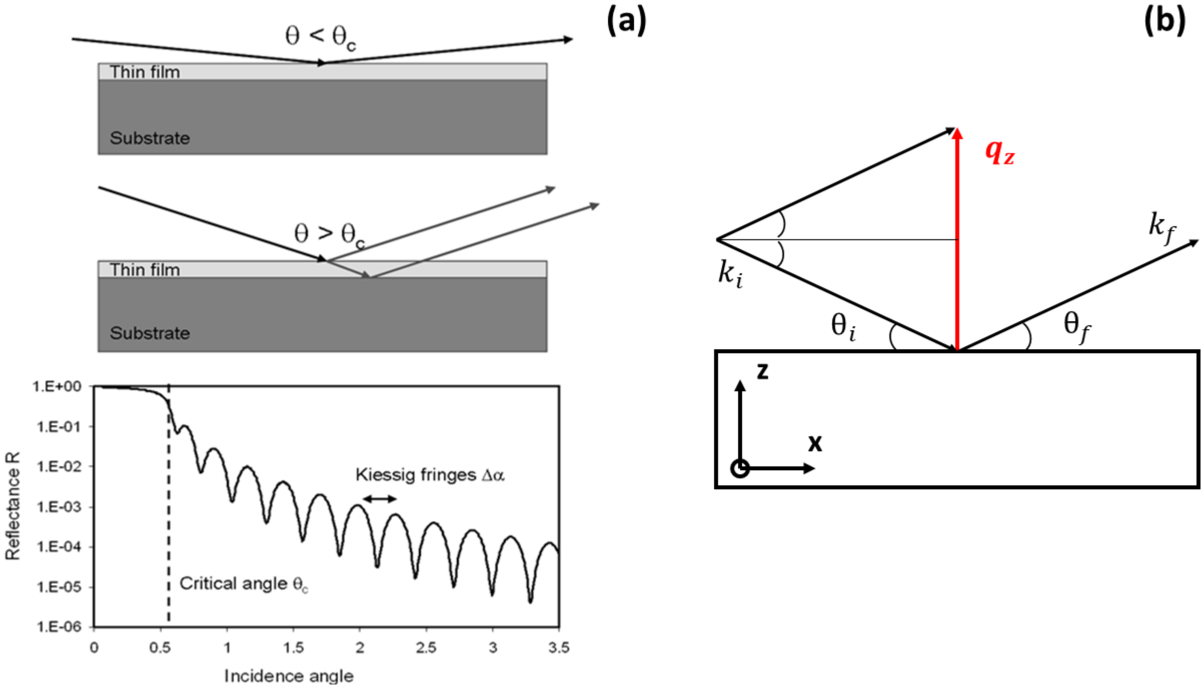

Figure 2.4: (a) Representation of the X-ray reflectivity in thin films. In the upper and central images are sketched the total reflection and the normal reflection of an X-ray beam impinging on a thin film surface. In the lower image an example of a typical XRR curve with indicated the critical angle θ_c is reported. (b) Reflection from an homogeneous slab of finite thickness. The wave vector k and its projection along the direction orthogonal to the surface are schematized.

2.2.3 Ferromagnetic resonance (FMR)

Ferromagnetic Resonance spectroscopy (FMR) is one of the most adopted methods to investigate the magnetization dynamics in magnetic materials. FMR provides multiple information, such as the direction and the intensity of the magnetization vector ($\vec{M}$), its magneto-structural quality , magnetic anisotropy and multiple energy dissipation effects. In the next sections, the theoretical background behind FMR is introduced, along with the experimental configurations of interest in the context of the present thesis.

2.2.3.1 Theoretical background

The description of the magnetic properties of ferromagnetic materials is generally a many body problem, where a quantum mechanical approach is required for an adequate physical description of the system. An effective strategy to override this constraint is provided by the so called *theory of micromagnetism*, a continuum theory which filled the gap between the empirical Maxwell's theory of magnetism and quantum theory. [66] In this theory, the fundamental quantity defining the magnetic state of a ferromagnet is the *magnetization* ($\vec{M}$). The modulus of ($\vec{M}$) is defined as $\mathbf{M} = \sum \frac{\vec{\mu}}{V}$, where $\vec{\mu}$ and V are the magnetic moment of a single atom and the volume of the magnetic medium. The atomic magnetic moment can be written as $\mu = \gamma S$, where S is the spin of the electron and γ the *gyromagnetic ratio*, which is related to the dimensionless Landè g-factor through the equation

$$\gamma = g\frac{\mu_B}{\hbar} \tag{2.14}$$

where $\mu_B = 9.274 \times 10^{-24} J/T$ is the Bohr magneton.

In magnetic materials the interaction between an external magnetic field with the spin of the electrons can generate a macroscopic magnetic polarization. In particular, in ferromagnetic materials when an external magnetic field is applied and subsequently removed, a net and spontaneous spin polarization is observed. This phenomenon can be explained analysing the contributions to the total magnetic energy density (E_{TOT}). In the next paragraphs the different contributions to E_{TOT} are discussed.

Zeeman energy The Zeeman energy (E_{Zeeman}) represents the interaction energy between an external magnetic field ($\vec{H}_{ext}$) and the magnetic moments in a magnetic body. Due to this energy term, a torque is exerted on the magnetic moments which minimizes the energy of the system when they are aligned parallel to the external magnetic field. The Zeeman energy can be expressed as the following integral over the volume of the magnetic body

$$E_{Zeeman} = -\mu_0 \int_V \vec{H}_{ext} \cdot \vec{M} dV \tag{2.15}$$

where μ_0 is the vacuum permeability. It is important to notice that the E_{Zeeman} is a fundamental contribution to the total magnetic energy, because it is the term that allows the manipulation of the magnetization in a FM through an external magnetic field, a central aspect for spintronic devices.

Exchange interaction energy The exchange interaction is the main responsible of the long-range magnetic order in a material and it essentially arises from the equilibrium of the electrostatic Coulomb interaction and the Pauli exclusion principle between electronic spins. Using the Heisemberg formalism the exchange energy (E_{ex}) is given by

$$E_{ex} = -\sum_{i<j} J_{ij} S_i \cdot S_j \tag{2.16}$$

where S_i and S_j represent the spin direction for the nearest neighbors spins and J_{ij} is the exchange integral, which is the energy difference between the parallel and the anti-parallel configuration of the spins.[67] When $J_{ij} > 0$ the ferromagnetic ordering is established and the energy minimum is reached for the parallel alignment of the spins. On the contrary, if $J_{ij} < 0$ is the anti-parallel spin configuration to be energetically favored, which is characteristic of anti-ferromagnetic (AFM) materials. When close to critical temperatures, the long-range magnetic order is dramatically compromised. The critical temperature of a magnetic material can be calculated from the magnitude of the J_{ij} integral and it is called Curie temperature (T_C) for FM and Néel temperature (T_N) for AFM. For a macroscopic description the exchange energy has to be expressed in its integral form as

$$E_{ex} = \frac{A}{M_s^2} \int (\vec{\nabla} \cdot \vec{M})^2 dV. \tag{2.17}$$

In this equation, A represents the exchange stiffness and M_s the saturation magnetization. It is important to notice that E_{ex} is isotropic in the space, thus for any volume dV and for any orientation of $\vec{M}$ the exchange energy is the same.

Demagnetizing field energy For a uniformly magnetized object the mutual interaction between magnetic dipoles (dipole-dipole interaction) generates an internal demagnetizing field (H_d), which contributes in the reduction of the total magnetic moment. The H_d field can be deduced by writing the relation

$$\vec{\nabla} \cdot \vec{M} \neq 0 \tag{2.18}$$

which is valid for the magnetic dipoles on the surface of a magnetic body. In the continuum approximation a magnetic dipoles density can be assumed and the demagnetizing energy density (or dipole-dipole interaction) can be written as

$$E_d = -\frac{\mu_0}{2} \int_V \vec{H}_d \cdot \vec{M} dV \tag{2.19}$$

The analytic expression of E_d is difficult to extract, because it depends on both the geometry and the magnetic state of the sample. Indeed, the magnetic field generated by E_d is also known as *shape anisotropy field* [C. Kittel and Solid State Physics] The magnetic samples studied in this thesis are all thin films, where the size of the specimen along the film plane is orders of magnitude bigger than its thickness. In this case E_d is

$$E_d = \frac{\mu_0}{2} (\vec{e_z} \cdot \vec{M}_s)^2 \tag{2.20}$$

where $\vec{e_z}$ is the unitary vector normal to the sample surface. From the latter relation it emerges that in magnetic thin films the magnetization has a preferential orientation which lies within the sample plane (*easy plane of magnetization*).

Magnetocrystalline anisotropy energy The crystalline structure of a ferromagnet influences the stationary position of the magnetization vector with respect to the symmetry of the crystal lattice. The magnetocrystalline anisotropy originates from the spin-orbit interaction between the spin and the orbital angular momenta of an electron subjected to the local electric field generated by the surrounding atoms, thus strongly depending on the atoms mutual position. As deeply discussed in M.Farle (1998)[68], the expressions for E_{MC} are often complicated and presented as a power expansion of the direction cosines of the magnetization vector with respect to specific directions of the crystal lattice. Also in this case, the direction of the magnetization in which E_{MC} has a minimum is called *easy axis* of the magnetization and, as the opposite, when E_{MC} reaches its maximum values is called *hard axis.* In some ferromagnets such as Co, the magnetization has one single direction for the easy/hard axis and in this case the expression for E_{MC} is given by

$$E_{MC} = \sum_n K_{u,n} sin^{2n}\theta \tag{2.21}$$

where $K_{u,n}$ (n = 1,2,...) are the constants of the uniaxial anisotropy. For an -hcp crystal lattice the angle θ is considered with respect to the c-axis of the unitary cell. For crystalline Co-hcp at RT typical values of the first two terms of $K_{u,n}$ are $K_{u,1} = 4.5 \cdot 10^5 J/m^3$ and $K_{u,2} = 1.5 \cdot 10^5 J/m^3$. In this thesis only polycrystalline ferromagnetic thin films are investigated, thus it was not possible to exploit any specific expression for E_{MC} straightforwardly. Therefore, the considerations regarding the magnetic anisotropy contribution are discussed during the exposition of the results.

Perpendicular magnetic anisotropy In magnetic thin films, a further relevant anisotropic contribution to the magnetic energy is the perpendicular magnetic anisotropy (PMA). As the thickness of the film becomes smaller the role of the surface starts to be relevant, inducing the direction of the magnetization to move from the in-plane direction, due to the shape anisotropy, towards an out-of-plane orientation.[68] The energy density contribution of PMA for in-plane magnetized samples generates the so called *out-of-plane magnetic anisotropy field*, which can be defined as

$$H_\perp = 4\pi M_s - \frac{2K_s}{M_s t_{film}} \tag{2.22}$$

where K_s is called *out-of-plane anisotropy constant.* In this thesis this equation covers a central role because several studies as a function of the FM thickness (t_{film}) are shown.

Total energy and effective magnetic field In order to have the overall depiction of the magnetic system, all the energy terms have to be summed, obtaining the total energy E_{TOT}. The expression for E_{TOT} can be generalized as

$$E_{TOT} = E_{Zeeman} + E_{ex} + E_d + E_{an} \tag{2.23}$$

where E_{an} encloses all the anisotropy terms, which can be more than those discussed above.[68] When the magnetization is uniform in the sample an effective magnetic field can be defined starting from E_{TOT} and it can be expressed as

$$\vec{H}_{eff} = -\vec{\nabla}_{\vec{M}} \cdot E_{TOT} \tag{2.24}$$

2.2.3.2 Magnetization dynamics

From the minimization of the magnetic energy of a ferromagnetic system the equilibrium condition for the magnetization can be achieved. When a ferromagnetic system is subjected to an external magnetic perturbation H_{eff}, the magnetization vector $\vec{M}$ changes its equilibrium state. The dynamics of $\vec{M}$ is described by the Landau-Lifshitz-Gilbert (LLG) equation [Eq.2.25], which correlates the temporal variation of $\vec{M}$ with the orientation of H_{eff}.

$$\frac{d\vec{M}}{dt} = -\mu_0\gamma\vec{M} \times \vec{H_{eff}} + \frac{\alpha}{\vec{M_s}}(\vec{M} \times \frac{d\vec{M}}{dt}) \tag{2.25}$$

The first term on the right-hand side of Eq.2.25 describes the dissipationless precessional motion of the magnetization vector $\vec{M}$ around H_{eff}, as represented in Fig.2.5. During its motion, $\vec{M}$ spins around the external magnetic field with a frequency called Larmor frequency (ω_L) defined as $\omega_L = \gamma H_{eff}$. In ferromagnetic materials, typical values for γ are in the range of $1.75 - 2.5 \cdot 10^7 Hz/Oe$. Eq.2.14 shows that γ is proportional to the g-factor which is dependent on the ratio between the spin (μ_s) and angular (μ_L) momenta in the magnetic material as

$$\frac{\mu_L}{\mu_s} = \frac{g-2}{2} \tag{2.26}$$

The value of the g-factor in ferromagnetic thin films can vary significantly from the bulk value as a consequence of the reduced symmetry of the system or due to possible intermixing effects between materials. The second term on the right-hand side of Eq.2.25 takes into account all the dissipative phenomena acting on the magnetization vector, which generate a spiraling motion of $\vec{M}$ towards the direction of the external magnetic field, with a relaxation time $\tau = 1/\gamma\alpha\mu_0 H_{eff}$ (Fig.2.5(b)).[68] Here α is called *damping constant* (or Gibert parameter) and it is the key parameter to study the dynamics of the magnetization in a ferromagnetic material. The relaxation effect which contributes in determining the value of α can be multiple. It does not exist a general theory able to decouple each dissipative contribution, thus complementary chemical-structural and magnetic experiment are demanding for a thorough understanding of a magnetic system. In Chapter 3.3 of this thesis, we focused the attention mainly on two aspects concerning the extraction of the damping constant: the chemical-structural quality of the studied materials and the so called *two magnons scattering effect*(TMS).[54] The chemical-structural inhomogeneities constitute a relevant scattering source for the magnetization vector during its precessional motion, and their role is discussed along the text in Chap.3.3.

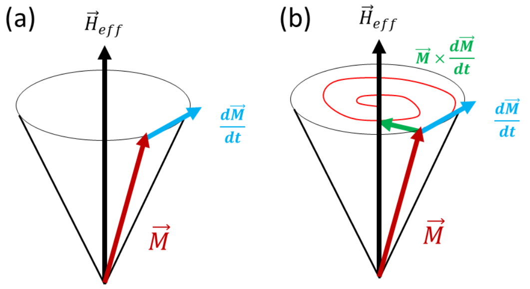

Figure 2.5: (a)Precessional motion of the magnetization vector M around the effective external magnetic field. As described by the first term on the right-hand side of Eq.2.25, the precessional motion is fully stable with no energy loss. (b)Spiraling motion of M towards H due to energy loss mechanism. This effect is described by the second term of the right-hand side of Eq.2.25. The damping constant α is a measure of the energy loss rate.

If the ferromagnetic system is excited through an external periodic magnetic field (h_{RF}) acting perpendicularly to the quasi-static magnetic field (H_{eff}), for specific combinations of the oscillating frequency of h_{RF} and H_{eff} an energy absorption phenomenon takes place giving rise to the ferromagnetic resonance. In order to extract the resonant condition the LLG equation must be solved for specific geometrical configurations of the system. For a thorough mathematical description of this procedure please refer to Ref.[69, 70].

2.2.3.3 FMR condition and absorption lineshape

The FMR is an absorption energy phenomenon where the magnetization vector in a ferromagnet resonates at the same frequency of an external oscillating magnetic field. The resonance is described by the complex susceptibility χ, which is derived by Eq.2.25 and has the form

$$\chi = \frac{M_S(B_{eff} - i\alpha\frac{\omega}{\gamma})}{(B_{eff} - i\alpha\frac{\omega}{\gamma})(H_{eff} - i\alpha\frac{\omega}{\gamma}) - (\frac{\omega}{\gamma})^2} \tag{2.27}$$

where B_{eff} and H_{eff} are the effective magnetic induction and the effective magnetic field respectively.[69, 70] The energy absorbed during the FMR is related to a variation of χ[70] and the absorbed power (P_{abs}) can be expressed as

$$P_{abs}(H) = \frac{1}{2} Im[\chi] h_{RF}^2 \tag{2.28}$$

The FMR thus occurs when $Im[\chi]$ reaches its maximum value, which corresponds to the maximum of the energy absorbed. By ignoring the damping terms ($\alpha = 0$), the relation between the resonant frequency ($f_{res} = \omega_{res}/2\pi$) and the applied external magnetic field H_{ext} for any mutual direction of $\vec{M}$ and H_{ext} can be obtained calculating the maximum of Eq.2.28 which occurs when

$$\omega_{res} = \frac{\gamma}{M_s sin(\theta_{eq})} \sqrt{\left(\frac{\partial^2 E_{TOT}}{\partial \theta^2} \frac{\partial^2 E_{TOT}}{\partial \phi^2} - \left(\frac{\partial^2 E_{TOT}}{\partial \theta \partial \phi}\right)\right)}\Big|_{\theta_{eq}\phi_{eq}} \tag{2.29}$$

The Eq.2.29 is called Smit-Beljers formula, where θ and ϕ are the spherical coordinates for $\vec{M}$.

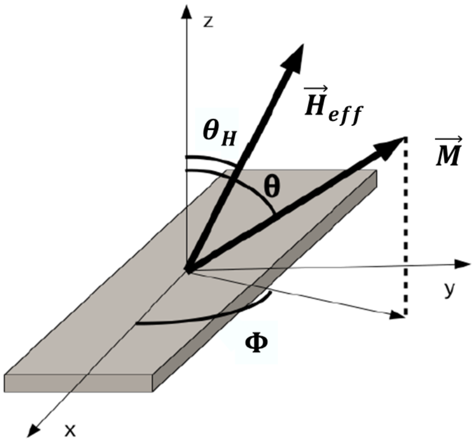

Figure 2.6: Generic geometrical configuration of H_{eff} and $\vec{M}$ with respect to the sample surface.

In Fig.2.6 a scheme of a system of coordinates with respect to the sample is shown and a generic configuration for the vectors H_{eff} and $\vec{M}$ is fixed. Here, θ_H indicate the angle between the normal to the sample surface (z-axis) and H_{eff}. As discussed in section 2.2.3.1, E_{TOT} determines the easy axis of the magnetization thus Eq.2.29 must be evaluated in the equilibrium position of the magnetization θ_{eq} and ϕ_{eq}, which can be determined minimizing the total energy density E_{TOT} as

$$\frac{\delta E_{TOT}}{\delta\theta}|_{\theta_{eq}} = 0 \qquad \frac{\delta E_{TOT}}{\delta\phi}|_{\phi_{eq}} = 0 \tag{2.30}$$

In the FMR experiments discussed in this thesis, the external magnetic field is applied parallel to the sample surface ($\theta_H = 90°$) and all the ferromagnetic films are polycrystalline. For this particular case the Smit-Beljers formula assumes a simplified form known as Kittel equation for the *in-plane configuration* [47, 68], which is given by

$$f_{res} = \frac{\gamma}{2\pi}\sqrt{H_{res}(H_{res} + 4\pi M_{eff})} \tag{2.31}$$

Here M_{eff} is the modulus of the effective magnetization vector, which is related to the saturation magnetization (M_s) value and *the out-of-plane anisotropy field* ($H_\perp$) by the relation

$$4\pi M_{eff} = 4\pi M_s - H_\perp = 4\pi M_s - \frac{2K_s}{M_s t_{FM}} \tag{2.32}$$

The latter equation links the value of the effective magnetization with the surface anisotropy constant K_s, which takes into account the role of the surface in ferromagnetic thin film. In order to extract information from this equation a study as a function of the thickness of the FM layer is necessary.
Considering the functional form of $Im[\chi]$ it is possible to demonstrate that the power absorbed by the sample close to the resonance can be modeled as a symmetric Lorentzian function. Anyway, an anti-symmetric contribution must be considered, because the coupling between the instrumentation and the sample can partially mix the imaginary and real parts of χ. [69] As a consequence, the FMR absorption line can be modeled as

$$P_{abs} = K_{sym}\frac{(\frac{\Delta H}{2})^2}{(\frac{\Delta H}{2})^2 + (H_{ext} - H_{res})^2} - K_{asym}\frac{\frac{\Delta H}{2}(H_{ext} - H_{res})}{(\frac{\Delta H}{2})^2 + (H_{ext} - H_{res})^2} \tag{2.33}$$

In the latter equation $\Delta H = 2\,\alpha\frac{\omega}{\gamma}$ (see also Eq. 2.37) and represents the full width at half maximum (FWHM) of the absorption signal (Fig.2.7). In the next section (Fig.2.8), in order to increase the sensitivity of the measurement, the rectified RF-signal is acquired with a lock-in amplifier. Through a lock-in amplifier the signal is shown in its first derivative form, which can be written as

$$\frac{dP_{abs}}{dH_{ext}} = -K_{Sym}\frac{(\Delta H)^2 - 4(H - H_{res})^2}{[4(H - H_{res})^2 + (\Delta H)^2]^2} + K_{Asym}\frac{4\Delta H(H - H_{res})}{[4(H - H_{res})^2 + (\Delta H)^2]^2} + mH + C \tag{2.34}$$

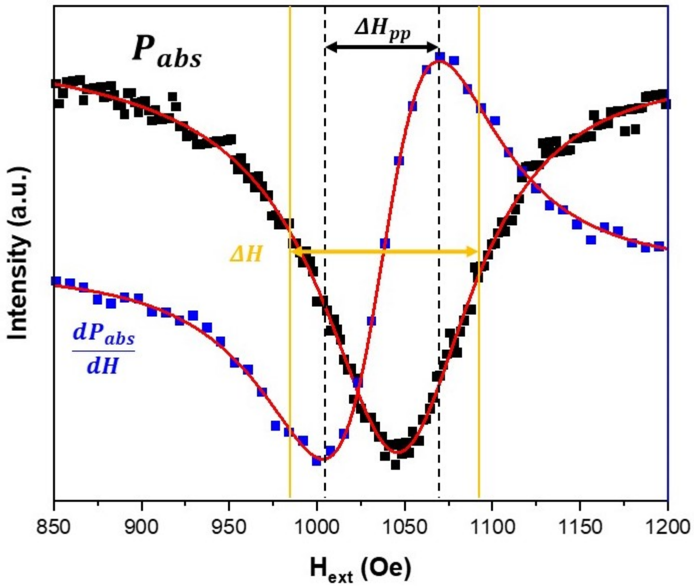

Figure 2.7: Typical FMR signal lineshapes of a Co(10 nm)/Sb_2Te_3 sample acquired at 12 GHz and relative fitting functions (red solid lines). The direct measurement of the absorbed power P_{abs} (black squares) is fitted with Eq.2.33 and its derivative signal (blue squares) with Eq.2.34. The fitting functions reproduce with a very good accuracy the evolution of both the datasets.

Despite the better sensitivity reached using the lock-in amplifier, at the beginning of the FMR studies performed in this thesis, measurements were performed through a direct acquisition of the signal, due to the lack of part of the instrumentation at the time. In this case the fit of the acquired FMR signal was performed using Eq.2.28. In order to make easier the treatment we will mention this during the discussion of the results when necessary (Section 3.3.1).

Eq.2.34 is the derivative form of Eq.2.33, where the linear term "mH" is added to account for the typical drift of the FMR signal during the measurement sweep.[71] Calculating the stationary points of the second derivative of Eq.2.33, we obtain the peak-to-peak linewidth of the first derivative of P_{abs}, which is linked to the FWHM of Eq.2.28 by the relation

$$\Delta H_{pp} = \frac{\Delta H}{\sqrt{3}} \tag{2.35}$$

which brings to the following equation

$$\Delta H_{pp} = \frac{\Delta H}{\sqrt{3}} = \frac{2}{\sqrt{3}}\frac{\alpha\omega}{\gamma} \Rightarrow \Delta H = \frac{4\pi\alpha}{\gamma} f_{res} \tag{2.36}$$

Performing a study of the linewidth as a function of the resonant frequency, from the latter equation it is possible to extract α value. In real systems, any magneto-structural disorder in the ferromagnetic film introduces an additional inhomogeneous broadening term (H_0), which has to be added in order to interpret the experimental data [68], see Eq. 2.37.

$$\Delta H = \frac{4\pi\alpha}{\gamma} f_{res} + \Delta H_0 \tag{2.37}$$

2.2.3.4 Broadband-FMR experimental setup

The BFMR measurements were performed using a home-made facility obtained from the customization of a Bruker ER-200 instrument originally adopted for Electron Paramagnetic Resonance (EPR) measurements. The setup is composed by a broadband Anritsu-MG3694C power source (1-40 GHz), which is connected to a home-made grounded coplanar waveguide (GCPW)(described in section 2.2.3.4) where the ferromagnetic sample is mounted in a flip-chip configuration (with the FM film close to the CPWG surface) with a $20\mu m$ thick mylar foil placed in between to avoid the shortening of the conduction line. When the RF-current exits from the GCPW, the signal is directed to a rectifying diode (Wiltron, Model 70KB50 (NEG), 1 - 26.5 GHz, 20 dbm MAX) which converts the RF-signal in a continuous DC-current, in turn sent to a lock-in amplifier for the signal detection. A scheme of the BFMR facility is shown in Fig.2.8. The FMR measurement was conducted positioning the sample between the polar extensions of the Bruker ER-200 electromagnet and maintaining its surface parallel to the external magnetic field H_{ext}, in the so called *in-plane* (IP) *configuration*.

Once the microwave frequency was fixed, the measurement was performed by measuring the derivative of absorption power ($\frac{dP_{abs}}{dH}$) downstream of the electrical transmission line

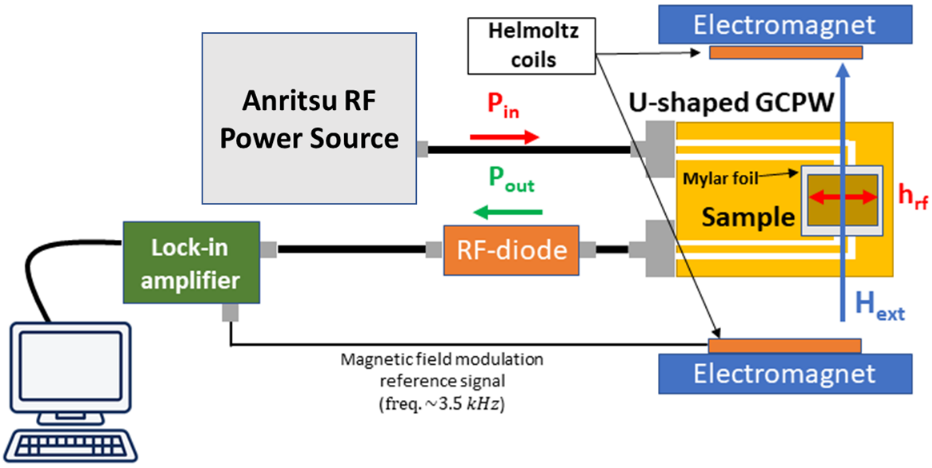

Figure 2.8: Scheme of the custom instrumental setup used to perform BFMR measurements.

as a function of the external magnetic field produced by the electromagnets. Fixing the RF-signal power, the same procedure was repeated for different frequency values. In Fig.2.9 an example of the fitting of the collected data with the described FMR setup.

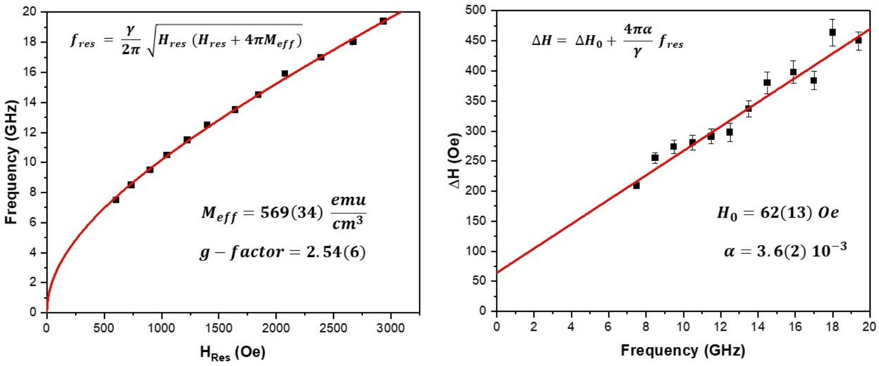

Figure 2.9: FMR caracterization of a Au(5nm)/Co(5nm)/Sb_2Te_3 heterostructure. On the left a typical fit of the $f_{res}(H_{res})$ curve using the Kittel equation for the in-plane configuration. On the right the linear fit of the FMR signal linewidth (ΔH) as a function of the resonant frequency (f_{res}). The insets show the parameters extracted from the fits are reported.

Grounded Coplanar Waveguide (GCPW) The GCPW is the RF-component used to generate the oscillating h_{RF} magnetic field (see Eq. 2.28). A GCPW consists essentially in a central conductor of width w_s which carries the RF-current (signal line, S) and two ground planes (G) separated from the signal line by an air gap of thickness w_{sg} (Fig2.10).

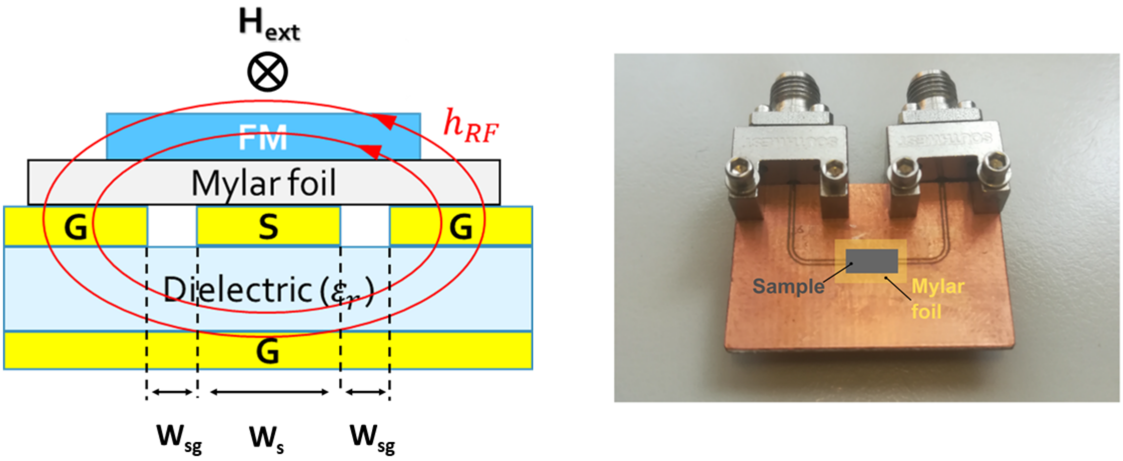

Figure 2.10: (a)Illustration of a FM sample positioned in the flip-chip orientation on a GCPW. S and G indicate respectively the signal and the ground conduction lines. h_{RF} represents the oscillating magnetic field produced by the RF-current. (b) Image of the home-made U-shaped GCPW, where the positions of the sample and of the Mylar foil used during the measurements are highlighted. The Mylar foil is located between the sample and the board in order to avoid the electrical shortening of the line. To connect the GCPW with the RF power source two Southwest connectors for high frequency application are used.

During the BFMR experiments conducted in this thesis, an home-made U-shaped GCPW was exploited for the acquisition of the FMR signal. In order to produce a broadband GCPW, the Sonnet Software program for the modeling of high frequency conductive lines was used. As a result, a broadband GCPW up to 20 GHz was obtained, with less than 4 dB as a maximum power loss over the whole frequency range. The simulated model considered the electric properties of the Cu/Dielectric/Cu tri-layer composing the GCPW (RF-35 material provided by Taconic), and the geometrical constrains due to the fixed distance of the electromagnet's poles of the Bruker ER-200 facility. In Fig. 2.11(a) and (b) the geometry and the modulus of the impedance of the simulated GCPW |S21| are showed respectively. The production of the GCPW was carried out using conventional photolithographic processes, where an aqueous $FeCl_3$ solution was employed as the etching solution for Cu. The shadow-mask with the desired geometric shape was created by means of a professional ink-jet printer, which printed the mask on a transparent plastic foil(Fig.2.12).

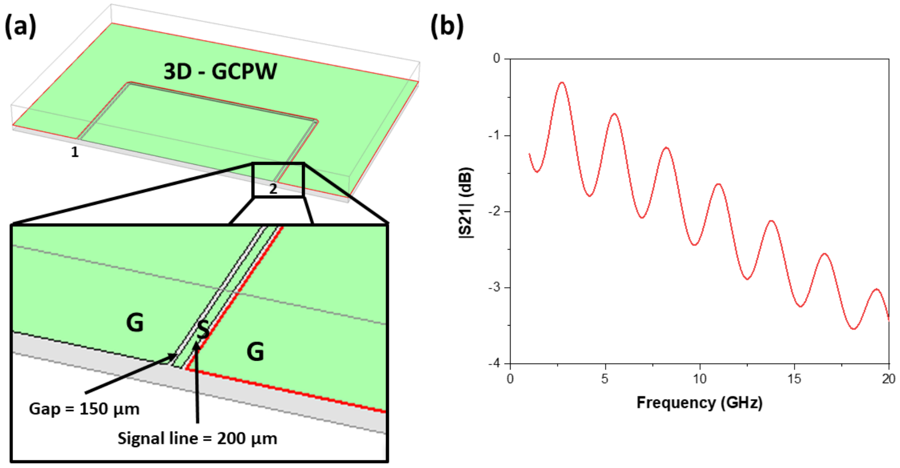

Figure 2.11: (a) Rendering 3D of the simulated GCPW with the Sonnet Software. The numbers 1 and 2 are the labels of the simulated electrical connections. (b) Modulus of the impendance (|S21|) between the ports 1 and 2 is simulated as a function of the RF frequency.

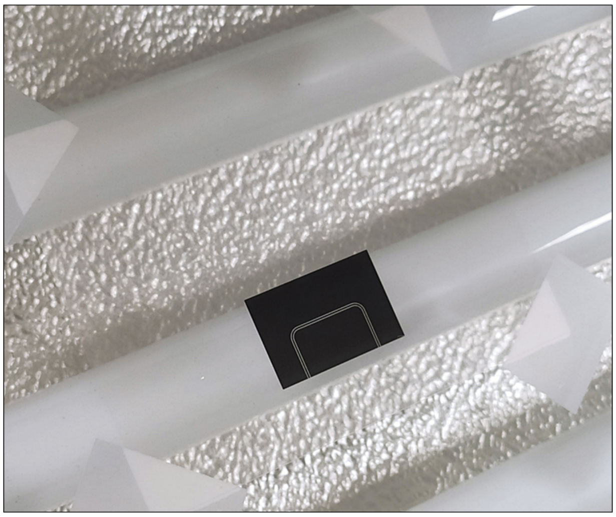

Figure 2.12: Ink-jet printed photolithographic mask on a transparent plastic foil. The mask was fixed on the glass of an UV lamp to impress the resist during the lithographic process.

In addition to the description of the magnetization dynamics in FM thin films, the FMR setup described here can be adapted to evaluate the spin-to-charge interconversion across the FM/NM interface, exploiting the so called SP technique. In the next section, the main theoretical concepts concerning the SP mechanism and the instrumentation setup are discussed.

2.2.3.5 Spin pumping by FMR

The spin-to-charge interconversion mechanism at the interface of FM/NM systems can be investigated using several techniques such as SP-FMR [49, 59, 72], ST-FMR [73–75], harmonic longitudinal voltage measurements [76], etc. In SP by FMR (SP-FMR), the precessional motion of the magnetization in the FM generates a pure spin current which is subsequently injected in the NM layer and here converted in a charge current. The theoretical description of the spin current generation and its transport across the interface in FM/NM heterostructures in SP-FMR experiments was deeply discussed by Tserkovnyak *et al.* (2002)[77, 78] and, in the last twenty years, experimentally widely demonstrated and reported in literature, see for instance Ref.[52, 55, 79–81] .
In Section 1.4, we briefly introduced both the SP-FMR and the ST-FMR techniques and we pointed out that these two mechanisms can be interpreted as the *two sides of the same coin*(Fig.2.13). Indeed, as firstly described by Slonczewski in 1996 [8], in FM/NM systems when a charge current is flowing across the NM layer, it can exert a torque on the FM and eventually switching its magnetization (Section 1.1). According to the Slonczewski theory the torque on the FM magnetization can be accounted by adding a further term in the LLG equation (τ_{Sloncz}), which can be written as

$$\frac{d\vec{M}}{dt} = -\mu_0\gamma\vec{M} \times \vec{H_{eff}} + \frac{\alpha}{\vec{M_s}}(\vec{M} \times \frac{d\vec{M}}{dt}) + \vec{\tau}_{Sloncz} \tag{2.38}$$

Thus, according to the latter equation, the effect of the current is to add a torque on the magnetization vector $\vec{M}$, sustaining the magnetization precession. For that, the τ_{Sloncz} term is also known as *anti-damping* term (Fig.2.13). On the other hand, if the vector $\vec{M}$ loses its torque during its motion an extra contribution to the damping is provided, which can be seen as the opposite effect of the Slonczewski torque. We refer to the latter effect equivalently as SP or SP-FMR. As described by Tserkovnyak and co-authors, part of the magnetic moment lost by $\vec{M}$ can be converted in a pure spin current J_S^{3D}, which is pumped from the FM into the NM layer.

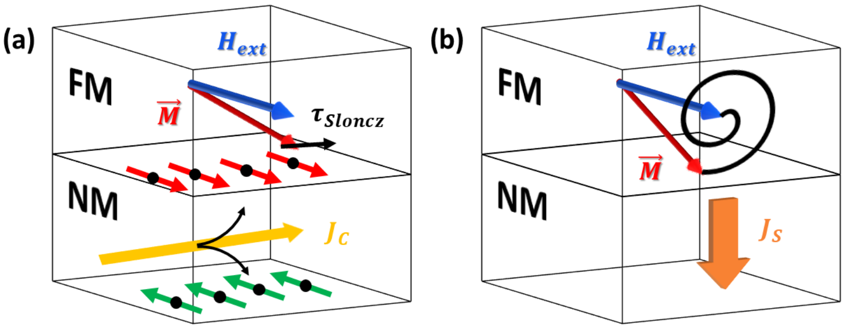

Figure 2.13: (a) Sketch of the torque (τ_{Sloncz}) induced by the spin accumulation in the NM material on the FM magnetization. (b) If the magnetization of a FM material is forced to precess under the effect of an external RF magnetic field, a portion of the angular momentum can be transferred in the adjacent NM layer as a pure spin current J_s.

In the SP theory the extra damping $\Delta\alpha$ enters in the LLG equation as

$$\frac{d\vec{M}}{dt} = -\mu_0\gamma\vec{M} \times \vec{H_{eff}} + \frac{\alpha_{ref}}{\vec{M_s}}(\vec{M} \times \frac{d\vec{M}}{dt}) + \frac{\Delta\alpha}{\vec{M_s}}(\vec{M} \times \frac{d\vec{M}}{dt}) \tag{2.39}$$

where α_{ref} is the damping constant of the free standing FM layer, when not influenced by the presence of an adjacent NM layer. The total damping is finally written as

$$\alpha_{tot} = \alpha_{ref} + \Delta\alpha \tag{2.40}$$

and according to Ref. [77] can be expanded as

$$\alpha_{tot} = \alpha_{ref} + Re(g_{eff}^{\uparrow\downarrow})\frac{g\mu_B}{4\pi M_s}\frac{1}{t_{FM}} \tag{2.41}$$

where $Re(g_{eff}^{\uparrow\downarrow})$ is the real part of the spin mixing conductance, a quantity which provides information on the spin transmission across the FM/NM interface, and t_{FM} is the thickness of the FM layer. The expression for the 3D spin current (J_S^{3D}) generated in the FM layer as a consequence of the extra damping term in Eq.2.41 is [77]

$$J_S^{3D} = \frac{\hbar}{4\pi}\frac{Re(g_{eff}^{\uparrow\downarrow})}{M_s^2}\vec{M} \times \frac{d\vec{M}}{dt}\left(\frac{2e}{\hbar}\right) \tag{2.42}$$

The latter equation for the generated spin current in a SP experiment is not complete, because it does not take into account a correction due to a possible back-flow of the spin current. Indeed, if $t_{NM} << \lambda_s$, where λ_s is the spin diffusion length in the NM material, the spin current will be reflected at the NM/vacuum interface, lowering the net spin current crossing the FM/NM interface. To properly consider the back-flow the net spin current needs to be corrected as

$$J_{S,net}^{3D} = J_S^{3D}\Big(1 - e^{\frac{-2t_{NM}}{\lambda_s}}\Big) \tag{2.43}$$

Eq. 2.41 and Eq.2.42 evidence the importance of a correct estimation of the damping constant in the FM/NM heterostructures, which is measured by the FMR experiments described in Section 2.2.3.1. By solving the LLG equation (Eq. 2.42), J_S^{3D} as a function of the angle θ_M (Fig. 2.6) can be expressed as

$$J_S^{3D} = \frac{Re(g_{eff}^{\uparrow\downarrow})\gamma^2\hbar h_{RF}^2}{8\pi\alpha^2}\Big(\frac{\mu_0 M_s\gamma sin^2(\theta_M) + \sqrt{(\mu_0 M_s\gamma sin^2(\theta_M))^2 + 4\omega^2}}{(4\pi M_s\gamma sin^2(\theta_M)^2) + 4\omega^2}\Big)\Big(\frac{2e}{\hbar}\Big) \tag{2.44}$$

In our SP-FMR experiments the external magnetic field was maintained parallel to the FM surface, thus in Eq.2.44 the terms $sin^2(\theta_M)$ are equal to 1.

SP-FMR experimental setup

As discussed in the previous section, the J_S^{3D} generated in the FM and injected perpendicularly into the NM layer, is able to produce a charge current I_c. This current generated in the NM layer can be detected as a drop of potential across the measured sample.[167,168 Noel thesis] In Fig.2.14(a) the scheme of the modified FMR setup to perform SP-FMR measurements is reported. Basically, the instrumentation is the same as in the FMR experiment (Fig.2.8), but in this case the sample is connected to a nanovoltmeter using two thin Ag wires connected to the sample edges with Ag paint. As we discussed above, the SP effect takes place during the FMR. Thus, the standard procedure for the acquisition of the SP signal is to synchronize the sweep of the applied external magnetic field with the DC voltage acquisition of the nanovoltmeter and, as a result, a $V(H)$ plot is generated (Fig.2.15).

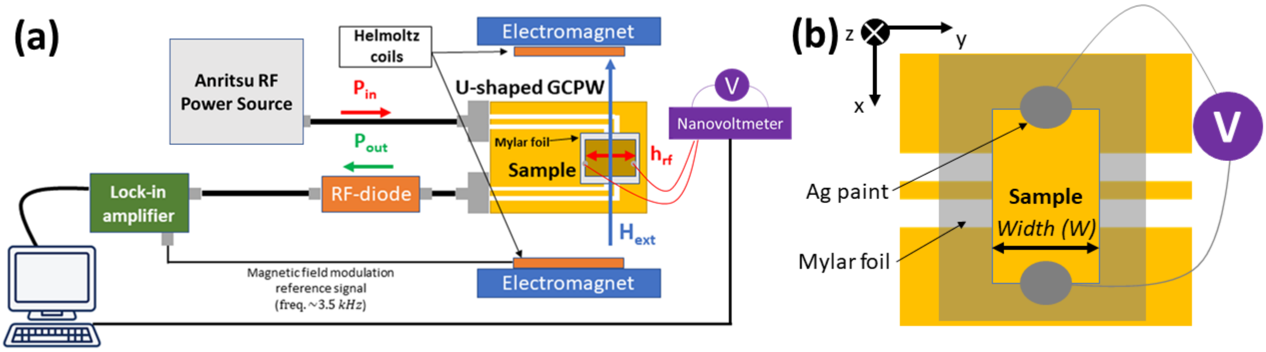

Figure 2.14: (a) The same FMR measurement setup adapted for SP-FMR measurements. (b) A particular of the sample mounted on the GCPW and electrically connected to a nanovoltmeter through Ag wires and AG paint.

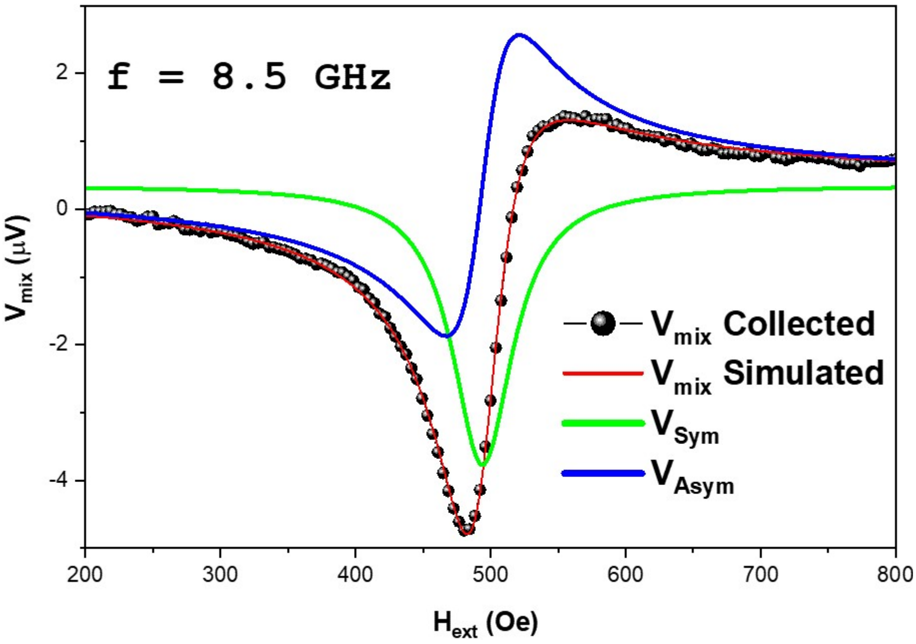

Figure 2.15: Acquired SP signal for a Au(5 nm)/Co(20 nm)/Au(5 nm/Sb_2Te_3 heterostructure at fixed RF frequency of 8.5 GHz and fixed RF power of 73 mW. The $V_{mix}(H_{ext})$ curve is fitted with Eq.2.45 and the V_{Sym} and V_{Asym} components are extracted.

It is fundamental that during the SP measurement the modulation of the magnetic field is turned off, because the low frequency modulation of the Helmoltz coils induces artifacts in the DC voltage signal. Being the SP-FMR signal a direct consequence of the

FMR phenomenon, the $V(H)$ signal can be fitted with a Lorentian function of with the following form

$$V_{mix} = V_{Sym}\frac{(\Delta H)^2}{\Delta H^2 + (H - H_{res})^2} + V_{Asym}\frac{(\Delta H)(H - H_{res})}{\Delta H^2 + (H - H_{res})^2} \tag{2.45}$$

where V_{Sym} and V_{Asym} are the prefactors of the symmetric and anti-symmetric part of the Lorentzian function. In Eq. 2.45, ΔH indicates the half width at half maximum (HWHM) of the V_{mix} curve, and in this case the $\Delta H(f)$ dispersion can be written as

$$\Delta H = \frac{2\pi\alpha}{\gamma} f_{res} + \Delta H_0 \tag{2.46}$$

The voltage generated during a SP experiment is called mixing voltage (V_{mix}), being an admixture of voltage signals with different origins. The SP signal has the form of a symmetric Lorentian, thus $V_{Sym} = V_{SP}$. On the other hand, anti-symmetric signals can contribute in the V_{mix} shape, usually due to anomalous Hall effect (AHE) and anisotropic magnetoresistance (AMR). [32, 81, 82]

Once the value of V_{SP} is extracted from Eq.2.45, the estimation of the generated I_c current can be calculated using the Ohm's law

$$I_c = \frac{V_{SP}}{R} \tag{2.47}$$

where R is the sheet resistance of the sample and it is independently calculated by four point measurements. Usually, typical values for R are few tens of Ohm.[52] Another important aspect for the calculation of the quantities of interest in SP measurements is the estimation of the h_{RF} value. Indeed, as shown in Eq.2.44, the latter is necessary to calculate the value of the generated 3D spin current generated in the FM layer. Usually, a precise estimation of h_{RF} is obtained performing SP measurement with a cavity FMR instrumental setup and it depends on the geometrical characteristics of the cavity.[49, 50, 52] In our experiments we measured the SP directly with the GCPW, thus in order to estimate the h_{RF} value we performed some calculations starting from the geometry of our GCPW and using the Bio-Savart law. In Fig.2.16 a general geometry of a GCPW and the calculation we used are reported.

The graph shown in Fig.2.16 shows the variation of the strength of the magnetic field produced by the RF current at the center of the signal line (S) and on the normal z, for

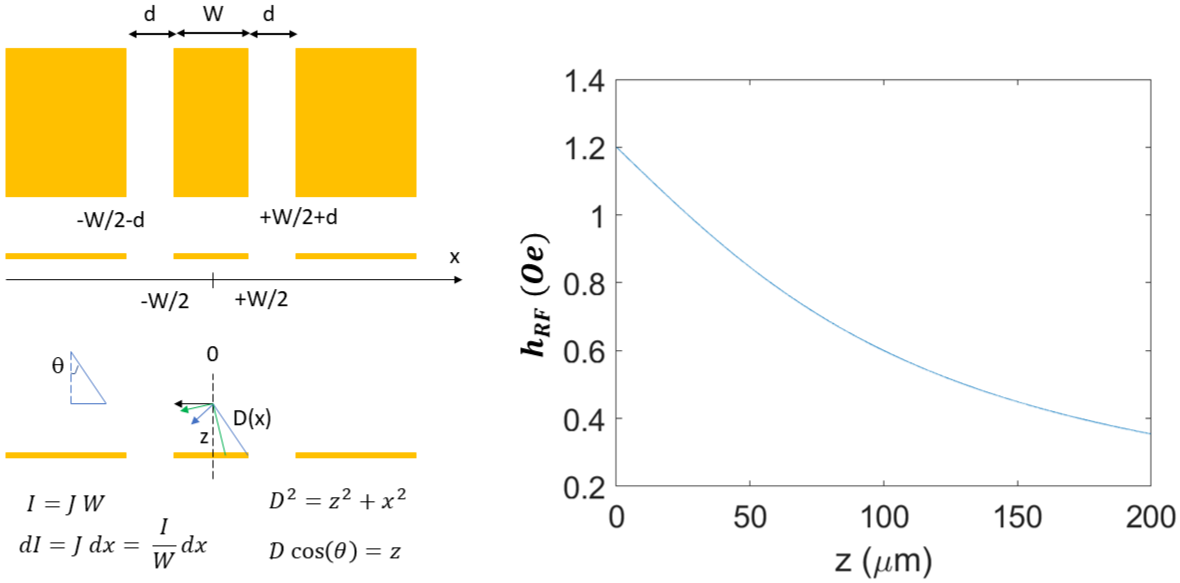

$$h_{RF}(z) = \int_{x=-\frac{W}{2}}^{x=+\frac{W}{2}} \cos(\theta)\frac{\mu_0 dI}{2\pi D} = \frac{\mu_0 I z}{2\pi W}\int_{x=-\frac{W}{2}}^{x=+\frac{W}{2}} \frac{dx}{x^2+z^2} = \frac{\mu_0 I}{\pi W}\tan^{-1}\left(\frac{W}{2z}\right)$$

Figure 2.16: Simulation of the h_{rf} magnetic field generated by the home-made GCPW described in Section 2.2.3.4 as a function of the distance from the surface. For the simulation we fixed W=200μm, d=150μm and RF-power = 73 mW. Considering the distance of the measured samples from the GCPW surface, in the SP-FMR measurements we considered $h_{RF} \sim 0.7 Oe$.

a fixed RF-power. Measuring the real height of the sample from the GCPW surface, we found that, due to the asperity of the GCPW , the average distance of our sample from the surface is around $70 \pm 10\mu m$. For that in the calculation of J_S^{3D} we assumed h_{RF} = 0.7 Oe. Anyway, in our opinion this value for h_{RF} could be largely over estimated, being the simulated geometry in Fig.2.16 just a rough estimation of the effective h_{RF} value generated by our home-made GCPW (Section2.2.3.4). For that, the results that we obtained in Section 3.4 represent a lower limit of the real spin-to-charge conversion efficiency in the studied samples.

At the interface between a FM and a NM film the SCC mechanisms can arise as a consequence of two mechanisms: the SHE generated in the bulk of the NM layers or the IEE in the surface states. In the following section a brief explanation of these two effects is reported and the relative figures of merit for the SCC efficiency are indicated.

2.2.3.6 Spin Hall and Inverse Spin Hall Effect (SHE, ISHE)

Generally, three main Hall effects can be observed in a material: the ordinary Hall effect (HE), the Anomalous Hall Effect (AHE) and the SHE [17], which are sketched in Fig.2.17 (a), (b) and (c) respectively. The SHE is a quantum-mechanical phenomena related with the SOI discovered by Dyakonov and Perel in 1971 [83], which allows the charge-to-spin (direct SHE) or the spin-to-charge (inverse SHE or ISHE) conversion in NM material. When an electrical current flows through a metal with large SOC (i.e HMs), electrons with opposite spins are deflected in opposite directions (Fig. 2.17(c)).

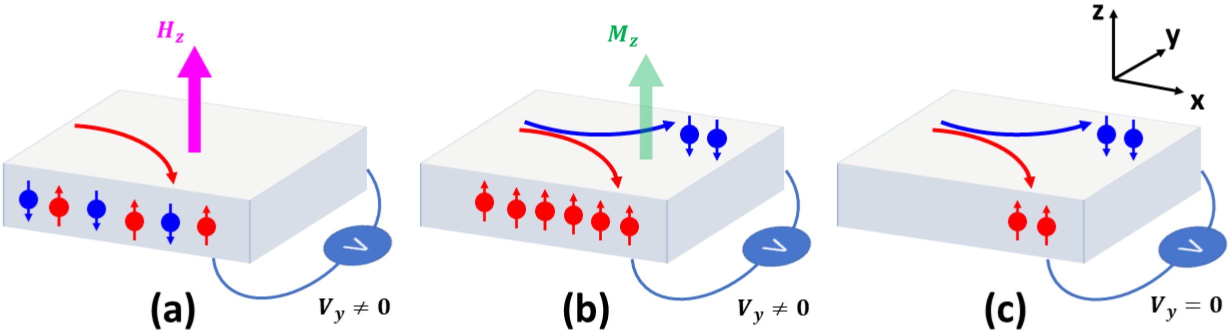

Figure 2.17: (a) Ordinary Hall effect. An external magnetic field applied along the z direction causes a charge unbalance at the boundaries, due to the Lorentz force ($F_y = ev_{drift}H_z$) exerted on the electrons.(b) Additional contribution to the ordinary Hall effect in (a). No external magnetic field is applied. AHE is similar to the Hall effect but here there is also a spin unbalance at the boundaries of the material due to spin-dependent scattering processes or spin-dependent band structure. AHE is often used as proof of ferromagnetism in materials. (c) Spin splitting inside the material due to the SHE. No external magnetic field is applied on the material.

As a consequence, a spin current perpendicular to the charge current direction takes place (Eq.2.48). The SCC efficiency due to SHE is accounted by the so called Spin Hall Angle (θ_{SHE}), a dimensionless quantity proportional to the ratio between the generated spin current from a charge current (direct SHE) or viceversa (ISHE). In the case of SP experiments (Section 3.4) the ISHE is exploited, thus the θ_{SHE} can be calculated from

$$\vec{J}_c^{ISHE} = \theta_{SHE} \vec{J}_s \times \vec{\sigma} \tag{2.48}$$

where $\vec{\sigma}$ is the unit vector of the spin polarization. Being the SHE dependent by the strength of the SOC, the θ_{SHE} value is expected to ber higher in materials with a high atomic number, such as HMs (i.e. Pt, Ta, Pd, W). A table with typical θ_{SHE} values is reported in Ref. [17]. The SHE is a complex phenomenon which can have an intrinsic (without impurities) or extrinsic (with impurities) nature. Further details about the latter arguments can be found in Ref. [84] and in the references of this paper.

2.2.3.7 Edelstein and Inverse Edelstein Effect (EE, IEE)

Another interface effect closely related to the SHE is the so called Edelstein effect (EE).[51] Here, a steady current J_x, driven by an electric field E_x produces a steady non-equilibrium spin polarization.[85] The EE has been observed experimentally [86, 87] and can be interpreted as the result of the effective magnetic field, generated due to spin-orbit coupling, acting on the drifting electrons of a NM material in their own reference frame.[88] In the past decade, a drift-diffusion theory of the SHE, ISHE, and EE has been proposed.[89] On the other hand, the inverse Edelstein effect (IEE) was poorly studied, despite the spin-galvanic effect observed almost a decade ago by Ganichev *et al.* [90] in GaAs can be interpreted as a manifestation of the IEE. In the very recent paper of Rojas-Sánchez *et al.* [49], the IEE was described and experimentally demonstrated for the first time.

The IEE can take place exploiting SOC-related properties of a two dimensional electron gas (2DEG) at specific surfaces and interfaces, such as the so-called Rashba interfaces [91] and the TSS of TIs.[24] Due to the similarities between the bandstructures of Rashba interfaces and TIs we will discuss the EE and IEE in both of them simultaneously.
In Ref.[49], the energy dispersion of the 2D states in a Rashba interface and the Dirac-like linearly dispersed TSS of a TI are represented, as depicted in Fig. 2.18.
In the EE, a charge current density J_c^{2D} is injected along the x-direction and in the plane of the sample and an electric field rises according to the equation $J_c^{2D} = \sigma\vec{E}$, where σ is the electrical conductivity. As a result, a Coulomb force acts on the electrons in the material, $\vec{F}_{Coul} = q\vec{E}$ with q the electron charge. Being $\vec{F}_{Coul} = d\vec{p}/dt$ and $\vec{p} = \hbar\vec{k}$ with $\vec{p}$ and $\vec{k}$ the momentum and the wave vector of the electron, if the charge current is injected for a time Δt, we have

$$\Delta\vec{k} = \frac{\Delta t q J_c^{2D}}{\sigma\hbar} \tag{2.49}$$

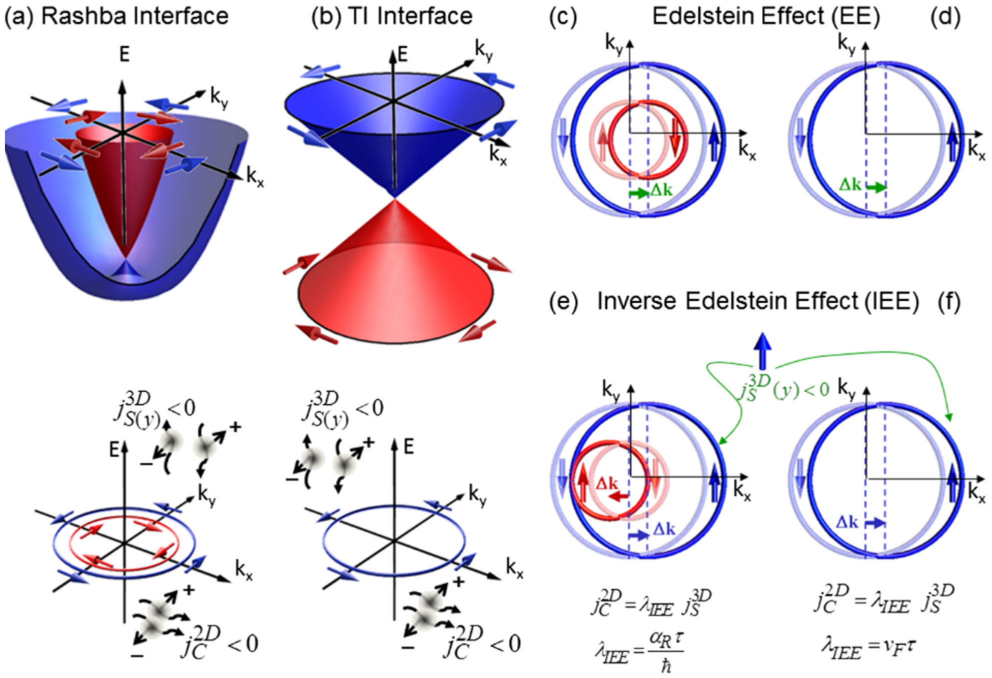

Figure 2.18: In the top panel of (a) and (b) the energy dispersion of a 2D Rashba surface and a Linearly dispersed TI surface are shown respectively. At the bottom of (a) and (b), the Fermi contour for the Rashba case and the TI surface are represented with their chirality. In (c) and (d) the EE effect is represented for the two systems. If a charge current J_c^{2D} flows along the x direction, a ΔH shift of the contours arises, with a consequent generation of an extra spin population along the y direction. (e) and (f) represent the opposite phenomena of (c) and (d) (IEE), where an injected spin current J_S^{3D} along the y direction creates a region with a spin accumulation on one side of the Fermi contour and a depleted region on the other side, giving rise to a charge current J_c^{2D} in the x direction. Figure taken from Ref.[49].

If Δt is in the range of the typical electron relaxation time τ, thus in the range of the femptoseconds (in metals) and picoseconds (in semiconductors), it is possible to write

$$\Delta\vec{k} = \frac{\tau q J_c^{2D}}{\sigma\hbar} \tag{2.50}$$

The latter shift does not depends directly on $\vec{k}$, thus a rigid shift of the Fermi contour occurs, as shown in Fig. 2.18(c) and (d).

For the EE a charge-to-spin conversion between a 2D charge current into a 3D spin current takes place, therefore it is possible to define a conversion efficiency for such process as

$$q_{EE} = \frac{J_S^{3D}}{J_c^{2D}} \tag{2.51}$$

where q_{EE} has the dimension of an inverse of a length.
In the case of the reciprocal IEE, a pure 3D spin current is converted into a charge current during a spin-to-charge conversion process. In a IEE the spin accumulation is created directly by the injected 3D spin current, giving rise to the $\Delta\vec{k}$ shift discussed above. The spin-to-charge conversion efficiency for the IEE can be written as

$$\lambda_{IEE} = \frac{J_c^{2D}}{J_s^{3D}} \tag{2.52}$$

where λ_{IEE} is the so-called inverse Edelstein length, usually expressed in nm. According to the calculation carried out by Fert and Zhang in Ref.[92], in a TI λ_{IEE} can be written as

$$\lambda_{IEE} = v_F \tau_p \equiv \lambda_{mf} \tag{2.53}$$

where v_F and τ_p are the Fermi velocity and the relaxation time of the electronic momentum, which takes into account the scattering of the electrons in the TI bands. As a consequence, the λ_{IEE} is exactly equivalent to the mean free path (λ_{mf}) in the TI.

2.2.3.8 Estimation of the Spin-Charge conversion efficiency

In the previous section we introduced some general concepts concerning the SP experiments and the theoretical interpretation at the base of the data acquired in such experiments. In this section we summarize the final shape of the equations used to extract the SCC in the materials studied in this thesis, according to the adopted model for the data interpretation.
In a FM/NM system if the SCC is attributed only to the IEE the 3D spin current generated inside the FM material is entirely absorbed by the surface states at the FM/NM interface. Here, a 2D charge current is generated and the IEE length can be calculated as

$$\lambda_{IEE} = \frac{J_c^{2D}}{J_s^{3D}} = \frac{I_c}{W J_s^{3D} sin(\theta_M)} \tag{2.54}$$

where W is the width of the measured sample (Fig.2.14(b)). On the other hand, if we considered the SCC arising as a consequence of the ISHE, the spin diffusion length (λ_s) in the bulk of the NM material needs to be accounted for. In this case as demonstrated in Ref.[82] the following equation is valid

$$J_s(z) = J_s^{3D} \frac{sinh(\frac{t_N - z}{\lambda_s})}{sinh(\frac{t_N}{\lambda_s})} \tag{2.55}$$

where t_N is the thickness of the NM layer. In order to calculate the generated charge current I_c along the x direction, Eq.2.48 must be integrated along z:

$$I_c = W \int_0^{t_N} \theta_{SHE} (\vec{J_s}(z) \times \vec{\sigma}) \cdot \vec{x} dz \tag{2.56}$$

By substituting the expression reported in Eq.2.55 in the latter equation, the θ_{SHE} can be calculated as

$$\theta_{SHE} = \frac{J_c^{2D}}{sin(\theta_M) J_S^{3D}(\theta_M) \lambda_s tanh(\frac{t_N}{2\lambda_s})} = \frac{I_c}{W sin(\theta_M) J_S^{3D}(\theta_M) \lambda_s tanh(\frac{t_N}{2\lambda_s})} \tag{2.57}$$

The latter equation shows that the ISHE depends by both the t_{NM} and λ_s of the NM material. As a consequence of this expression, it turns out that the voltage signal measured in a SP experiment is not directly proportional to the θ_{SHE}, but to the product $\theta_{SHE}\lambda_s$. Indeed, as reported in Ref.[93, 94], it is possible to extract the value of λ_s studying the generated spin signal as a function of t_{NM}. In this thesis, we did not perform a similar t_{NM} dependent study, thus the λ_s value was extracted by independent measurements as discussed along the text in Section 3.4.

2.2.4 Other methods

The scientific results presented in this thesis are obtained also thanks to the efforts spent by many researchers belonging to different research institutes, which collaborated with our group to perform complementary measurements to those obtained by X-ray based and FMR techniques.

2.2.4.1 Time-of-Flight Secondary Ion Mass Spectrometry (ToF-SIMS)

The elemental distribution in the studied heterostructures was determined by ToF-SIMS measurements performed in the CNR-IMM Unit of Agrate Brianza laboratory. An ION TOF IV, using Cs^+ ions with 500 ev for sputtering and Ga^+ ions at E = 25keV, was used for the analysis. The secondary ions were collected in negative polarity and in interlaced mode. As discussed in chapter 3, the ToF-SIMS was used to analyse the elemental interdiffusion in samples with Fe atoms. Under this operation mode, in a Fe (or FeO_x) matrix, the sensitivity of the instrument is enhanced for secondary FeO^- ions with respect to the elemental Fe^- ion [95].

2.2.4.2 Vibrating Sample Magnetometry (VSM)

For a complementary magnetic characterization of the magnetic samples, VSM measurements were performed on the investigated samples at the Polifab Laboratory - Politecnico di Milano. The heterostructures hysteresys loops were acquired using a MicroSense EZ-9 vibrating sample magnetometer, from which the saturation magnetization (M_s) and the direction of the easy/hard axis were identified.

2.2.4.3 Atomic and Magnetic Force Microscopy(AFM/MFM)

In order to extract information about the magnetic and morphological features of the surface of the analysed thin films, a Bruker AFM/MFM commercial system was used. In order to efficiently decouple the morphological and magnetic signals, the tip of the AFM/MFM probe was maintained at different heights from the surface, as explained during the discussion of the results.

2.2.4.4 Brillouin Light Scattering (BLS)

Thanks to a collaboration with the University of Perugia, a BLS study was conducted on selected samples. The BLS is an optic technique which makes possible the excitation of spin waves inside a magnetic material when lighted with a laser source. Through the analysis of the optic response, the magnetic properties of a magnetic material can be studied. In order to be used as a complementary analysis to the BFMR, the BLS experiments were conducted applying a fixed external magnetic field parallel to the sample plane while the laser light was focused at normal incidence and its frequency is swept. In such configuration BLS is totally equivalent to the BFMR adopted in this work.[96, 97] Thanks to the BLS we managed to investigate the magnetic signal produced by ultra-thin ferromagnetic thin films (less than 2 nm), often too weak to be easily detected by a BFMR measurement.

2.2.4.5 Conversion Electron Mossbauer Spectroscopy (CEMS)

The CEMS technique provides information about the chemical-structural and magnetic environment of ^{57}Fe atoms. The ^{57}Fe selectivity of this technique and the possibility to grow ultra thin ^{57}Fe films on top of other materials, make CEMS a very powerful tool for the investigation of interface phenomena, following the magnetic properties of an interface as a function of its chemical-structural modifications (i.e. intermixing, reconstruction, etc.) CEMS analysis was carried out at RT in a constant-acceleration drive, with the sample mounted as an electrode in a parallel plate avalanche detector filled with acetone gas. An α-Fe foil at RT was used for CEMS velocity scale calibration and all the reported isomer shift were relative to α-Fe. The CEMS apparatus is the home-made facility present at the CNR-IMM Unit of Agrate Brianza laboratory and the collected spectra analysed with the Vinda software package.[98] For further details on this technique please refer to [99–101].

Chapter 3

Results and Discussion

3.1 Integration of Fe and Co thin films with granular Sb_2Te_3

In the first part of the following section the chemical-structural properties of MOCVD-deposited granular Sb_2Te_3 thin films are discussed. Two approaches for the integration of Fe and Co thins films with Sb_2Te_3 are proposed together with strategies for the improvement of the FM/Sb_2Te_3 interface quality. The content of this section is largely based on the results reported in the papers Ref. [44, 102, 103]. My main contribution in these works was the analysis of the samples with XRD/XRR techniques, the study of the effect of thermal treatments (which I directly performed) on their chemical-structural properties and the thermodynamic description of the chemical evolution of the interfaces in the presented multilayered heterostructures. In the case of the Co deposition, in addition to the above mentioned characterization activity, I also directly performed the growth of the materials by means of ALD. Moreover, I collected, organized and linked the data acquired by my coworkers in order to produce a systematic description of the studied phenomena.

3.1.1 Chemical-structural characterization of granular Sb_2Te_3

A 30 nm thick polycrystalline granular Sb_2Te_3 thin film was deposited by MOCVD on large area (4") SiO_2/Si substrates at RT. Despite of the granular nature, the Sb_2Te_3

thin film turned out to be structurally continuous as observed by Scanning Electron Microscopy (SEM). In Fig.3.1 (a), (b) and (c) the top, tilted and side views of the grown Sb_2Te_3 thin films are reported respectively. The proof of the topological nature of the Sb_2Te_3 film, and thus also its electrical continuity, was reported in a recent paper published by our group [104]. Here, low temperature magnetotransport measurements on the Sb_2Te_3 thin films have been conducted, with the consequent demonstration of weak antilocalization (WAL) effect. The WAL can be interpreted as a marker for the presence of surface conductive states in a TI material. As discussed in Ref.[104], the magnetotransport measurements are very often affected by thermal noise, thus the topology in Sb_2Te_3 thin films was observed only at low temperature (15 K). Nevertheless, as reported by several groups[REF], the evidence of the WAL at low temperature does not exclude the presence of surface topological states also at RT.

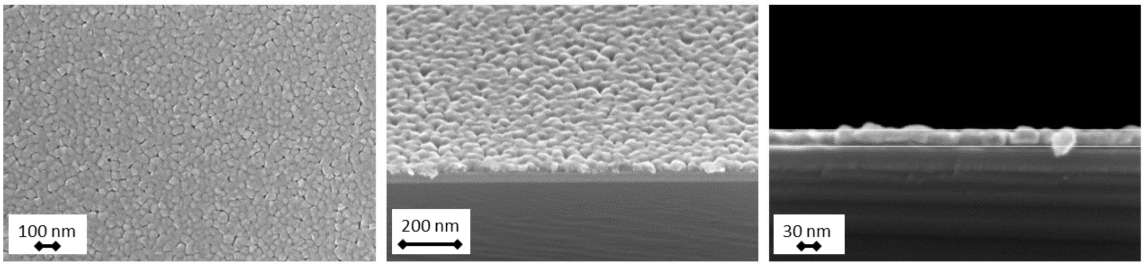

(a) Top View (b) Tilted View (c) Side View

Figure 3.1: SEM images of the granular Sb_2Te_3 thin film deposited by MOCVD taken from Ref.[102].

In order to investigate on the chemical-structural properties of the granular Sb_2Te_3 thin films, GIXRD and XRR analyses were performed. In Fig.3.2(a) the GIXRD pattern of the Sb_2Te_3 film is reported. Here, the marked crystallinity of this material is demonstrated by the presence of relatively sharp diffraction peaks belonging to the rhombohedral crystalline structure (space group R-3m). The identification of the lattice parameter was obtained by the Rietveld refinement of the GIXRD collected data (Fig.3.2(a) red line), which provided the value of $a, b = 4,27$Å and $c = 30.06$Å. The latter values are in accordance with those found in literature for the same material [102], although a slight reduction of the c-axis was observed. As compared to the powder diffraction pattern (Fig.3.2 bottom), in our film a higher intensity of the (003) and (006) peaks is observed.

This feature can be attributed to a texturization of the Sb_2Te_3 film, corresponding to a $[00\ell]$ out-of plane preferential orientation of its crystalline grains and it is often accompanied by a comparable increasing of the (009) reflection[Anderson]. The latter feature is not easily appreciable due to the proximity of the (015) peak, which turned out to be broadened due to the the contribution of the amorphous part of the Sb_2Te_3 crystalline structure. In order to confirm this picture, in Fig.3.2(c) the XRD measurements in Bragg-Brentano geometry (BB-XRD) are reported for the same sample. These measurements allow the determination of a preferential out of plane orientation of the crystalline grains in a thin film. If it is present, a fully OOP orientation of a particular family of crystalline planes is identified by the presence of spots lying on the bisector between the ω and 2θ axes. In our samples Sb_2Te_3, the presence of faint lines in place of spots provides different information. The main one is that their position indicates that the film is OOP oriented along the $[00\ell]$ direction. Moreover, the extension of these lines up to very small ω values, corresponding to high mosaicity, allowed us to perform the X-ray diffraction characterization in the GIXRD configuration, obtaining the same information achievable by the Bragg-Brentano geometry. In Fig.3.2(c) we notice also that the line corresponding to the (0 1 5) plane, the main peak in the powder, is present only for small ω values, thus due to the higher volume involved in the measurement for such small angles.

3.1.2 Fe/Sb_2Te_3 heterostructure

A $^{54}Fe(10nm)/^{57}Fe(1nm)$ bilayer was deposited by PLD on a granular Sb_2Te_3 substrate (Section 2.1.3). As emerges by the GIXRD pattern shown in Fib.3.2(b) performed on the whole $^{54}Fe(10nm)/^{57}Fe(1nm)/Sb_2Te_3$ stack, the polycrystalline nature of the Fe bilayer is evidenced by the the sharp peak at $2\theta = 44.3°$ due to the reflection by the (110) planes of the Fe body-centered-cubic(bcc) crystalline structure. The nature of the other peaks is attributable to Sb_2Te_3, and being their position unaltered as compared with the the bare substrate, we can assert that the Fe deposition did not affect the Sb_2Te_3 bulk stoichiometry. Of course the XRD/XRR analysis cannot distinguish between the two Fe isotopes ^{54}Fe and ^{57}Fe, and we refer here to the $^{54}Fe/^{57}Fe$ bilayer simply as Fe. Thus, in order to obtain information on the Fe/Sb_2Te_3 interface, XRR measurements were performed on the sample. In Fig.3.3 the XRR collected data and their best fit obtained

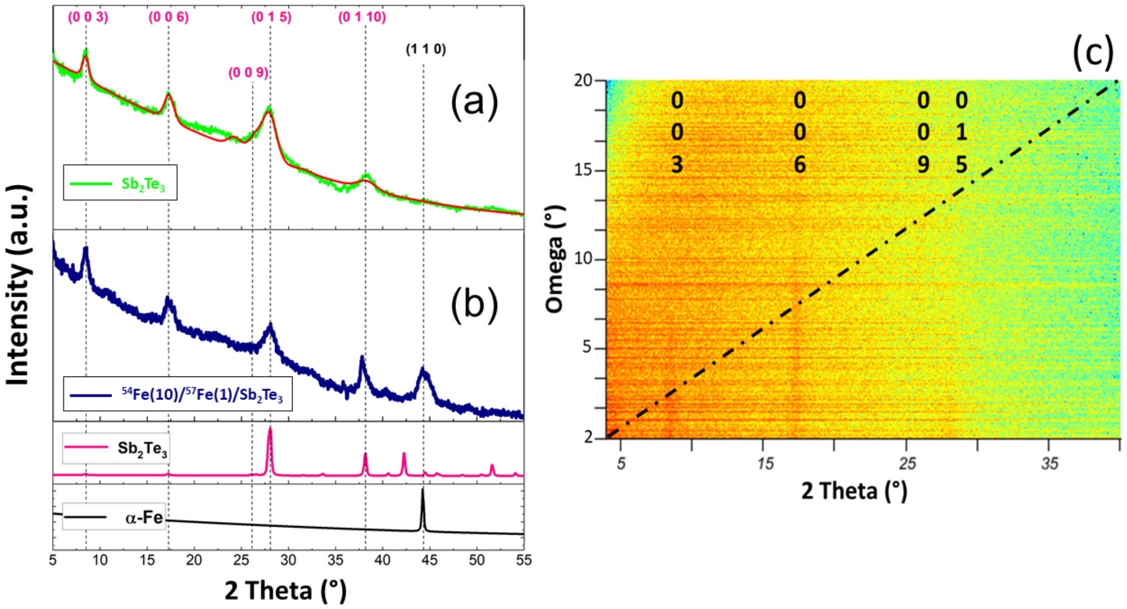

Figure 3.2: (a) GIXRD pattern of the Sb_2Te_3 granular thin film. The red curve represents the Rietveld refinement of the collected data. (b) GIXRD pattern of the Fe/Sb_2Te_3 bilayer. At the bottom of figures (a) and (b) the powder diffraction patterns of the Sb_2Te_3 and Fe phases are shown. (c) XRD pattern acquired in Bragg-Brentano geometry. The faint lines corresponding to the (003) and (006) peaks indicates that the Sb_2Te_3 film is OOP oriented along the $[00\ell]$ direction.

with a layered model are reported both for the bare Sb_2Te_3 substrate and the whole Fe/Sb_2Te_3 structure. From the best fit, the thickness, roughness and electronic density for each layer were extracted and summarized in Table3.1. The Fe/Sb_2Te_3 heterostructure exhibits a six-layered structure, with the ρ_e values in very good agreement with those tabulated. In addition to the expected surface FeO - due to the absence of any capping layer - Fe and Sb_2Te_3 layers, two further interlayers were observed, at both the Sb_2Te_3/SiO_2 and Fe/Sb_2Te_3 interfaces. Likely due to a partial segregation of oxygen, the interlayer found in proximity of the Sb_2Te_3/SiO_2 interface was modeled as an Sb_xO_y compound. More interestingly, the ρ_e value for the interlayer at the Fe/Sb_2Te_3 interface turned out to be compatible with the formation of a FeTe compound. This result is sustained by the presence of a TeO_2 surface layer on the bare Sb_2Te_3 substrate prior to Fe deposition (Table3.1). The presence of such interlayers did not emerge by the presence of further peaks in the GIXRD pattern (Fig.3.2(b)), being most likely amorphous or too thin to be detected with this technique.

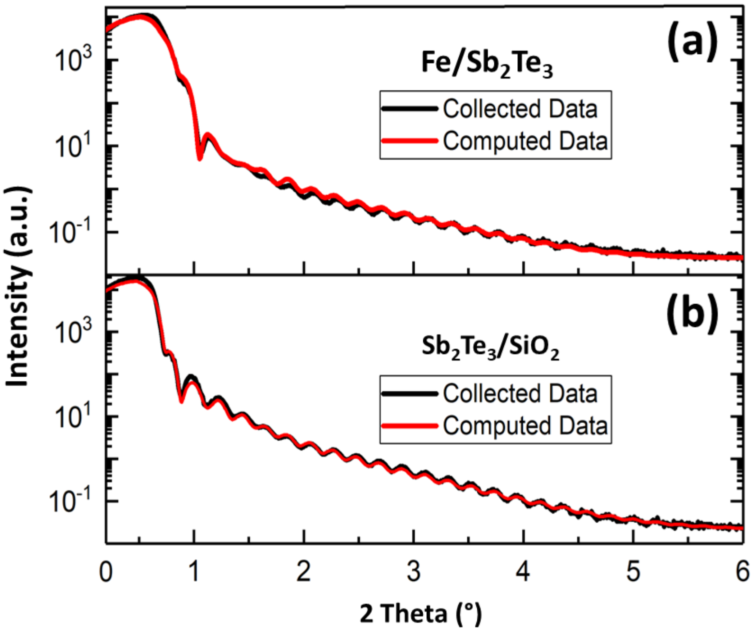

Figure 3.3: In (a)and (b) the black line represents the XRR collected data on the Fe/Sb_2Te_3 and Sb_2Te_3 samples respectively. The red line indicates the fit of the XRR data and the extracted values are reported in Table3.1.

Table 3.1: XRR parameter for the Fe/Sb_2Te_3 and Sb_2Te_3/SiO_2 samples obtained from the fit reported in Fig.3.3. In the central column the measured and the nominal values of the electronic density ρ_e are reported. The error bar on the thickness and roughness values is $\pm 0.1nm$ and $\pm 0.005e^-\text{Å}^{-3}$.

Fe/Sb_2Te_3	Thickness (nm)	ρ_e (meas./nom.) ($e^-/\text{Å}^3$)	Roughness (nm)
FeO	2.8	1.7/1.6	2.8
Fe	7	2.1/2.2	2.2
Interlayer FeTe	2.4	1.7/1.7	2.1
Sb_2Te_3	20.6	1.6/1.6	2.9
Interlayer Sb_yO_x	2	1.5	0.4
SiO_2	40.9	0.8/0.8	0.4
$Sb_2Te_3\backslash SiO_2$			
TeO_2	3.6	1.5/1.5	3
Sb_2Te_3	27.7	1.6/1.6	2.1
Interlayer Sb_yO_x	1.9	1.5	0.6
SiO_2	41.5	0.8/0.8	0.4

In order to investigate deeply on the origin of the chemical composition of the Fe/Sb_2Te_3 interface, we performed a ToF-SIMS analysis on the bare Sb_2Te_3, as shown in Fig.3.4.

Here, the evolution of the oxygen was monitored by plotting the OH signal (black marker) and the SbO line (light-blue marker) rises near the SiO_2 substrate, suggesting the formation of a SbO-like layer at the Sb_2Te_3/SiO_2 interface. Differently, the purple line indicates the evolution of the TeO signal, which clearly increases while approaching Sb_2Te_3 surface, thus compatible with the formation of a TeO_x enriched Sb_2Te_3 surface. This scenario is totally in accordance with the XRR data for the Sb_2Te_3 sample. Based on both the ToF-SIMS and XRR measurements, we conclude that the favored formation of a Te-rich Sb_2Te_3 surface serves as a Te reservoir for the FeTe compound formation at the Fe/Sb_2Te_3 interface following Fe deposition.

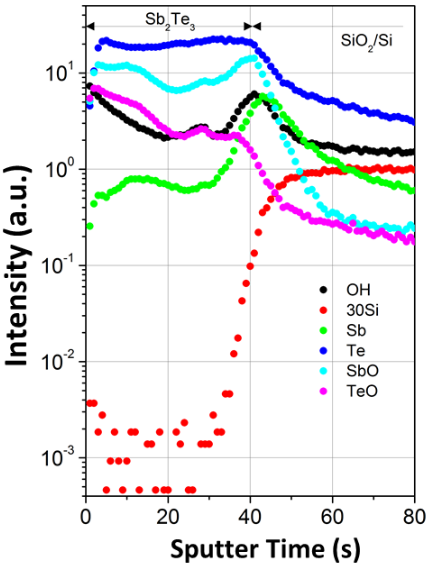

Figure 3.4: ToF-SIMS measurement of the bare Sb_2Te_3 substrate. Each colored signal refers to an element or a compound indicated by the legend in the figure.

As introduced in subsection 2.2.4.5, the choice to deposit a $^{54}Fe(10nm)/^{57}Fe(1nm)$ bilayer was to allow the interface sensitive CEMS analysis, being CEMS only sensitive to ^{57}Fe atoms. Moreover, the deposition of 1 nm thick layer of ^{57}Fe in contact with Sb_2Te_3 gave us the possibility to investigate on the chemical-structural and magnetic environment of the ^{57}Fe atoms at the $^{57}Fe/Sb_2Te_3$ interface. In Fig.3.5 the CEMS spectrum for the $^{54}Fe(10nm)/^{57}Fe(1)/Sb_2Te_3$ sample is reported. A CEMS signal can be divided in four components: (i)$\alpha-Fe$, (ii) DIST, (iii) DOUB-1 and (iv) DOUB-2. As a result of the fit, for each of these components the hyperfine parameters are extracted and reported in Table 3.2, where $< B_{hf} >$ is the average hyperfine magnetic field, δ is the isomer shift, ΔE_Q is the quadrupole splitting, $< \Gamma >$ is the average linewidth and A_{25} the ratio between the lines (1,6) and (2,5) of the magnetically-split components. The Area (%) is the relative area of the fitting components assuming the Debye-Waller factor 1 for all the components. The $\alpha - Fe$ component is referred to the Fe atoms in an unperturbed local environment. On the contrary, DIST is a distribution of magnetically-split sextets where the $< B_{hf} >$ value is slightly lower than in pure Fe, in this case most likely coming from the ^{57}Fe atoms in direct contact with the Sb_2Te_3 surface. It happens because here a bonding hybridization of the ^{57}Fe atoms can occur, thus lowering the $< B_{hf} >$ value and enhancing the isomer shift ΔE, pointing towards a lower electronic density of the ^{57}Fe atoms as compared to the pure bcc environment. The overall magnetic fraction ($\alpha - Fe$+DIST) out of the 1 nm thick layer of ^{57}Fe in contact with Sb_2Te_3 is $\sim$ 48%. According to the values of A_{25} (Table3.2), the magnetization of the Fe film lies always in the film plane.

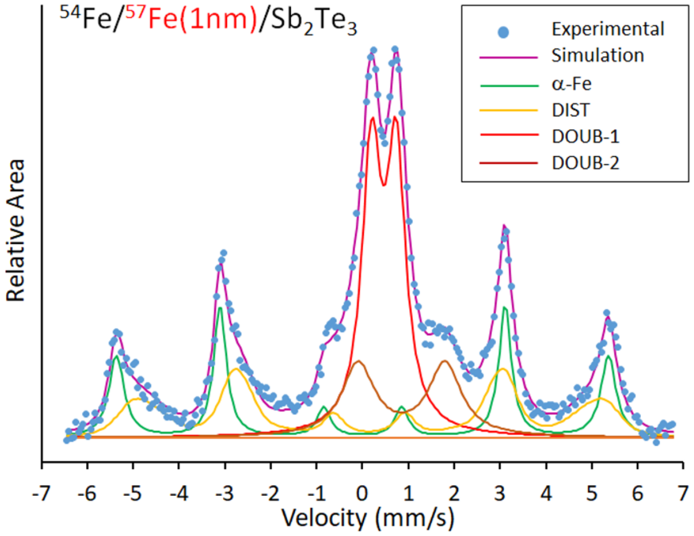

Figure 3.5: CEMS collected signal for the $^{54}Fe(10nm)/^{57}Fe(1nm)/Sb_2Te_3$ heterostructure. The meaning of the extracted CEMS signal components (colored lines) is discussed in the text. Taken from Ref.[102].

For what concern the remaining ^{57}Fe atoms, they coordinate paramagnetically as accounted by the doublets DOUB-1 and DOUB-2. The hyperfine parameters of the DOUB-1 component are in very good accordance with those previously reported for the FeTe

Table 3.2: CEMS hyperfines parameters for the $^{54}Fe(10nm)/^{57}Fe(1nm)/Sb_2Te_3$ sample and extracted from the fit of Fig.3.5

Parameters	α-Fe	DIST	DOUB-1	DOUB-2
$\langle B_{hf} \rangle$ (T)	33,2(2)	30,3(2)	–	–
δ (mm/s)	0	0,14(1)	0,46(1)	0,85(1)
ΔE_Q (mm/s)	0	0	0,54(1)	1,89(2)
$\langle \Gamma \rangle$ (mm/s)	0,37(1)	0,5	0,50(1)	0,87(1)
A_{25}	4	4	–	–
Area (%)	22.9	25	35.5	16,6

compound.[105, 106] As compared to Ref.[105, 106], we noticed a slight increase of the ΔE_Q value as compared the previously reported value for FeTe. The latter is attributed to a local distortion of the FeTe phase due to interface effects, which is highly plausible given the granular nature of the Sb_2Te_3 substrate. Interestingly, the DOUB-1 component attributed to the FeTe compound is the most relevant contribution to the CEMS signal, accounting for $\sim 35.5\%$ of the $^{57}Fe(1)/Sb_2Te_3$ interface and thus demonstrating that Fe atoms preferentially bond with Te. This finding is a strong confirmation of what emerged by XRR and ToF-SIMS analysis. Finally, the DOUB-2 is associated to the formation of FeO_x compound, as suggested by its isomer shift value that points towards a Fe^{2+} electronic configuration.[107]

At first sight, a correct identification of DOUB-2 is not trivial, being its hyperfine parameters also compatible with the formation of $FeSb_2$ compounds, as reported in Ref. [108]. Moreover, an alternative magnetic nature of DOUB-2 could be possible, because an alternative fitting strategy was attempted using a broad distribution of magnetically-split sextets with an average field of $< B_{hf} >\sim 10T$ (not shown). Anyway, the results presented in the next section and reported in Ref.[103] undoubtedly inked the DOUB-2 CEMS component to the presence of the FeO_2 phase.

As a result of the thorough investigation on both the $^{54}Fe(10nm)/^{57}Fe(1)/Sb_2Te_3$ and Sb_2Te_3/SiO_2 heterostructures performed by means of XRD/XRR, ToF-SIMS and CEMS techniques, a marked reaction at the Fe/Sb_2Te_3 interface was evidenced. In particular, thanks to the interface CEMS analysis, it was observed that a relevant fraction ($\sim 35.5\%$) of the 1 nm thick Fe layer in contact with the Sb_2Te_3 surface reacts with Te to form FeTe.

The preferential bonding mechanism between Fe and Te turned out to be associated to a Te enrichment at the Sb_2Te_3 surface, thus the obtained results suggest a possible general interaction between Fe and the chalcogen element in chalcogenide-based TIs, as also observed from others in similar structures.[109] Moreover, in our study reported in Ref. [103] the chemical stability of the FeTe compound at the interface of Fe/Sb_2Te_3 systems was demonstrated up to 200°C, thus confirming the strong tendency of the Fe atoms to bound with the elemental Te.

For any spintronic device, the presence of paramagnetic phases at the FM/TI interface could be detrimental. In particular, in SP or SOT experiments this could lead to a less efficient SCC. Moreover, from the technological point of view, the growth of FMs is often conducted ex-situ, after the synthesis of the TI. For that, the TI surface is usually protected by a capping layer during the transfer.[18] An effective removal of the capping layer can be not straightforward and the presence of unwanted interlayers could be detrimental for spin-to-charge conversion application. Despite that, as reported by H. An *et al.* and A. Ruiz-Calaforra *et al.* in Ref.[110] and Ref.[111] respectively, the presence of species or interlayers could give rise to unexpected enhanced SCC phenomena in FM/Oxide or FM/Interlayer/NM heterostrutures, thus the trade-off between benefits and criticalities is still controversial. Therefore, in the next section, the role of mild and rapid thermal treatments is discussed as a possible solution to improve the Fe/Sb_2Te_3 interface quality.

3.1.2.1 Fe/Sb_2Te_3 annealing for the interface quality improvement

Being aware about the benefits that thermal treatments could offer for the improving of the interface sharpness in Fe/oxide systems, as a first attempt to improve the Fe/Sb_2Te_3 interface, the same Rapid Thermal Annealing (RTA) process used in Ref.[99] was used. Here, a mild RTA composed by two steps is proposed: Ramp up ($RT \rightarrow 200$ °C, 10 sec.); Heating (200 °C, 10sec.); Cooling down (200 °C $\leftarrow RT$, 6 min.)). In Fig. 3.6(a) are reported the GIXRD pattern of the $^{54}Fe(10nm)/^{57}Fe(1nm)/Sb_2Te_3$ sample already discussed in Section 3.1.2 prior (blue line) and upon (red line) RTA. Here, clear changes on the diffraction pattern are visible as a consequence of the thermal treatment. For what concern the Sb_2Te_3 peaks, we notice that the (003) and (006) peaks are not sig-

nificantly affected by the RTA. Differently, most changes are clearly visible for the (015) and (01 10) reflections. Indeed, the intensity of the (015) peak decreases and the (01 10) reflection almost disappears, an indication that the amorphous part of the film and crystalline orientation different from the $[00\ell]$ direction tend to reorganize. Looking at the Fe(110) peak, just a slight reduction is visible, which is a proof that the Fe crystallization persists almost unchanged. The lower intensity of the Fe(110) peak could suggest that in the annealed Fe/Sb_2Te_3 structure part of the Fe atoms coordinate in a new phase, different from the previous $\alpha - Fe$. On the other hand, a very intense peak appears at $2\theta = 32.5°$. This anomalous peak formation indicates that a new energetically favored crystalline phase arises as a consequence of the thermal budget provided to the sample. From the CEMS analysis in Fig.3.5, the presence of a distorted FeTe crystalline phase was evidenced at the Fe/Sb_2Te_3 interface. In view of this, we attributed the anomalous peak rise to the formation of a non-stoichiometric or distorted FeTe crystalline phase. At the bottom of Fig.3.6(a), the FeTe powder diffraction pattern is reported and compared with the anomalous peak at $2\theta = 32.5°$. What emerged was that the main peak of the cubic FeTe phase could be compatible with a distorted FeTe crystalline phase.
Fig.3.6(b) shows the ToF-SIMS performed on the annealed $^{54}Fe(10nm)/^{57}Fe(1nm)/Sb_2Te_3$ sample. Despite what discussed above concerning the GIXRD analysis, ToF-SIMS clearly evidenced that the ^{57}Fe and ^{54}Fe atoms heavily diffuse into the Sb_2Te_3 substrate, with an overall damage of the interfaces and the FeTe fraction likely distributed across the whole stack.

As it is clear by this results also a mild 200 °C RTA was proved to be detrimental for the interface quality, due to the large enhancement of the elemental interdiffusion at the Fe/Sb_2Te_3 interface. In view of that, we decided to explore an alternative strategy. A new set of samples was prepared and the RTA was performed prior to the PLD of Fe. Also in this case, the Fe layer was composed by a $^{54}Fe(10nm)/^{57}Fe(1nm)$ bilayer to allow the interface CEMS analysis. In Table3.3, the different thermal recipes are summarized for each sample and for simplicity we named the $^{54}Fe(10nm)/^{57}Fe(1nm)/Sb_2Te_3$ samples according to the performed RTA temperature as follow: SN - as deposited; S150 - RTA at 150 °C; S200 - RTA 200 °C.
In Fig.3.7(a) and (b) the XRR data for the SN and S200 samples is reported and the parameters extracted from the fit reported in Table3.4. The system here is modeled

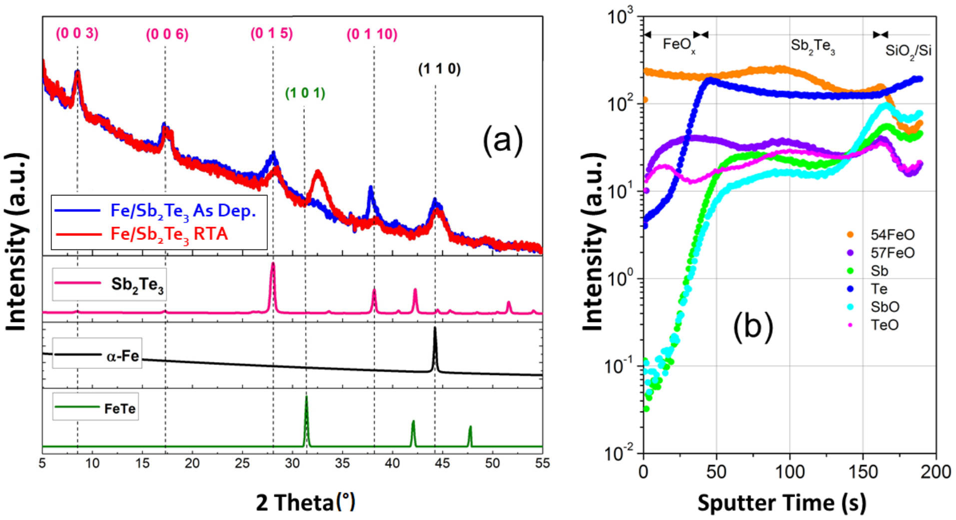

Figure 3.6: (a) GIXRD pattern of the Fe/Sb_2Te_3 heterostructure prior (blue line) and post (red line) annealing. At the bottom the powder diffraction pattern of the phases of interest are reported. (b) ToF-SIMS signals of the sample Fe/Sb_2Te_3 upon RTA. The evolution of the signals indicates that the layered structure of the sample was compromised due to the interdiffusion of the ^{57}Fe and ^{54}Fe atoms into the Sb_2Te_3 substrate. Figure taken from Ref.[102].

Table 3.3: List of samples and relative thermal treatment prior to Fe deposition. The stack is the same for the SN, S150 and S200 samples, but the thermal treatment is different as indicated on the right side of the table.

		RTA steps on Sb$_2$Te$_3$ (prior to Fe deposition)		
Sample	Stack	Ramp up	Heating	Cooling down
SN	^{54}Fe(10 nm)/^{57}Fe(1 nm)/Sb$_2$Te$_3$/SiO$_2$/Si	None	None	None
S150	^{54}Fe(10 nm)/^{57}Fe(1 nm)/Sb$_2$Te$_3$/SiO$_2$/Si	RT $\overset{10\,s}{\Rightarrow}$ 150 °C	150 °C $\overset{10\,s}{\Rightarrow}$ 150 °C	150 °C $\overset{250\,s}{\Rightarrow}$ RT
S200	^{54}Fe(10 nm)/^{57}Fe(1 nm)/Sb$_2$Te$_3$/SiO$_2$/Si	RT $\overset{10\,s}{\Rightarrow}$ 200 °C	200 °C $\overset{10\,s}{\Rightarrow}$ 200 °C	200 °C $\overset{250\,s}{\Rightarrow}$ RT

using five layers with no need of any interlayer at the Fe/Sb_2Te_3 interface. Moreover, the thickness and the electronic density of the layers are not affected by the RTA process, preserving the stack. Interestingly a slight reduction of the Fe and Sb_2Te_3 surfaces is observed, characteristics which point towards the formation of a sharper Fe/Sb_2Te_3 interface upon RTA.

Despite the XRR analysis detected small differences from the SN and S200 samples up

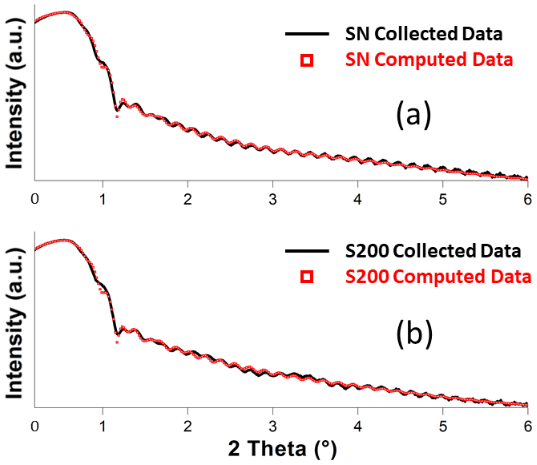

Figure 3.7: XRR collected spectra (black solid lines) and the computed model for the samples (a) SN and (b) S200. Figure taken from Ref.[103].

Table 3.4: Parameters extracted from the fit of the XRR curves reported in Fig.3.7. In (a) and (b) the collected data and their fit are reported for the SN and S220 samples respectively. Table taken from Ref.[103].

Layers	Thickness [nm]	ρ_e [$e^- \text{Å}^{-3}$]	Roughness [nm]
	SN/S200	SN/S200 [nominal]	SN/S200
FeO	2.8/3.1	1.7/1.7 [1.6]	2.4/2.3
Fe	6.2/6.3	2.2/2.2 [2.2]	2.4/2.0
Sb_2Te_3	27.7/27.7	1.5/1.5 [1.6]	2.3/2.1
Sb_2O_3	1.6/1.5	1.4/1.5 [1.5]	0.2/0.1
SiO_2	50.0/50.3	0.8/0.8 [0.8]	0.4/0.4

the RTA of the Sb_2Te_3 substrate, the crystal quality of both the Fe and Sb_2Te_3 layers turned out to be largely affected by the thermal process.

In Fig.3.8 the GIXRD pattern for all the samples is reported, together with the powder diffraction patterns of the Fe and Sb_2Te_3 crystalline phases for comparison. As discussed in section 3.1.1, the Sb_2Te_3 structure is highly textured, with an OOP orientation along the [00ℓ] direction, as proved by the intensity of the (003), (006) and (009) peaks as compared to the powder. Anyway, the overall crystallinity of the Sb_2Te_3 film can slightly vary with the deposition run. Indeed, for seek of completeness, we point out that the overall crystallinity of the Sb_2Te_3 films discussed below is higher if compared with those reported in Section 3.1.1, which is accompanied by an higher orientation of the crystalline grains along the $[00\ell]$, as emerges from the lower intensity of the (015) peak in the as deposited sample. In Fig.3.8(d) and (e), the FWHM of the Sb_2Te_3 (003) and Fe (110) peaks is reported. In Fig.3.8(d),we observed that the peaks relative to the $[00\ell]$ direction becomes higher and sharper as a function of the RTA temperature. This behavior corresponds to an improvement of the Sb_2Te_3 crystallization, indicating that the amorphous fraction of the as-deposited Sb_2Te_3 film becomes crystallized and oriented along the $[00\ell]$ direction. The effect of the thermal budget provided to the sample is visible also from the higher intensity of the other Sb_2Te_3 diffraction peaks, as clear at $2\theta \sim 38°$ in Fig.3.8. In Fig.3.8(d) the evolution of the Fe (110) peak is reported and, interestingly, we notice that the RTA on the bare Sb_2Te_3 prior to Fe deposition influenced the crystalline quality of the Fe layer. Indeed, also the FWHM of the Fe(110) peak reduces with the annealing temperature, while the intensity increases, pointing towards the formation of larger crystalline grains in the annealed S200 sample.

Similarly to what we did previously, we employed ToF-SIMS in order to monitor the elemental interdiffusion between Fe and Sb_2Te_3. In Fig.3.9 (a) and (b), the ToF-SIMS measurements for samples SN and S200 are reported respectively. Once again, the higher sensitivity for the Fe atoms detection was obtained by tracking the ^{57}FeO and ^{54}FeO respectively the green and orange lines. Observing the evolution of the curves, the stacking order of the layer is respected, with the ^{54}Fe layer on top of the stack. More importantly, after $\sim 45sec$ of sputtering time, the ^{57}Fe shows a relative maximum in both the SN and S200 samples, which is due to the presence of the $^{54}Fe/^{57}Fe$ interface. On the contrary, in the case of an ideal intermixing between ^{54}Fe and ^{57}Fe the pile up effect would be lost and the ^{57}Fe signal flattened. Moreover, moving toward longer sputtering times, the intensity decay of the ^{57}FeO and ^{54}FeO signals is different, thus confirming the transition from a ^{57}Fe-enriched region despite the knock of the ^{54}Fe due to the sputtering. The Te and Sb profiles result very similar in both samples, suggesting that the RTA did not promote elemental diffusive effects. The Te and Sb signals quickly drop in the FeO_x matrix at comparable values in the two samples, suggesting a similar amount of diffused elements. Further, the slope of the Te signal is similar in both the SN and S200 samples, with a marginal reduction in S200 associated with the loss of the pile up in intensity at the $^{54}Fe/^{57}Fe$ interface and probably related to a very small

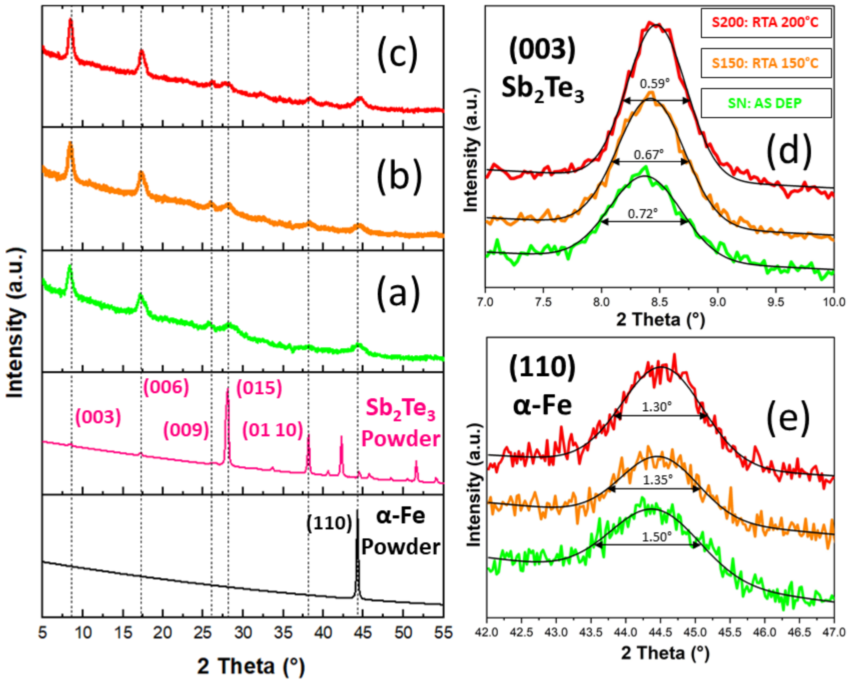

Figure 3.8: GIXRD pattern of samples (a) SN, (b) S150 and (c) S200. In (d) and (e), the particular of the evolution of the Sb_2Te_3 (003) and Fe (110) peaks as a function of the RTA is showed respectively. Figure taken from Ref.[103].

Te diffusion in the FeO_x layer. Also the Sb signal shows a drop across the $^{54}Fe/^{57}Fe$ interface with nearly the same slope in SN and S200. Nicely, within the technique limit, no relevant Sb diffusion is detected in the Fe layer, pointing towards a clean $^{54}Fe/^{57}Fe$ interface.

As a first magnetic characterization on the new set of samples we performed VSM on the SN and S200. Fig.3.10 shows the magnetic hysteresis loops for the sample SN (blue curve) and S200 (red curve) acquired by VSM at RT with the external magnetic field applied in the film plane. From the shape of the hysteresis loops, in both samples the easy axis of the magnetization lies IP of the Fe layer and the hard axis is along the OOP direction, as evident from the comparison between the green and the red/blue lines in the inset of Fig.3.10. This result is in accordance with the shape anisotropy (Eq.2.20) contribution in such thin films. The value for the saturation magnetization M_s for the SN and S200 samples is around 1600 $emucm^{-3}$(or kAm^{-1}), which is very similar to that reported for bulk $\alpha - Fe$ (1700 kAm^{-1}). The latter result confirms the

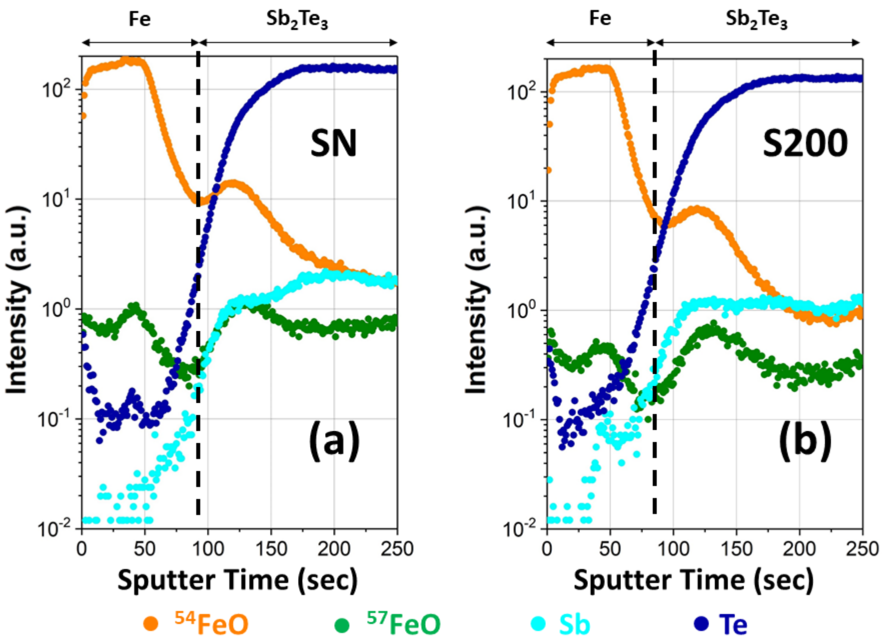

Figure 3.9: ToF-SIMS measurements of (a) SN and (b) S200 samples. A qualitative comparison between the two datasets proved that the RTA preserved the interfaces stability between layers. Figure taken from Ref.[103].

high magnetic quality of the Fe film, despite the lack of any capping layer (FeO_x on the surface, Table3.4).

The squareness of an hysteresis loop is defined as the ratio between the magnetization at the remanence (y-axis interception) and at the saturation. In our sample the squareness is around the 70%, compatible with the polycrystalline structure of the film. Interestingly, the coercive field turned out to be slightly affected by the RTA, passing from 22 Oe in SN to 16 Oe in S200. As discussed above following the GIXRD analysis as a function of the temperature, the RTA on the S200 sample promoted the formation of larger Fe crystalline grains. The larger Fe grains could correspond to larger magnetic domains in the Fe layer, thus possibly connected with the reduction of the coercive field in the S200 sample. In the context of spintronic devices, the decrease of the coercive field of a FM when in contact with a 3D-TI could be beneficial, because of the reduction of the energy required to switch the magnetization of the FM layer through SOT effect at the FM/TI interface.

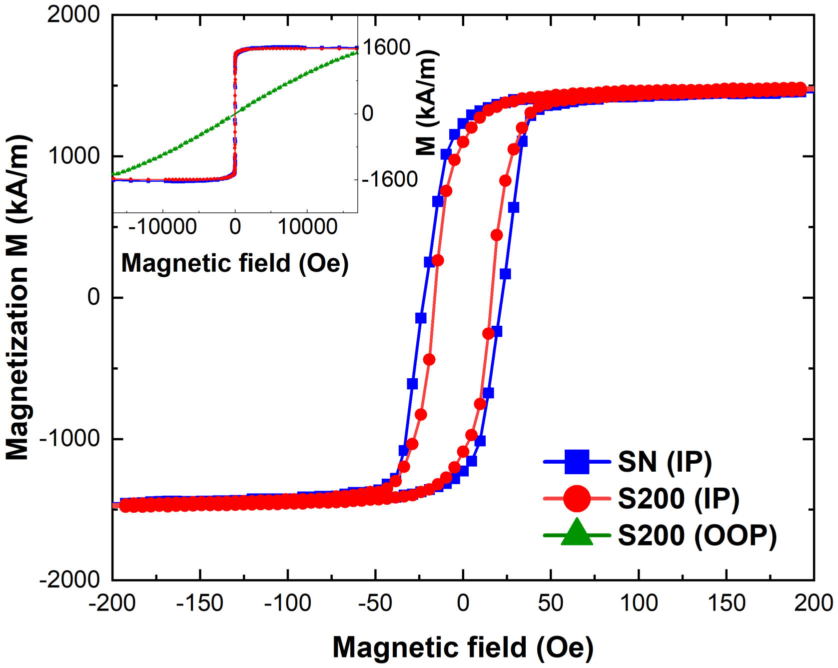

Figure 3.10: VSM measurement is the SN(blue) and S200(red) samples. The external magnetic field is maintained IP. The inset shows the comparison between the VSM hysteresis loops when the magnetic field is positioned IP (red/blue curves) and OOP (green curve). The error bar for the determination of M_s is within the 5%. Figure taken from Ref.[103].

In Fig.3.11 the CEMS analysis on the samples SN,S150 and S200 in shown. As in Fig.3.5, all the CEMS spectra can be fitted with the four components $\alpha - Fe$, DIST, DOUB-1 and DOUB-2 and the extracted hyperfine parameters are reported in Table3.5.

The fitting strategy was to fix the value of the hyperfine parameters for all the fitted components in SN, S150 and S200, while the relative areas (Fig.3.11(b)) and the $< B_{hf} >$ of the DIST component (Table3.5) are the free parameters of the fit. The identified CEMS components are exactly the same as previously discussed in Section 3.1.2, thus $\alpha - Fe$ refers to the unperturbed Fe atoms, DIST to a broadened magnetic distribution due to the under-coordinated Fe atoms and the doublets DOUB-1 and DOUB-2 are associated with the two paramagnetic phases FeTe and FeO_x (or FeSb) respectively. In accordance with the VSM results (Fig.3.10), the A_{25} value associated with the ferromagnetic portion

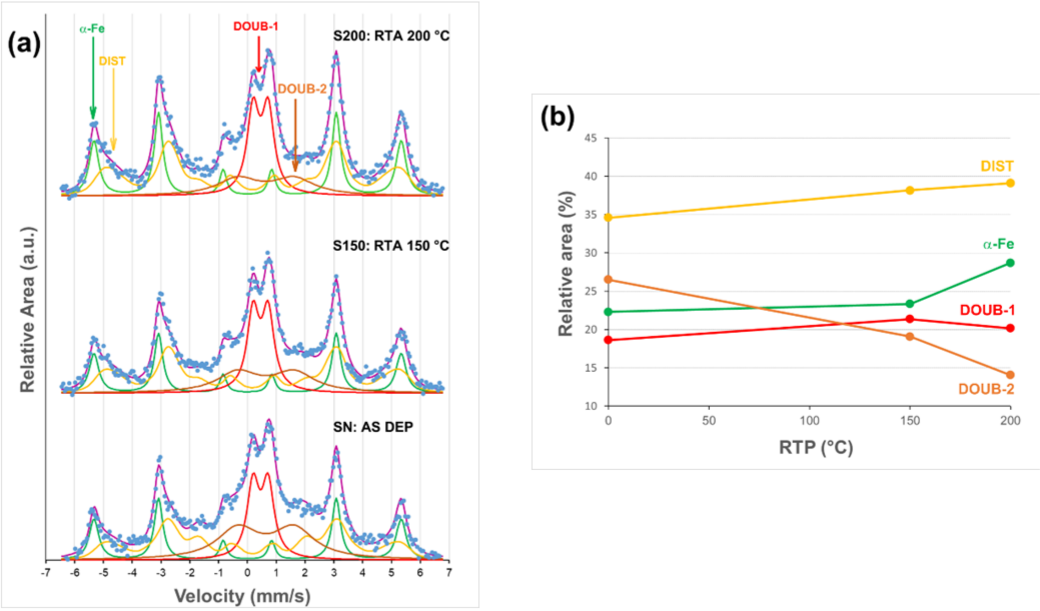

Figure 3.11: CEMS measurements of sample SN,S150 and S200. The blue points indicate the experimental data and the solid purple line the simulated fit obtained from the sum of the $\alpha - Fe$, DIST, DOUB-1 and DOUB-2 components. (b) RTA dependence of the relative area for the four fitting components. Figure taken from Ref.[103].

Table 3.5: Parameters extracted from the fit of the CEMS data shown in Fig.3.11. If the experimental error is not indicated for a certain parameter, it means that it was fixed during the fitting procedure. Table taken from Ref.[103].

	Parameters	α-Fe	DIST	DOUB-1	DOUB-2
	δ (mm s^{-1})	0,0	0,17(1)	0,46(1)	0,64(2)
	ΔE_Q (mm s^{-1})	0,0	0,0	0,52(1)	1,95(3)
SN	$<B_{hf}>$(T)	33,02(3)	26,58(3)	–	–
S150	$<B_{hf}>$(T)	33,02(3)	28,57(3)	–	–
S200	$<B_{hf}>$(T)	33,02(3)	28,82(3)	–	–
	$<\Gamma>$ (mm s^{-1})	0.35(1)	0.5	0.5	1,72(4)
	A_{25}	4	4	–	–

of the ^{57}Fe film showed that the magnetization vector lies always IP. What can be deduced from Fig.3.11(b) is that both the B_{hf} and DIST components increase in the S200 sample, when compared to SN. This fact strongly supports the hypothesis that, upon the RTA of Sb_2Te_3, the Fe atoms at the Fe/Sb_2Te_3 interface tend to reorganize towards a pure $\alpha - Fe$ configuration. In particular, we detected an $\sim$ 8% increase of the B_{hf} for the DIST component from SN to S200 (Table3.5), which reflects an overall increase of the magnetic moment at the Fe/Sb_2Te_3 interface. Looking at the overall chemical, structural and magnetic picture provided by Fig.3.5(b), is clear that a gradual increase of the magnetic fraction ($\alpha - Fe + DIST$) of $\sim$ 11% took place. Furthermore, a correspondent lowering of the DOUB-2 paramagnetic component is observed, from $\sim$ 27% to $\sim$ 14%. Based on the present findings, we attributed the DOUB-2 component to the FeO_x compound.

Differently from all the other CEMS components, DOUB-1 was affected by a negligible change as a function of the RTA temperature. Being DOUB-1 associated to the formation of the FeTe compound, this result nicely supports previous insights about a strong tendency of the Fe atoms to bond with chalcogen atoms in chalcogenide-based TI.[102, 109] The presence of this small amount of interfacial FeTe could influence the spin-to-charge conversion efficiency at the Fe/Sb_2Te_3 interface, but its role is difficult to determine and in general it could be detrimental. On the other hand, the stabilization of a crystalline FeTe phase may give rise to superconductivity in Fe/FeTe/Sb_2Te_3 heterostructures, thus opening perspectives towards the study of the exotic interplay between topology, superconductivity and magnetism to investigate on the elusive Majorana fermion, as previously proposed.[106, 112, 113] Motivated by the latter reasons, in the following a thermodynamic picture about the formation of FeTe in Fe/Sb_2Te_3 systems and a comparison with some related literature are provided.

Vobornik et al.[114] and Walsh et al.[37] reported the favorable stability of the FeTe compound based on thermodynamics considerations for different FM/TI compounds. The standard-state Gibbs free energy variation was evaluated using the equation $\Delta G^0 = \Delta H^0 - T\Delta S^0$, where ΔH^0 and ΔS^0 are the changes in entalpy and entropy respectively. T indicates the temperature and it is fixed at 298 K, thus we can write $\Delta G^0(H, S)$. In Ref.[114] the authors considered the possible reactions taking place at the Fe/Bi_2Te_3 interface using a standard thermodynamics tabulation [REF], and discussed the natural tendency of Fe atoms to react with Bi_2Te_3 forming $FeTe_{0.9}$ ($\Delta G^0_{FeTe_{0.9}}$ spans from - 4.5 to 0.5 $kJ/mol \cdot Fe$) and $FeTe_2$ ($\Delta G^0_{FeTe_2}$ spans from - 17.5 to - 6.6 $kJ/mol \cdot Fe$) compounds. The same approach was used in Ref.[37] for the Fe/Bi_2Se_3 heterostructure, pointing out, also in this case, the high reactivity betweem Fe and Se atoms. Here, the formation of Fe_3Se_4 ($\Delta G^0_{Fe_3Se_4} = -244.0 kJ/mol \cdot Fe$) was found the most favorable. In this thesis we performed similar thermodynamic calculations for the Fe/Sb_2Te_3 interface and the possible chemical reaction we identified are

$$3Fe + 0.9Sb_2Te_3 \rightarrow FeTe_{0.9} + 1.8Sb \qquad \Delta G^0_{FeTe_{0.9}} = -8.09\frac{kJ}{mol \cdot Fe} \tag{3.1}$$

$$3Fe + 0.9Sb_2Te_3 \rightarrow FeTe_{0.9} + 1.8SbTe \qquad \Delta G^0_{FeTe_{0.9}} = 100\frac{kJ}{mol \cdot Fe} \tag{3.2}$$

$$3Fe + 2Sb_2Te_3 \rightarrow 3FeTe_2 + 4Sb \qquad \Delta G^0_{FeTe_2} = -34.8\frac{kJ}{mol \cdot Fe} \tag{3.3}$$

$$Fe + 2Sb_2Te_3 \rightarrow FeTe_2 + 4SbTe \qquad \Delta G^0_{FeTe_2} = 661.3\frac{kJ}{mol \cdot Fe} \tag{3.4}$$

From the latter equations, the formation of $FeTe_{0.9}$ and $FeTe_2$ compounds accompanied by the dissociation of the elemental Sb are the most favorable when Fe reacts with Sb_2Te_3. Anyway, we did not consider possibilities connected to the dissociation of Sb_2Te_3 in $FeTe_x + Sb_2Te$, since the lack of thermodynamic data in literature.

As a result of this study, the RTA is demonstrated to favor the formation of a sharper and structurally purer Fe/Sb_2Te_3 interface. The presence of oxygen on top of the Sb_2Te_3 surface is unavoidable, as far as Sb_2Te_3 is exposed to the atmosphere without a proper capping layer prior to the transfer to the PLD system for the deposition of Fe. Despite that, we demonstrated that through a proper annealing procedure of the only Sb_2Te_3 substrate prior to Fe deposition an almost complete restoration of the Sb_2Te_3 crystalline quality can be achieved, thus improving the Fe/Sb_2Te_3 quality. To a certain extent this results permits to avoid the capping-decapping procedure for the production of Fe/Sb_2Te_3 heterostructures. In principle, the proposed RTA process can be extended to other FM/TI systems, thus providing a tool for optimizing the interface quality without the use of TI capping interlayers.

From the atomic-scale study on the chemical, structural and magnetic properties of the

Fe/Sb_2Te_3 interface when Fe is deposited by PLD, emerged the importance of controlling the chemical reaction taking place at the Fe/Sb_2Te_3 interface during the Fe deposition, with the aim to avoid the formation of paramagnetic compounds in principle detrimental for spin-to-charge conversion applications. For sure in this case, the high energetics involved in the PLD process had a negative role in determining the quality of the Fe/Sb_2Te_3 interface. In order to investigate on the potential role of the energetics involved in the FM deposition on the interface quality, in the next section the ALD of Co thin films on the granular Sb_2Te_3 and the main reason behind the choice of this new FM material are discussed.

3.1.3 Co/Sb_2Te_3 heterostructure

As we deeply discussed in the previous section, the Fe/Sb_2Te_3 interface is characterized by a high reactivity, in particular between Fe and Te atoms. A similar behavior was reported by other authors [37, 114] and, interestingly, in Fig.14 of Ref.[37] the authors summarized in a scatter plot the strength of the interaction between different metals (grown by electron beam evaporation) and the Bi_2Se_3 TI. As a result, the strength of the metal-Bi_2Se_3 interaction in forming metal-Se compounds was ordered as $Au < Pd < Ir < Co \leq CoFe < Ni < Cr < NiFe < Fe$, with Fe reported as the more reactive in forming FeSe alloys. For that, Co turned out to be much less reactive than Fe when in contact with Bi_2Se_3. These evidences motivated us to conduct the ALD of Co on the Sb_2Te_3, with the aim to combine both the favored thermodynamics and the lower energetics of the process to reduce the intermixing at the Co/Sb_2Te_3 interface.

The ALD of metals is challenging due to the difficulty in the precursors preparation. [43] In 2017 Kerrigan et al. demonstrated the possibility to synthesize metallic Co by thermal ALD at relatively low temperature (170-200 °C), testing different precursors and substrates. [62, 115, 116] During my PhD activity, I visited for two months the Winter Laboratory (Detroit - U.S), being the laboratory in which Kerrigan produced the Co by ALD.

During this collaboration, I performed simultaneous growths of Co ultrathin films at 180 °C on top of $Sb_2Te_3(35nm)/SiO_2(50nm)/Si$ (set of samples previously prepared at the CNR-IMM Agrate Brianza) and $Pt(70nm)/SiO_2(10nm)/Si$ substrates, in order to investigate the role of the substrate in determining the Co structural properties (Section 2.1.3.1). In Table3.6 the ALD-grown Co-based heterostructures are reported. In the following a thorough and systematic chemical-structural and magnetic characterization of these systems is discussed.

Table 3.6: Number of cycles and Co layer thickness for each sample sample studied. The thicknesses reported here are extracted by different measurements methods as explained in the text. All the depositions were carried out at 180 °C. Figure taken from Ref.[44].

No. of cycles	Co (nm)/Sb_2Te_3	Co (nm)/Pt
100	3.5	1.8
250	8.1	6.3
1,000	50	35

In Fig.3.12 the XRR data for the Co(8.1 nm)/Sb_2Te_3 and Co(6.3 nm)/Pt samples obtained simultaneously after 250 ALD cycles of Co is shown. The two heterostructures were modeled using a multilayer stack and from the best fit of the data we extracted the thickness, roughness and electronic density of each layer (Table3.7).

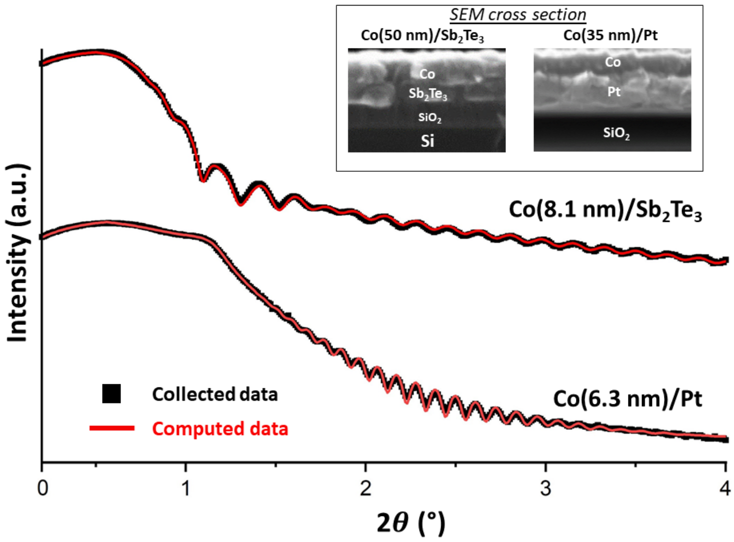

Figure 3.12: XRR measurement of the 250 cycles ALD run on the Sb_2Te_3(top graphic) and Pt (bottom graphic) substrates. In the inset SEM cross sectional view of the sample produced after 1000 cycles. Figure taken from Ref.[44].

The electronic density of Co for Co/Sb_2Te_3 sample results slightly lower than the nominal values for bulk Co ($2.37 - 2.44e^-/\text{Å}^3$), as typically observed in thin films. [102, 117]

Moreover, in order to properly model the XRR data of the Co/Pt stack it was necessary to introduce an interlayer between Co and Pt, with a ρ value within the $3.3 - 4.9e^{-}/\text{Å}^3$ range, which correspond to the values of crystalline PtO and Pt respectively.

Table 3.7: Thickness, roughness and electronic densities extracted by the XRR fit of Fig.3.12 for the Co(8.1 nm)/Sb_2Te_3 and Co(6.3 nm)/Pt samples. The uncertainty on the thickness and roughness is $\pm 0.1nm$ and $\pm 0.1e^{-1}/\text{Å}^3$ on the electronic density. Table taken from Ref.[44].

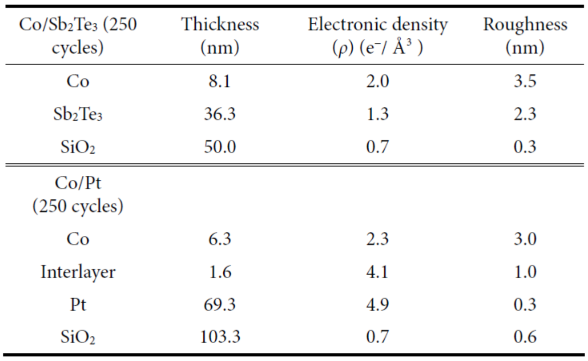

Co/Sb_2Te_3 (250 cycles)	Thickness (nm)	Electronic density (ρ) ($e^-/\text{Å}^3$)	Roughness (nm)
Co	8.1	2.0	3.5
Sb_2Te_3	36.3	1.3	2.3
SiO_2	50.0	0.7	0.3
Co/Pt (250 cycles)			
Co	6.3	2.3	3.0
Interlayer	1.6	4.1	1.0
Pt	69.3	4.9	0.3
SiO_2	103.3	0.7	0.6

The XRR measurements conducted on the bare Pt substrate prior to Co deposition evidenced a surface roughness of $1.2 \pm 0.1nm$ (not shown), a quite high value for heavy metals conventionally deposited by magnetron sputtering.[118] The latter results, jointly with the relatively high roughness of the modeled interlayer ($1.0 \pm 0.1nm$), suggest the presence of a partial oxidation of the Pt surface, likely organized in PtO_x islands. The presence of such partial surface oxidation is of course unwanted, and cannot be removed with the mild 180 °C thermal annealing to which the samples are subjected during the ALD of Co. In contrast to the ALD of Co on Pt, the XRR of Co/Sb_2Te_3 is fully interpreted without inclusion of any interlayer. Although an intermixed region between Co and Sb_2Te_3 could be expected,[37] on the basis of XRR results, we find it negligible when compared to the Fe/Sb_2Te_3 system and well beyond the XRR detection limit.[37, 102] In the inset of Fig.3.12 the SEM cross section of the thickest samples (1000 ALD cycles) is reported, by which we evaluated their structural integrity and thickness. In order to get a further insight about the morphology of the materials, AFM was performed both on the surface of the bare Sb_2Te_3 film and on the final Co(8.1 nm)/Sb_2Te_3 stack (Fig.3.13). From the AFM analysis on a $2 \times 2\mu m^2$ area, the granular nature of the Sb_2Te_3 film and its structural continuity were confirmed. Moreover the root-mean-square (RMS) roughness turned out to be 2.2 ± 0.1nm, in very good accordance with the value extracted by the XRR model (Table 3.7). The image in Fig.3.13(b) confirms the uniformity of the Co layer in the Co(8.1 nm)/Sb_2Te_3 heterostructure and the RMS was found to be 2.8 ± 0.1nm, being quite lower than the value extracted by XRR. The reason behind the discrepancy between the roughness values extracted by the AFM and XRR is that XRR is sensitive to both the morphological roughness and the density grading between two layers, thus typically giving higher roughness than AFM, also suggesting the presence of a subnanometric oxidized layer at the Co surface.

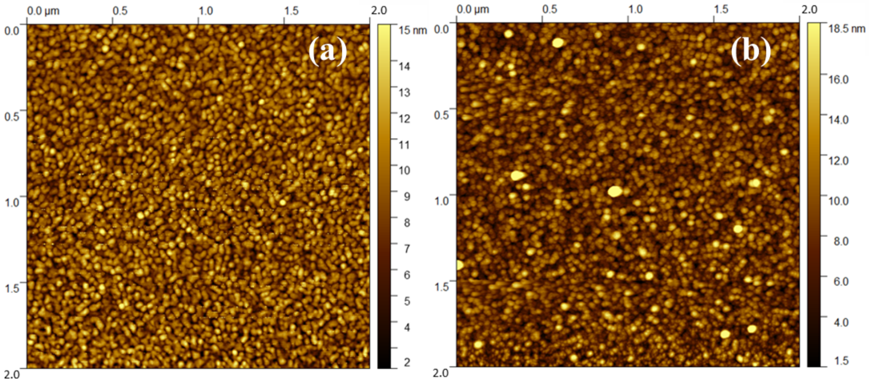

Figure 3.13: AFM images of $2 \times 2\mu m^2$ area of (a) the Sb_2Te_3 surface and (b) the final Co(8.1nm)/Sb_2Te_3 structure. The extracted values for the RMS are 2.2 ± 0.1nm and 2.8 ± 0.1nm respectively. Figure taken from Ref.[44].

The thickness of the Co layer as a function of the number of cycles, as measured by XRR and SEM, is plotted in Fig.3.14. The growth rate of Co on the Sb_2Te_3 and Pt substrates was extracted by the linear interpolation of the data, and turned out to be 0.5 Å/$cycle$ for the Co/Sb_2Te_3 sample and 0.35 Å/$cycle$ for Co grown on Pt. These values are lower than those reported for similar process at 200 °C on Pt. This difference can be attributed to both the different ALD reactor used (Picosun R-75 BE) and the lower temperature of our process. [62, 115] The Y-intercept is -1.95 nm for the growth on the Sb_2Te_3 and -2.1 nm for the growth on Pt, which correspond to a delay in the Co deposition of 40 cycles in the first case and of 60 cycles in the second one. We attribute this delay to a partial surface oxidation of the underneath Sb_2Te_3 and Pt surfaces. Indeed, Kerrigan et al. showed that the Co growth is typically prevented on top of oxides [115]. Interestingly, the different Co growth rates observed on top of Sb_2Te_3 and Pt clearly show that the Co deposition is affected by the chemical-structural nature of the substrate.

As deeply discussed in Section 3.1.2.1, the Sb_2Te_3 crystalline quality is enhanced upon thermal treatments up to 200 °C and a consequent reduction of the surface oxidation is also observed. This is much likely the cause of the higher Co growth rate observed on top of Sb_2Te_3 when compared to Pt.

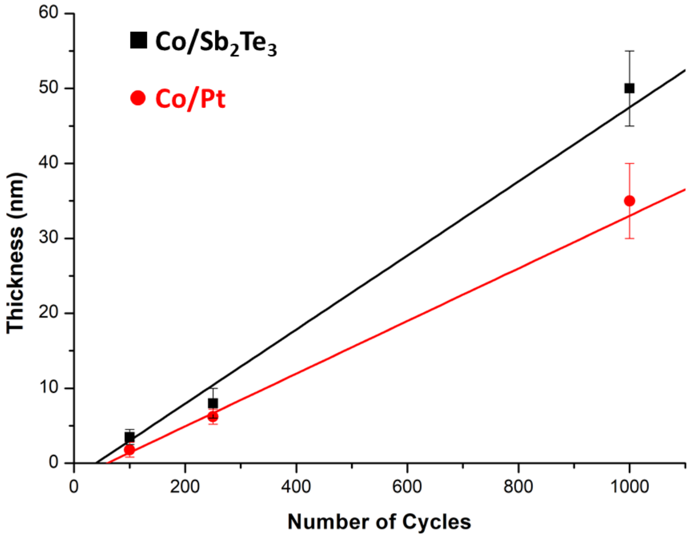

Figure 3.14: Thickness of the Co thin films deposited at 180 °C as a function of the number of ALD cycles for the Sb_2Te_3 (black) and Pt (red) substrates. The extracted linear fits are: $y = 0.049x - 1.946$(Co/Sb_2Te_3) and $y = 0.035x - 2.109$(Co/Pt). Figure taken from Ref.[44].

In order to obtain further information on the influence of the substrate on the structural properties of the Co thin films, we performed GIXRD measurements on both the stacks and the collected diffraction pattern are shown in Fig.3.15 (a). As discussed before, the Sb_2Te_3 thin film is granular and highly texturized, with the OOP orientation of its crystalline grains directed along the $[00\ell]$ orientation.[102] In Fig.3.15 (a) the signal-to-noise ratio for the Sb_2Te_3 peaks is progressively reduced due to the rising of the background produced by the Co fluorescence, which increases linearly with the Co thickness. As a result of the simultaneous increase of the Co thickness and the lowering of the Sb_2Te_3 signal, the Co reflections are more evident in the sample with the thickest Co layer (Fig.3.15(a) top pattern), due to the higher volume of Co involved in the diffraction process. During the Co deposition, as a consequence of the thermal budget provided to the samples, the Sb_2Te_3 crystallinity is progressively enhanced, favoring a further orientation of the film along the [00ℓ] direction. Moreover, we know that this annealing process promotes the oxygen dissociation from the Sb_2Te_3 surface [102], preparing the latter for the Co growth. On the contrary, the oxidation of the Pt substrate should be unaffected by the extremely mild temperature exposure. [119] In the Co/Sb_2Te_3 samples, the presence of the peaks positioned at $2\theta \sim 45°$ and $2\theta \sim 75°$ correspond respectively to the reflections from the (002) and (110) planes belonging to the Co hexagonal-closed-packed (hcp) crystalline structure.

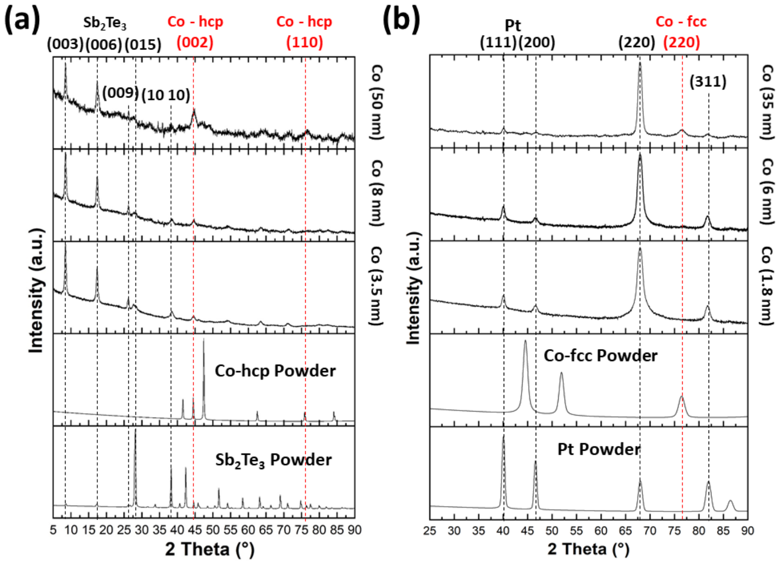

Figure 3.15: GIXRD pattern of the Co/Sb_2Te_3 and the Co/Pt set of samples. The Co-hcp and Co-fcc crystalline phases were identified respectively on the Sb_2Te_3 and Pt substrates. Figure taken from Ref.[44].

In fig.3.15 (b), the presence of the cubic Pt phase is confirmed by the correspondence between the collected Pt reflection and the Pt powder diffraction pattern. Also in this case, the consideration about the Co fluorescence are valid, thus a lowering of the Pt peaks intensity was observed with the increase of the Co thickness. Differently from what happens on top of the Sb_2Te_3 substrate, on top of Pt the Co reflection with the highest intensity is located at $2\theta \sim 76°$. By calculating the angle between the different families of planes within the hcp or the fcc structures of Co, we demonstrated that the presence of the Co peak at $2\theta \sim 76°$ can be attributed to the (220) reflection of [111] OOP oriented fcc Co (Supplementary Information of Ref.[44]).In order to get more insight about the orientation of the crystalline grains of our heterostructures, we performed

BBXRD measurements on the Co(50 nm)/Sb_2Te_3 and the Co(35 nm)/Pt samples which are shown in Fig. 3.16. In this BBXRD patterns, the rocking angle ω was varied in the 2°–25° range and the diffracted photons were collected using the same position-sensitive gas detector adopted for GIXRD. In this configuration we detected both the symmetric ($\omega = \theta$) and the non-symmetric reflections from the crystalline planes, determining the OOP orientation and the mosaicity of the measured thin films. We racall here that the mosaicity is a measure of the grains orientation broadening, which provides information on the structural isotropy in a thin film. In Fig.3.16(a) the BBXRD spectrum for the Co(50 nm)/Sb_2Te_3 sample is reported. Here, at $2\theta \sim 8.5°$, $2\theta \sim 17°$ and $2\theta \sim 26°$, we observe three lines corresponding to the Sb_2Te_3 (003), (006) and (009) reflections.

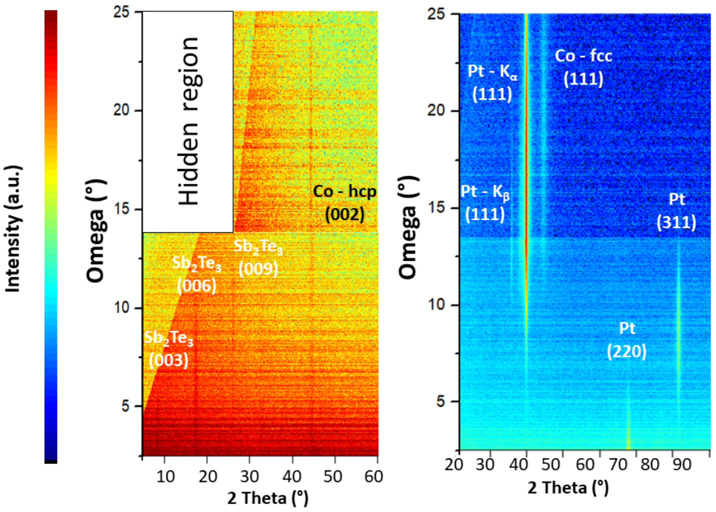

Figure 3.16: XRD measurements in Bragg-Brentano geometry of the thickest samples (1,000 ALD cycles): Co/Sb_2Te_3 on the left and Co/Pt on the right. The hidden region in the BB-XRD measurement on the left is present due to a geometrical limitation of the adopted instrumental set up. Figure taken from Ref.[44].

The presence of lines and not just spots is an indication of the strong mosaicity characterizing our Sb_2Te_3 granular thin film. Hence, we can consider such grains out-of-plane oriented along the $[00\ell]$ direction, with a broadened orientation on a relatively wide solid angle. Beside the Sb_2Te_3 reflections, at $2\theta \sim 26°$ is present a clear line corresponding to the Co-hcp (002) reflection. The presence of such line proves the broad distribution of the Co grains orientation. Moreover, it demonstrates that “grain-by-grain” the Co layer replicates the same orientation and mosaicity of the underlying Sb_2Te_3, with OOP lattice parameter $c = 4.05 \pm 0.01$Å. Due to the lack, in GIXRD, of significant diffracted intensity from asymmetric reflections of OOP (002) oriented hcp Co, the IP lattice parameter cannot be determined. From trivial calculations, if we consider $a_{Co-hex} = 2.51$Å and $a_{Sb_2Te_3} = 4.26$Å, it is however interesting to notice that $a_{Sb_2Te_3}/\sqrt{3} = 2.46$Å is very close to a_{Co-hex}, suggesting that the diagonal of the Co lattice is commensurate with $a_{Sb_2Te_3}$, therefore favoring the epitaxial grain-to-grain growth with Co(001)//Sb_2Te_3(001). At $2\theta \sim 40°$ the diffraction corresponding to the (111) planes of the fcc Pt is strongly evident. Beside the Pt (111) reflection, the peak at $2\theta \sim 45°$is broadened similarly to the latter. Taking into account the GIXRD analyses, this peak can be attributed to the Co fcc (111) reflection. Epitaxial growth of fcc Co on Pt by physical methods has been already reported.[120, 121] Comparing the Co thin films studied in this thesis with those reported in literature, we can confirm their high quality in terms of crystallinity, conformality and interface sharpness. From our analyses of the (111) and (220) peak positions we estimated the lattice parameter to be $a = 3.51 \pm 0.01$Å, in agreement with the one reported in the databases for cubic Co [23], and suggesting that, for the analyzed thickness, Co can fully relax OOP. Thus, in the Co/Pt heterostructures the Co grains mosaicity is lower when compared to the Co/ Sb_2Te_3 case, and the Co is organized in the fcc phase. The comparison between the Co/Pt and Co/Sb_2Te_3 X-ray data (Figs. 3.15 and 3.16) confirms the key-role played by the substrate to determine the structural properties of the Co thin films grown by ALD. Importantly, apart from its advantageous and well-known conformality,the developed ALD process demonstrates the possibility to conduct a local epitaxy that tunes the Co structure through the substrate selection.

Complementary information about the layers and the interface of the Co/Sb_2Te_3 structure and morphology were obtained employing cross sectional high resolution transmission electron microscopy (HRTEM) and energy dispersive X-ray spectroscopy (EDS) on a cross sectional lamella of the Co(8.1 nm)/Sb_2Te_3 sample, as prepared with the focused ion beam (FIB) method. HRTEM analyses (Fig.3.17), clearly show how the Co layer adheres with a very high conformality to the underneath granular Sb_2Te_3 surface. On the right side of Fig.3.17, fast Fourier transform (FFT) analyses are reported for the highlighted region of the TEM image. By FFT the hexagonal crystalline structure of the Sb_2Te_3 and the Co layers were investigated, elegantly confirming the XRD analyses (Figs. 3.15 and 3.16). The Pt layer was deposited to protect the sample during the FIB lamella preparation. The FFT of this Pt layer is also shown and its fcc crystal structure identified.

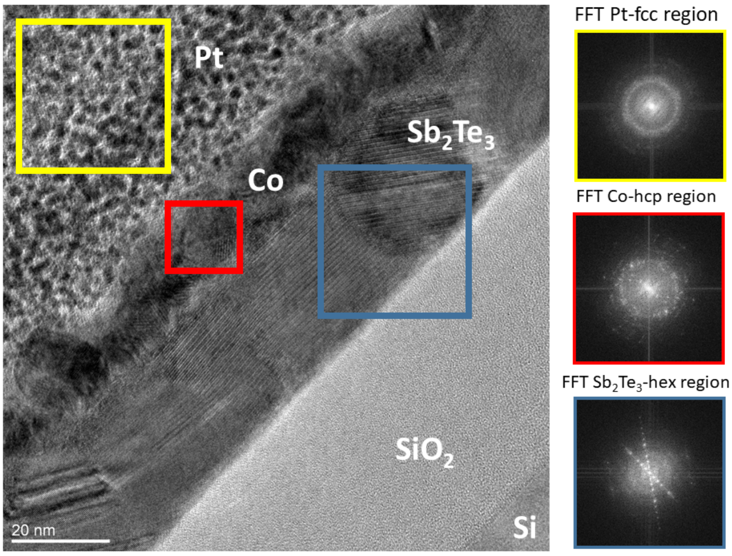

Figure 3.17: HRTEM cross section of the Co(8.1nm)/Sb_2Te_3) heterostructure.On the right the FFT analysis of the highlighted region in the TEM image. Figure taken from Ref.[44].

Figure 3.18 shows the elemental depth profile extracted from the red box in the TEM image inset. The spatial distribution of the Co, Sb and Te elemental signals shows that their overlapping extends over a distance comparable with the surface roughness of the Sb_2Te_3 granular layer. Thus, the EDS results confirm the absence of an intermixed layer at the Co/Sb_2Te_3 interface, in agreement with XRR (Table 3.7). The O evolution (green line) along the stack indicates a partial oxidation of the Co layer, which is attributed both to the lack of a capping layer on top of Co and to the oxygen exposure of the whole heterostructures during the TEM lamella preparation.

The development of different IP crystallographic ordering depending on the underlying substrate has been already reported for the ALD deposited oxides. [122, 123] Due to the structural continuity and the absence of developing interfacial oxides and/or under-layers between the substrate and the grown metal, the promotion of the observed IP ordering follows the rules of commensurability of interatomic distances as for physical deposition. Actually, for Co ultra-thin films deposited by ultrahigh vacuum RF magnetron sputter-

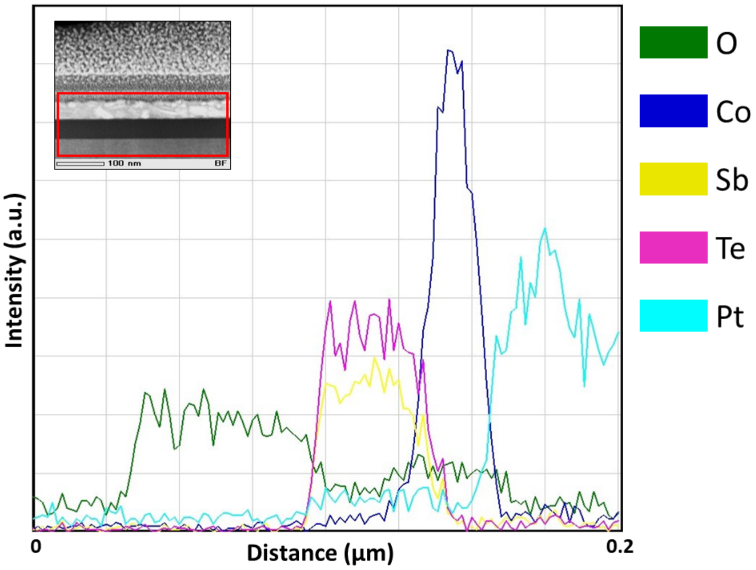

Figure 3.18: Elemental profile of the Co(8.1nm)/Sb_2Te_3 samples. the signalsare integrated along the red rectangular region in the inset (the distance is measured from the bottom of the red box). Figure taken from Ref.[44].

ing, when an appropriate template is used, deposition in the hexagonal or in the cubic frameworks should take place at the same temperature.[124] The lower growth rate measured for the growth on Pt when compared to that on Sb_2Te_3 can be attributed to a "cube-on–cube" growth and therefore related to the more ordered arrangement of atoms of the fcc than of the hcp unit cell, corresponding to the larger unit volume of the fcc cell. The adatoms mobility is promoted by the thermal budget, which is equal in both the Sb_2Te_3 and Pt cases. Therefore, the more ordered fcc structure when compared to the hcp, could require a longer time in order to arrange the Co atoms, and this turns out in a slower growth rate.

To conclude, the possibility to synthesize by ALD high quality metallic Co ultra-thin films on top of the granular topological insulator Sb_2Te_3 has been demonstrated. We presented evidences of a local epitaxy driving the as-grown Co structure depending on the underneath substrate, with metallic Pt promoting fcc-Co, while Sb_2Te_3 promoting the hcp-Co. In particular, in Ref.[44] different IP orientations following the rules of atomic distances commensurabilities has been observed, similarly to what happens for physical deposition methods. The achieved local epitaxy, jointly with the excellent conformality and the extreme thickness-control of the ALD-grown Co layers, opens perspectives for the cost effective inclusion on large areas of the presented Co/(Sb_2Te_3, Pt) systems in emerging spintronic devices.

3.2 Integration of Co thin films with epitaxial-Sb_2Te_3

The topological properties of TIs are closely related to their crystalline quality. Even if topological properties have been reported also in granular materials, [125] highly ordered TIs are expected to display stronger topologically-protected states. [35, 36, 61] Indeed, such highly ordered materials are able to host more robust linearly dispersed topological surface states (TSS) as compared to disordered materials, which is crucial for an optimized employment of TIs for spintronic applications.

In Section 3.1, I summarized the efforts spent towards the integration of the granular Sb_2Te_3 TI with Fe and Co thin films, demonstrating the possibility to produce highly sharp and stable Fe,Co/Sb_2Te_3 interfaces. While carrying out those studies, I was also involved in the optimization of the structural/morphological properties of Sb_2Te_3 thin films, a research activity that is active at CNR-IMM of Agrate Brianza. Indeed, the content of Section 3.2.1 is largely based on the results reported in Ref.[42], where my contribution was a thorough XRD and XRR analysis on the optimized MOCVD-grown Sb_2Te_3 thin films, which gave us the possibility to investigate their structural properties identifying the epitaxial fashion of such a film. Subsequently, in Section 3.2.2 I will present the integration of Co thin films with epitaxial Sb_2Te_3, together with the implementation of a Au capping layer in order to protect Co from oxidation in Au/Co/Sb_2Te_3 heterostructures. Here, I also reported the VSM measurements on Au/Co/Sb_2Te_3 systems conducted at the Politecnico di Milano by Prof. Matteo Cantoni and Dr. Christian Rinaldi, in order to investigate on the quality of our deposited FM thin films also by the magnetic point of view.

3.2.1 Sb_2Te_3 thin films: from polycrystals to epitaxy

The granular Sb_2Te_3 thin films grown on top of SiO_2 substrates are demonstrated to be highly OOP oriented along the [00ℓ] direction of their rhombohedral crystalline cell. Moreover, their texturization can be enhanced if their are subjected to proper thermal treatments (Section 3.1.2.1). However, the amorphous structure of SiO_2 thin films is inherently unsuitable to promote an epitaxial order when used as substrates. For that, a crystalline substrate is necessary, which should be also characterized by a moderate lattice mismatch as compared the Sb_2Te_3 film. Commonly employed substrates in TIs growth, such as Si(100), Si(111), and Al_2O_3(0001), show a significant lattice mismatch with Sb_2Te_3 (and TIs in general) that therefore grows as poorly oriented polycrystalline layers in the presence of rotational domains, [126–128] with only a few exceptions.[129, 130] Recently, to overcome this issue, way less common materials, such as BaF_2(111)[131] and, for instance, a ZnTe or GaN buffer layer on Al_2O_3(0001), have been identified to lattice match with telluride-TIs and effectively adopted as substrates to enhance the quality of the films.[131]

Most significantly, the large area deposition of high-quality Sb_2Te_3 epitaxial layers on Si substrates with thickness control below 100 nm would be much attractive for integration in CMOS compatible devices. In MOCVD processes, alike other chemical methods such as ALD, the selection of precursors plays a relevant role in governing the growth and morphology of the films. So far, the most promising results in Sb_2Te_3 growth were achieved employing trialkylstibines (such as $SbMe_3$, Sb^iPr_3) and diallyltellanes ($TeEt_2$, Te^iPr_2) as precursors; however, temperatures greater than or equal to 400 °C were required, along with a dihydrogen partial pressure, to sustain the precursors' pyrolysis. In the following,we report a RT MOCVD process to obtain epitaxial Sb_2Te_3 thin (30 nm) films in direct contact with Si(111) substrates and show the effect of pre-growth (substrates annealing) and post-growth (film processing) treatments on the film morphology, surface roughness, crystallinity, and crystallographic orientation (Section 2.1.1).[42] For the sake of clarity, in this section we will use the following notation to indicate the different thermally treated samples: as deposited $Sb_2Te_3/Si(111)$ (**1**), pre-annealed $Sb_2Te_3/Si(111)$ (**2**) and post-annealed $Sb_2Te_3/Si(111)$ (**3**).

In Fig. (3.19) the SEM and AFM analyses on samples **1**, **2** and **3** is reported. Apart from the marked granularity and non uniform crystalline grains, sample **1** is structurally continuous and very similar to the granular Sb_2Te_3/SiO_2 discussed in Section3.1. The AFM on **1** substantiated a non-directional growth and RMS roughness around 4-4.5 nm (these values found reproducible in several growths). In order to improve the film quality, an in situ Si(111) substrate thermal annealing was tested(500 °C and 20 mbar under N_2

atmosphere for 1 h). Fig. 3.19 shows the tilted cross-section SEM image of Sb_2Te_3 films deposited on the treated substrate (**2**), which clearly evidence the enhanced crystallinity and significantly improved morphology of the film. Moreover, granularity was largely diminished to the extent that Sb_2Te_3 appeared as a continuous film no longer composed of juxtaposed grains of various sizes and, consequently, the surface roughness was lowered (RMS roughness of 1.5–1.8 nm). AFM data highlighted interesting features in the fine structure of the films (Fig. 3.19). The sample **1** exhibited a non-uniform granularity consisting of a bimodal grains size distribution centered at ca. 18 and 33 nm. On the other hand, the film in sample **2** can be described by a narrower distribution of smaller grains – mostly within the 11–14 nm range – specifically accountable for the lower surface roughness. Aiming at further structural improvement, an in situ post-growth treatment was performed; the sample **2** was subjected to a thermal annealing at 300 °C under N_2 atmosphere for 15 min, at a relatively high pressure (900 mbar) to prevent or minimize desorption phenomena (Fig. 3.19, **3**). This post-growth processing step neither did alter the film thickness nor was detrimental to its uniformity. It triggered instead a reorganization of the grains throughout the film.

As qualitatively demonstrated from SEM and AFM images, the most intriguing characteristic is relative to the film orientation, which became uniform and poorly spread. Moreover, this is accompanied by a further lowering of the film roughness (RMS roughness of 0.9–1.3 nm), an aspect which is of major importance in the view of integrating additional layers on top of the optimized Sb_2Te_3 (see below in Section 3.2.2). An AFM profile extracted from sample **3** (Fig. 3.19) evidences steps of 1 nm (consistent with an antimony telluride quintuple layer), supporting an improved ordering with respect to the parent Sb_2Te_3 materials **1** and **2**. The MOCVD average growth rate of $0.44 \pm 0.01 nm\ min^{-1}$, extrapolated from films prepared with different deposition times, resulted appreciably lower than literature values that fall within the 8–50 nm min^{-1} range.[126, 129] However, dissimilar experimental conditions, including the choice of the precursors (their chemical reactivity), the higher deposition temperature (up to 450 °C), and the use of dihydrogen rather than an inert gas can significantly impact the growth rate and are therefore accountable for the observed low values.

The morphology and structural properties of the films were studied in detail by performing TEM analyses.[42] Typical cross-sectional high-resolution views of the three different

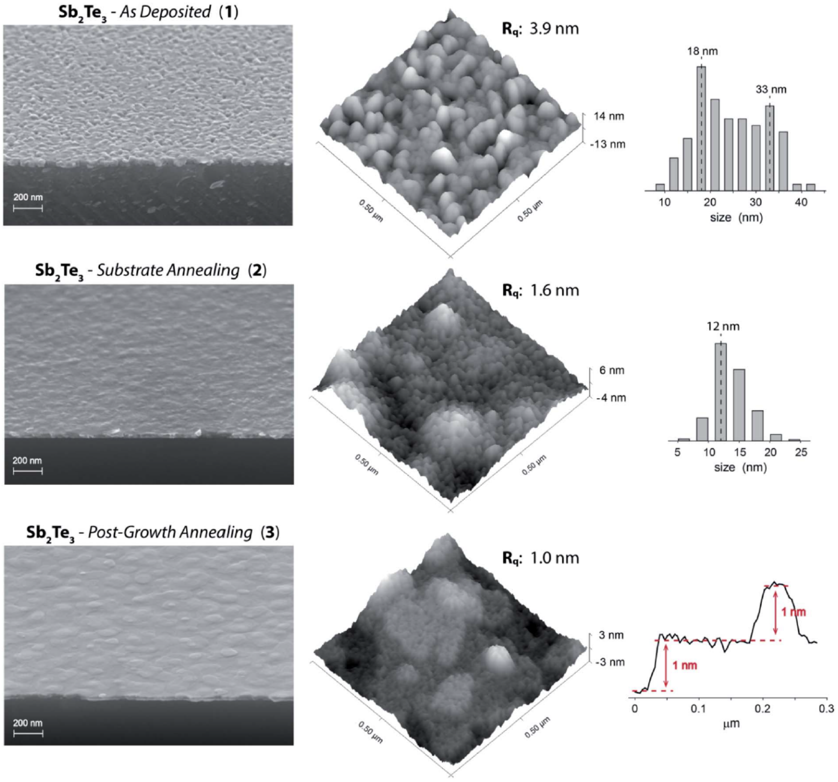

Figure 3.19: (Left) Tilted cross-section SEM images, (center) AFM images (Rq values are specific to the shown AFM images), (Right) grains size distribution histograms (as determined by AFM) of Sb_2Te_3 – As Deposited (**1**) and Sb_2Te_3 – Substrate Annealing (**2**), and a selected AFM surface profile of Sb_2Te_3 – Post-Growth Annealing (**3**). Figure taken from Ref.[42].

types of samples are reported in Fig. 3.20, including the corresponding Fast Fourier Transform (FFT) (insets). In general, crystalline planes and van der Waals stacks were observed in all samples, although each one showed a different degree of ordering and orientations. Amongst the three samples, **1** appeared to be the most granular and defective in nature.

Its FFT also highlights the essentially random orientation of its grains, even though sometimes the c-axis was found to be almost perpendicular to the substrate. Consistently with the SEM and AFM data, the structure of **2** revealed a much lower granularity and a more ordered growth. However, different crystallographic orientations were detected throughout the sample. Lastly, the sample **3**, in agreement with SEM and AFM results, appeared to be composed of larger building units. The c-axis of the Sb_2Te_3 crystalline

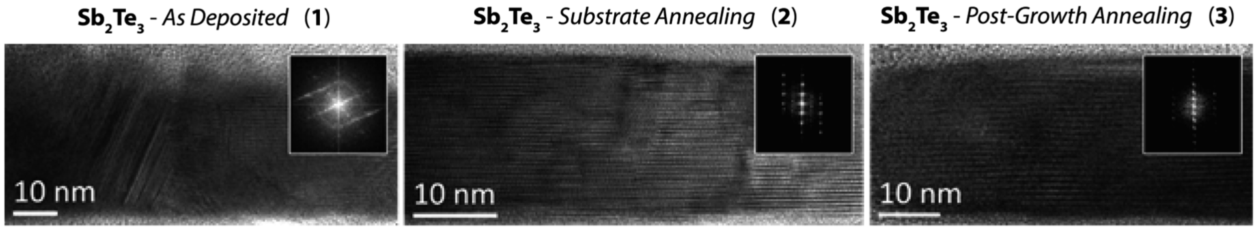

Figure 3.20: Cross sectional high resolution TEM images of the Sb_2Te_3 films: Sb_2Te_3 – As Deposited (**1**), Sb_2Te_3 – Substrate Annealing (**2**), and Sb_2Te_3 – Post-Growth Annealing (**3**). Insets: fast Fourier transform analyses. Figure taken from Ref.[42].

cell was almost always found to be perpendicular to the silicon substrate, while grains with very low misalignment were rarely observed. The van der Waals gaps of the Sb_2Te_3 quintuple layer structure are clearly visible and parallel to the substrate. The (003) periodicity along the c-axis, measured over many pictures, was 1 nm, consistently with the one calculated for the Sb_2Te_3 rhombohedral structure.

Regardless of the morphological and structural differences between the three films, their thickness, probed via XRR (Fig.3.21), remained almost unchanged. In fact, films **2** and **3** showed thicknesses (32.5 and 32.0 nm, respectively) only slightly reduced respect to **1**, fact that is principally explained by their higher crystallinity and enhanced packing.

Table 3.8: Thickness (nm), Electron density ($e^-/\text{Å}_3$), and Roughness (nm) of Sb_2Te_3 - As Deposited (**1**), Sb_2Te_3 - Substrate Annealing (**2**), and of Sb_2Te_3 - Post-Growth Annealing (**3**) extracted from XRR measurements in Fig. 3.21.

	Thickness (nm)	**Electronic density (e/A^3)**	**Roughness (nm)**
Sb_2Te_3 - As Deposited	33.7	1.75	3.1
Sb_2Te_3 - Substrate Annealing	32.5	1.68	2.0
Sb_2Te_3 - Post-Growth Annealing	32.0	1.80	1.5

Also, their composition, as determined from the ratio of the Sb and Te lines detected by TXRF, was found consistent with the Sb_2Te_3 stoichiometry(not shown, please see Ref. [42]). XRD studies were undertaken to probe the Sb_2Te_3 films crystallinity and evaluate the relevance of the substrate annealing and post-growth processing on their structural properties. The GIXRD pattern of **1** (Fig. 3.22a, black) exhibited intense reflections at 2θ= 8.46°, 17.3°, 26.0°, 28.26°, and ca. 38.4° corresponding to the 003, 006,

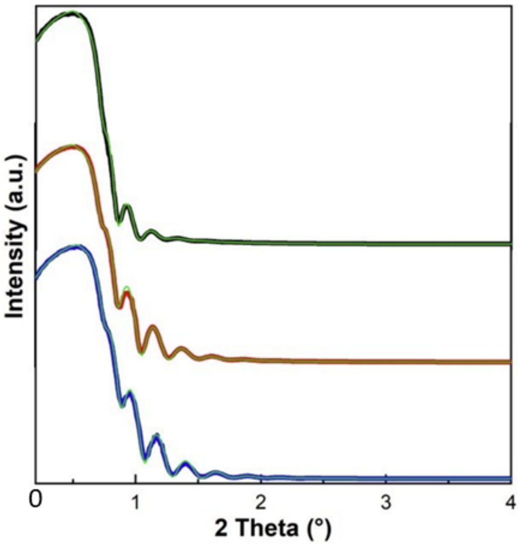

Figure 3.21: XRR measurements of Sb_2Te_3 - As Deposited (**1**) (black, top), Sb_2Te_3 - Substrate Annealing (**2**) (red, middle), and of Sb_2Te_3 - Post-Growth Annealing (**3**) (blue, bottom).Figure taken from Ref.[42].

009, 015, and 1 0 10 reflections, attributed to the rhombohedral crystalline structure in the R-3m space group. The relatively small linewidths of the (00ℓ) peaks indicated high crystallinity while the (015) peak – the peak with the highest intensity in the powder diffractogram – indicated the polycrystalline nature of the film, and its broadening, possibly, a structural amorphous component.

Interestingly, the 015 reflection was no longer observed in **2** (Fig. 3.22a, red), whereas the 003 reflection was drastically enhanced, indicative of grains predominantly oriented along the [00ℓ] direction and, consequently, of a more crystalline structure. Moreover, the GIXRD of the **3** revealed an overall reduction of the peaks intensity (Fig. 3.22a, blue) suggesting substantial changes in the structure, compatible with a crystallinity improvement. To assess the Sb_2Te_3 crystalline nature, XRD measurements were set up specifically to probe out-of-plane and in-plane orientations.

The XRD patterns collected in the Bragg–Brentano geometry (Fig. 3.23a) revealed the scattering of the reflections' intensity across ω (plot's y-axis), feature informative of the broadening in the (00ℓ) out-of-plane orientation. While the FWHM of the ω scan, (see plots in Fig. 3.23a) was substantial in **1** (up to 9°), it appeared much reduced in **2** (2.6°)

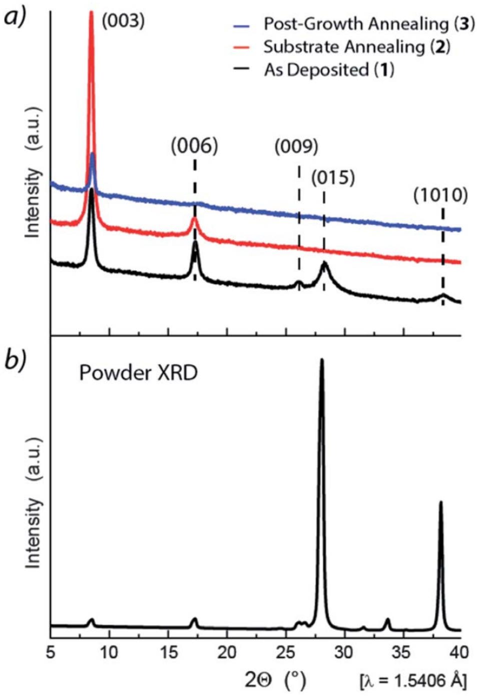

Figure 3.22: (a) Grazing incidence X-ray diffraction pattern of (bottom, black) Sb_2Te_3 – As Deposited, (red, middle) Sb_2Te_3 – Substrate Annealing, and (blue, top) Sb_2Te_3 – Post-Growth Annealing; (b) powder XRD pattern reference for Sb_2Te_3 measured at RT and atmospheric pressure. Lattice parameters: a = 4.264 Å and c = 30.458 Å. Figure taken from the supporting information of Ref.[42].

and strongly contained in **3** that showed an FWHM value of 0.46°, indicating a mosaicity typical of epitaxial films and suggestive of single crystal-like materials. These data, along with the absence of the 015 reflection (both in **2** and **3**, consistently with the GIXRD – Fig. 3.22) indicated strongly (00ℓ) out-of-plane oriented grains in **3**. Moreover, the in-plane orientation, probed through a ϕ angle scan here optimized on the 015 reflection (2θ = 28.26°), appeared positively affected by Substrate Annealing and Post- Growth Annealing, too (Fig.3.23b).

In fact, while **1** showed almost no in-plane ordering, 60°-spaced peaks distinctive of the 3-fold symmetry of the Sb_2Te_3 rhombohedral cell (and related to the 015 reflection) emerged in the 2θ–ϕ plot of **2**, as result of a preferential in-plane orientation (Fig. 3.23b). However, the faint line connecting the (015) peaks revealed residual disorder, indicative of a minor fraction of randomly oriented grains. Differently, the intense, precisely positioned, and narrow peaks of the 015 reflections observed in **3** indicates an almost

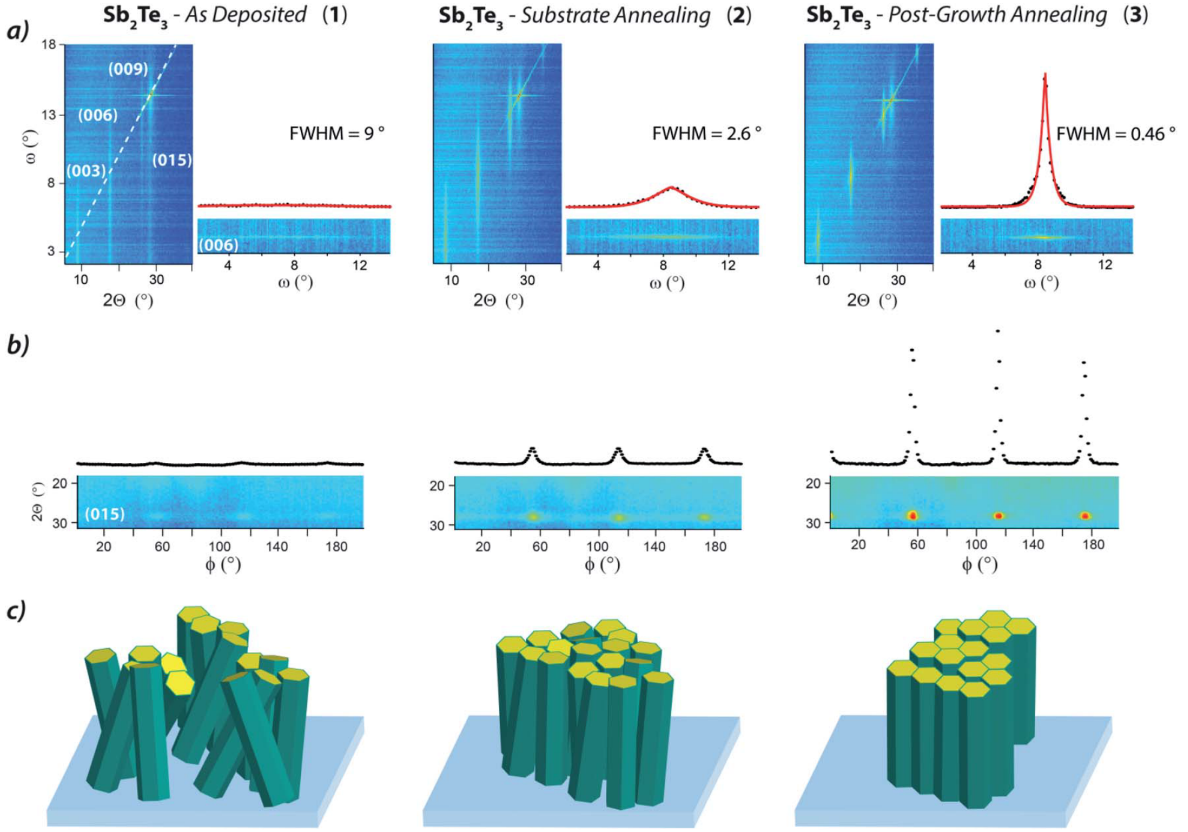

Figure 3.23: a) XRD pattern collected in Bragg–Brentano geometry, including the profile of the (006) peak and the mosaicity values, and (b) ϕ angle scan of Sb_2Te_3 – As Deposited (1), Sb_2Te_3 – Substrate Annealing (2), and Sb_2Te_3 – Post-Growth Annealing (3). The dashed line in (a) evidences the Bragg–Brentano condition. The most intense signal in (a) is the 111 reflection pertaining to the silicon substrates and it is very close to the (015) peak. (c) Graphical representation of the Sb_2Te_3 crystalline ordering and orientation relative to the Si(111) substrate. Figure taken from Ref.[42].

complete in-plane ordering (Fig.3.23b). Combining the data from the Bragg–Brentano and the ϕ scan, the epitaxial relationship between the Sb_2Te_3 and the substrate is found as $Sb_2Te_3[00\ell] \parallel Si[111]$ and $Sb_2Te_3[015] \parallel Si[011]$. The latter epitaxial relationship was deduced by a careful positioning of the sample, in the way that the $\phi = 0$ position corresponds to the Si[011] direction parallel to the X-ray beam. The set of structural information attained from the microscopies and diffraction measurements can be rationalized as sketched in Fig. 3.23c. This visual representation highlights the structural and morphological transition from a highly granular and poorly oriented film (**1**) to a smoother and crystallographically out-of-plane ordered one (**2**), and, finally to an epitaxial layer, consisting of crystallites both in-plane and out-of-plane oriented (**3**). The quality improvement observed comparing samples **1** and **2** is the result of the Si(111) substrate annealing. A high temperature substrate treatment likely favors the removal of adventitious physisorbed or chemisorbed water, preventing from a disorderly initial-stage deposition, whereas we tend to exclude surface reconstruction phenomena that are known to take place at higher temperatures.[132] In fact, as the MOCVD process was performed at room temperature, therefore not requiring the precursors' pyrolysis, residual surface water and hydroxyl groups would readily react with the protolyzable organometallic precursors, compromising the integrity of the silicon/Sb_2Te_3 interfacial van der Waals layers and possibly resulting in an uncontrolled deposition and an unordered and highly granular growth. While some structural enhancement (out-of-plane orientation) was obtained upon substrate annealing, the most remarkable improvement was indeed achieved with the post-growth processing. This step is specifically responsible for the in-plane ordering. We speculate that the thermal treatment triggers a rearrangement of the grains into a thermodynamically preferred configuration allowed by the symmetry match between the substrate and the film. The crystallites preferential orientation is possibly induced by the surface-exposed crystalline lattice of Si(111). The working hypothesis for the selection of Si(111) as preferred substrate in the present study relies indeed on its surface lattice symmetry, analogous to the Sb_2Te_3 crystalline cell.

3.2.2 Scaling of evaporated Co thin films and Au capping

In sections 3.1.2 and 3.1.3, we widely discussed the chemical-structural properties of Fe,Co/Sb_2Te_3-granular heterostructures, where the Fe and Co ferromagnetic thin films were deposited by PLD and ALD respectively. Several bottlenecks have been identified. Certainly, in order to exploit the peculiar TIs properties in contact with FMs, there is the interest of controlling the FM thickness to the nanometer-scale. At the same time, to prevent the surface oxidation of the FM is demanding. In the following I present the chemical, structural and magnetic characterization of Au/Co/Sb_2Te_3 heterostructures, where Au/Co have been produced in situ by e-beam evaporation (Section 2.1.3), on top of the optimized Sb_2Te_3.

In the following, we present the data relative to the XRD/XRR and VSM measurements on Au/Co/Sb_2Te_3 heterostructures. These results are a selection of a systematic activity focused on the production and the optimization of evaporated Au/Co bilayers on top of epitaxial Sb_2Te_3 substrates conducted in our laboratory at the CNR-IMM Unit of Agrate Brianza.

Fig.3.24 shows the XRR collected signals for a set of Au(5 nm)/Co(t)/Sb_2Te_3 samples, where the nominal Co thickness t spans in the range of 2-15 nm.

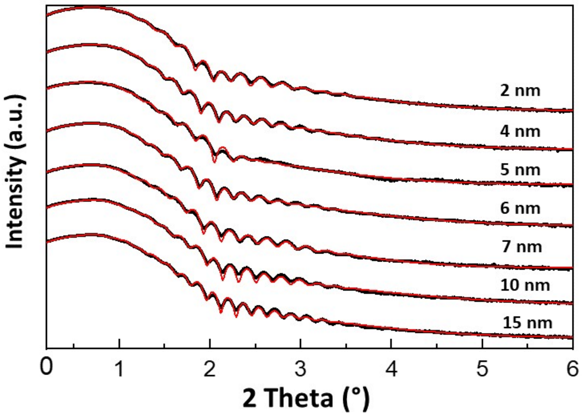

Figure 3.24: XRR collected data for the Au(5 nm)/Co(t)/Sb_2Te_3 heterostructure as a function of the Co thickness t (black lines). Each curve is fitted with a multilayer model and the obtained XRR parameter are summarized in Table 3.9.

Table 3.9: Thickness, Electronic density and Roughness for each layer composing the Au/Co/Sb_2Te_3 samples as a function of the Co thickness extracted from XRR measurements in Fig. 3.24. In the first two rows of the table, we reported the average values for the parameters relatively to the Au and Sb_2Te_3 layers, being them similar in all the samples and not related to their magnetic properties. On the other hand, the detail of the Co parameters for each Co layer thickness is reported.

	Nominal Thickness (nm)	Measured Thickness (nm)	ρ (e^-/Å^3)	Roughness (nm)
Sb_2Te_3	30	31 ± 3	1.6 ± 0.1	1.35 ± 0.3
Au	5	4.5 ± 0.5	4.2 ± 0.1	1.5 ± 0.1
Co	2	1.6	2.15	1.4
	4	3.3	2.15	1.57
	5	4.1	2.15	1.6
	6	4.73	2.15	1.77
	7	6.2	2.15	1.52
	10	9.5	2.15	1.5
	15	14.1	2.15	1.57

The XRR signal oscillations evolve coherently as a function of the Co thickness, confirming the successful thickness control of the deposition technique. In order to extract information about the effective thickness, roughness and electronic density (ρ) of each layer, the XRR spectra are fitted with a multilayer model and the extracted values reported in Table 3.9. Due to the shape of the oscillations of the XRR signals and the presence of different layers in the stack, several models could fit well the collected data. Thus, in order to minimize the convolution between the XRR parameters, the best model for the whole stack was obtained fixing the ρ value for the Co layer ($\rho = 2.15\ e^-/\text{Å}^3$). Such strategy reproduced values for the Au and Sb_2Te_3 layers compatible with those already measured in similar structures and compatible with literature, supporting the validity of the adopted model (Table 3.9). As a complementary structural characterization, we performed GIXRD measurements on the same Au/Co/Sb_2Te_3 structures. In the top panel of Fig. 3.25 the GIXRD spectra for the Au(5 nm)/Co(15 nm)/Sb_2Te_3 sample is reported.

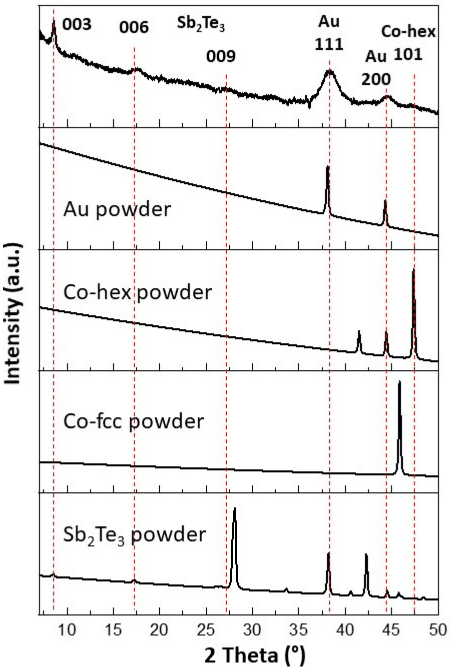

Figure 3.25: GIXRD pattern for the Au(5 nm)/Co(15 nm)/Sb_2Te_3 heterostructure (top panel). The powder diffraction patterns of the materials of interest are reported for a direct comparison with the experimental data. As discussed in the main text, the most visible peaks are associated to the diffraction of the Au crystalline planes, due to the strong fluorescence of Au which hides the peaks belonging to the other crystalline phases.

From the comparison between the collected data and the powder diffraction patterns of Au, Co and Sb_2Te_3 materials, it is clear as the most visible reflections are those associated with the (111) and (200) peaks of the polycrystalline Au layer. Indeed, despite the presence of a 15 nm thick Co layer, it is only visible a very weak and broadened diffraction peak likely attributed to the (101) reflection from the hexagonal crystalline structure of Co. As previously discussed in section 3.25 for the Co, here the Au fluorescence increases the GIXRD signal background, hiding the reflections from the Co and Sb_2Te_3 crystalline structures. It is important to underline that the GIXRD pattern reported in Fig.3.25 is the result of a 4 hours long measurements, which helps to understand the role of a high level of fluorescence in a XRD measurement.

Figure 3.26 shows the hysteresis loops of the same set of samples summarized in Table 3.9, where the the magnetization ($\vec{M}$) as a function of the external magnetic field (H_{ext}) applied IP is recorded by VSM.

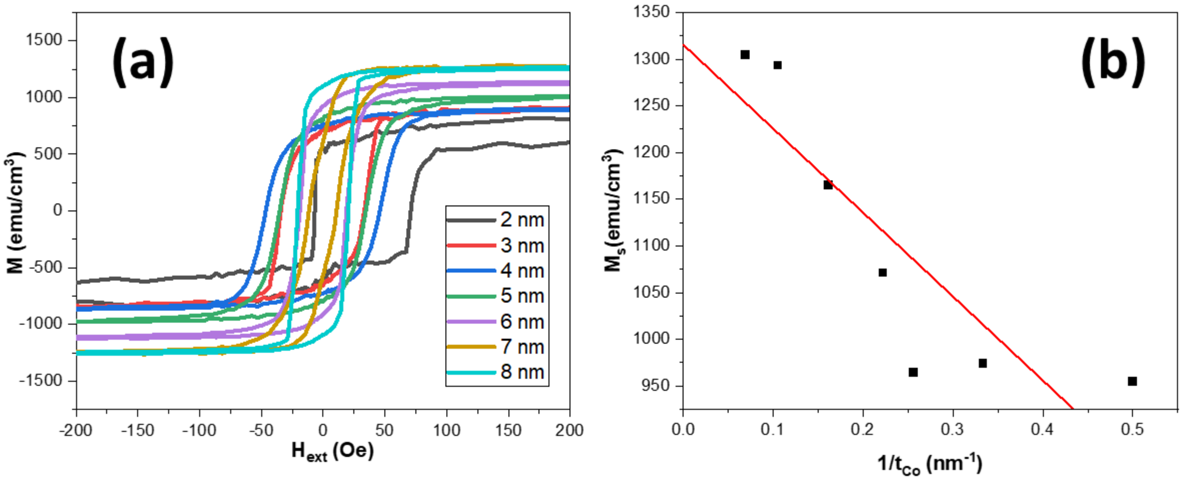

Figure 3.26: (a) In-plane VSM measurements on the Au/Co(t)/Sb_2Te_3 samples. The shape of the recorded magnetic hysteresis loops indicates that the magnetization of all the Co thin films lies IP. (b) Values of the saturation magnetization (M_s) extracted by the curves showed in (a) and plotted as a function of the inverse of the thickness. The value of the intercept with the y-axis $M_s = 1315 \pm 62 emu/cm^3$ compares well with the M_s values for the Co bulk.

The shape of the hysteresis loops indicates that the easy axis of the magnetization lies IP for all the Co thicknesses. Moreover, VSM demonstrates how the value of the saturation magnetization M_s decreases with the scaling down of the Co thickness, as expected.[133, 134] Importantly, even for the thinner Co sample (real thickness 1.6 nm from XRR,

Table 3.9) the M_s value of $\sim 950\ emu/cm^3$) indicates the good magneto-structural quality of the film. VSM clearly confirmed that the employed Au capping preserved the Co magnetic properties by efficiently preventing the unwanted oxidation.

3.3 Broadband - FMR on FM/Sb_2Te_3 heterostructures

In this chapter the main results obtained by measuring the FMR response on a selection of the FM/Sb_2Te_3 heterostructures studied in this thesis are reported. As a first attempt, in Ref.[44], we discussed the magnetic properties of the Co thin films deposited by ALD on both the granular Sb_2Te_3 and Pt substrates (Section 3.1.3). Here, a comparison in terms of magnetic anisotropy and damping constant is provided, demonstrating that the different Co structural propeties obtained (Section 3.1.3), are reflected in different magnetic behaviour. The content of this section is partially based on the results obtained in Ref.[135] and my main contribution was to perform XRD/XRR and BFMR measurements for all the presented samples.
In Section 3.2, a BFMR study on the capped Au/Co/Sb_2Te_3-epitaxial samples as a function of the Co thickness (2-30 nm) is presented, providing information on the spin mixing conductance (g_{eff}) in such samples.
In the last Section 3.4, I present the results on Au/Co/Au/epitaxial-Sb_2Te_3, for which ISHE was also measured as convincing marker of the presence of SCC mechanisms at the interface with the Sb_2Te_3 TI.

3.3.1 BFMR in $Co/granular - Sb_2Te_3$ heterostructures

In Fig. 3.27, the MFM images of the Co/Sb_2Te_3 stacks discussed in Section 3.1.3 are shown. It is evident that the sample with the thicker Co (50 nm) film (Fig. 3.27(a)) shows the strongest magnetic contrast and the largest magnetic domain size (few μm). In Fig. 3.27 (b) the size of the magnetic domains is reduced to hundreds of nm with a consequent lowering of the magnetic contrast. In the case of the thinnest sample the magnetic contrast disappeared, likely due to the almost-full oxidation of the Co (3.5

nm) layer. In the following, we focus our attention on the thinnest Co layers showing magnetic contrast, i.e. the sample shown in Fig. 3.27(b). It is known that the magnetic properties of Co-hcp and Co-fcc are different as due to the different crystal symmetry. [68, 136, 137]

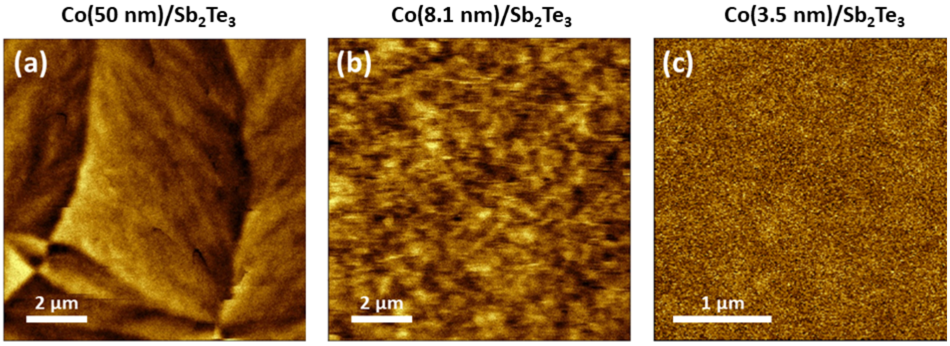

Figure 3.27: MFM measurements for the Co/Sb_2Te_3 samples. (a) The Co (50 nm) layer is characterized by a strong magnetic contrast with very sharp magnetic domains few μm large; (b) the thinner Co (8.1 nm) film evidences a weaker magnetic contrast as compared with (a), with a reduced magnetic domains size of hundreds of nanometers. (c) In this sample no magnetic contrast was evidenced, likely due to the complete oxidation of the Co layer. Figure taken from Ref.[135].

In the following, the investigation on the magnetic anisotropy properties of the developed Co/Sb_2Te_3 and Co/Pt systems is presented. Fig 3.28 shows the $\mathbf{M(H)}$ curves of the Co(8.1 nm)/Sb_2Te_3 and Co (6.3 nm)/Pt samples (Table 3.28), as measured by VSM with the external magnetic field oriented along the film plane. Both samples clearly show an in-plane easy axis. The extracted values for the saturation magnetization (M_s) are $M_s = 922\, emu/cm^3$ for the Co-hcp/Sb_2Te_3 sample and $M_s = 612\, emu/cm^3$ for the Co-fcc/Pt, being compatible with those reported for chemically-grown Co thin films,[138] and slightly lower than for the bulk Co-hcp and Co-fcc. The lower M_s in thin films, when compared to the bulk counterpart, is mainly attributed to the presence of magnetic dead layers at the Co surface, which are certainly present in our samples, due to the absence of any capping layer. From the thorough structural analysis conducted on these systems, it turned out that the polycrystalline Co films exhibit a preferred OOP crystallographic orientation, which is the $[00\ell]$ direction for Co grains on Sb_2Te_3 and the [1 1 1] direction for Co on Pt substrates. [139] Therefore, the hard axis of the magnetization is associated to the $[00\ell]$ direction in the Co/Sb_2Te_3 structure and to the [1 1 1] direction in the Co/Pt samples, respectively. Importantly, as due to the polycrystalline nature of the underneath Sb_2Te_3 and Pt layers, no preferential orientation of the Co grains in the film plane has been observed, preventing us to correlate the easy axis direction with a specific orientation of the Co crystalline structure.

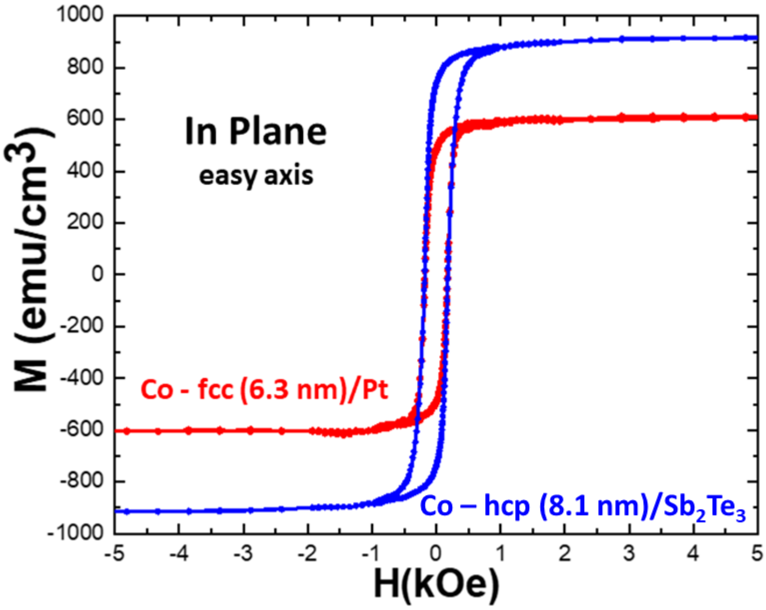

Figure 3.28: In-plane VSM measurements on the Co(8.1 nm)/Sb_2Te_3 (blue line) and the Co(6.3 nm)/Pt (red line) samples. Figure taken from Ref.[135].

A magnetic anisotropy study has been carried out on samples Co (8.1 nm)/Sb_2Te_3 and Co(6.3 nm)/Pt through BFMR. Fig. 3.29 shows the $f_{res}(H_{res})$ data for the Co(8.1 nm)/Sb_2Te_3 (blue squares) and Co(6.3 nm)/Pt (red triangles) heterostructures. As introduced in Section 2.2.3.3, the FMR signal acquired for these samples was the fitted with Eq. 2.28, because a direct measurement, without the use of a lock-in amplifier, was conducted. The BFMR data are fitted with the Kittel equation for the IP configuration (Eq.2.31), in order to extract the values for M_{eff}, which is related to the anisotropy field H_k by Eq.2.32. From the fits in Fig. 3.29, we measure $M_{eff}^{Co-hcp/Sb_2Te_3} = 554\ emu/cm^3$ and $M_{eff}^{Co-fcc/Pt} = 636\ emu/cm^3$. By substituting the M_s values obtained from the VSM measurements in Eq. 2.32, we finally obtain $H_k^{Co-hcp/Sb_2Te_3} =$ 4626 Oe and $H_k^{Co-hcp/Pt} =$ - 312 Oe. From Section 2.2.3.3, we know that the anisotropy field H_k can be written as $H_k = K_{eff}/M_s$, where K_{eff} is known as the effective anisotropy constant and takes into account the crystalline structure of a ferromagnetic material, which is intimately related to its magnetic properties. [68, 133]

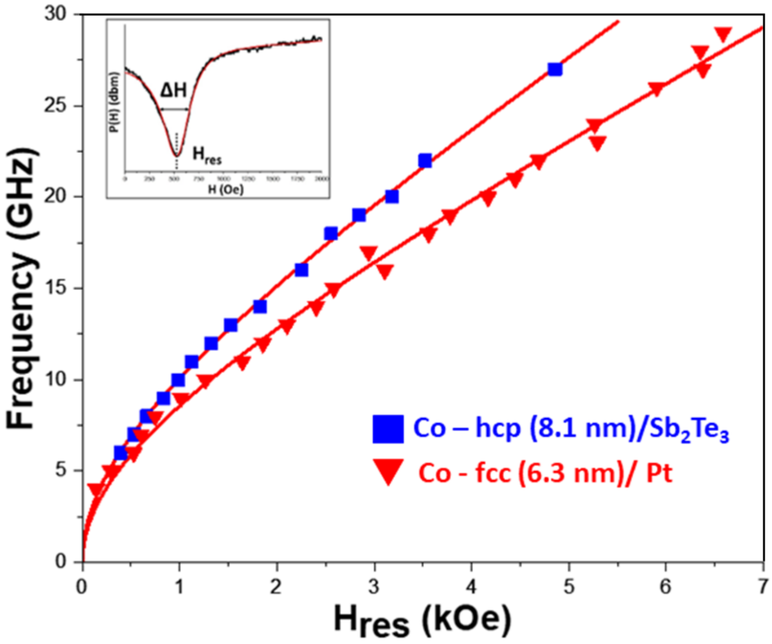

Figure 3.29: f_{res}(Hres) of the Co(8.1 nm)/Sb_2Te_3(blue squares) and Co(6.3 nm)/Pt (red triangles) samples for the IP BFMR configuration. The red solid line represents the fitted data with Eq.2.31. The inset shows a typical FMR absorption curve, in which the resonant magnetic field H_{res} and the linewidth ΔH are indicated. Figure taken from Ref.[135].

From the literature, it is well known that Co-hcp and Co-fcc exhibit large differences in terms of magnetocrystalline anisotropy, due to the different symmetries of their crystalline structures. [140] In general, when the relative orientation of $\vec{M}$ with respect to a specific crystalline plane is known, it is possible to expand K_{eff} as a series of multiple terms which contribute to the calculation of the free energy density for a certain crystal symmetry.[68] Being the preferential orientation of $\vec{M}$ in a polycrystalline Co film not defined, we considered the total effective anisotropy constant K_{eff} as a marker of the different magnetic anisotropy characterizing the hcp and fcc Co polymorphs. We obtain $K_{eff}^{Co-hcp/Sb_2Te_3} = 4.26 \times 10^6\, erg/cm^3$ and $K_{eff}^{Co-hcp/Pt} = 0.43 \times 10^6\, erg/cm^3$. The Co-hcp phase on top of Sb_2Te_3 presents an order of magnitude higher K_{eff} value as compared the cubic Co on top of Pt, as it is expected when comparing hcp and fcc phases. [140] In order to have a further confirmation on the validity of the BFMR collected data, in Fig.3.30 complementary Brillouin Light Scattering (BLS) measurements are shown as conducted on the sample $Co(8.1nm)/Sb_2Te_3$. [96, 97] Here, the good accordance between the two collected datasets is evident, nicely reinforcing our results.

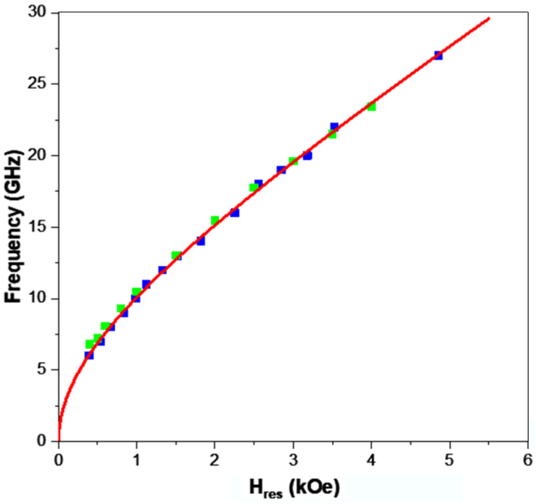

Figure 3.30: Resonance field values for different frequency of incident radiation extracted from BLS measurements of the Co/Sb_2Te_3 heterostructure (green squares). The blue squares refer to the Co(8.1 nm)/Sb_2Te_3 data collected by BFMR, while the red curve represents the trend fitted on BFMR points. BLS technique shows an evident agreement. Figure taken from Ref.[135].

Solely considering the shape anisotropy energy density (defined by $\frac{1}{2}\mu_0 M_s^2$, which is respectively $0.43 \times 10^6\, erg/cm^3$ and $0.19 \times 10^6\, erg/cm^3$ for Co-hcp/Sb_2Te_3 and Co-fcc/Pt, it is not possible to interpret the order of magnitude for the difference between the measured K_{eff} values, which is therefore mainly attributed to the different MC anisotropy. The BFMR results elegantly prove the possibility to tune the magnetism of ALD-Co thin films through an appropriate substrate selection. From the data reported in Fig. 3.29, the g factor values for the Co(8.1 nm)/Sb_2Te_3 and Co(6.3 nm)/Pt heterostructures are obtained, resulting in $g^{Co/Sb_2Te_3} = 2.4 \pm 0.2$ and $g^{Co/Pt} = 2.1 \pm 0.2$. As already mentioned, the IP configuration and the large width of the FMR absorption peaks make the determination of the H_{res} values in the low frequency region of Fig. 3.29 very challenging. This is the main reason for the relatively large error bars in determining the g factor values. On the other hand, by comparing these values with those already reported [141], we underline that $g^{Co/Pt}$ shows a good agreement. The apparent higher g^{Co/Sb_2Te_3} value will be the subject of further investigations, since according to Beaujour et al.[142], the increase of the g factor is attributed to a possible lowering of symmetry at the Co/Sb_2Te_3

interface, which can cause an enhancement of the $\mu_\ell/\mu_s = |g-2|/2$ ratio, where μ_ℓ and μ_s are the orbital and the spin moments, respectively [68]. Motivated by the observed enhancement of the g factor in the Co/Sb_2Te_3 heterostructure, in Fig.3.31 we plotted the frequency-dependent linewidth for the Co (8.1 nm)/Sb_2Te_3 sample. Here, from the fit of the collected data with Eq.2.37, we extracted the values for the damping parameter and for the inhomogeneous term ΔH_0. Interestingly, we found that $\alpha_{Co(8.1nm)/Sb_2Te_3} = 0.095 \pm 0.04$. This is a considerably high value when compared to the intrinsic damping parameter (α_0) for pure Co, independently of its crystalline structure, which is usually reported as being in the range of 0.0052-0.0085 [136].

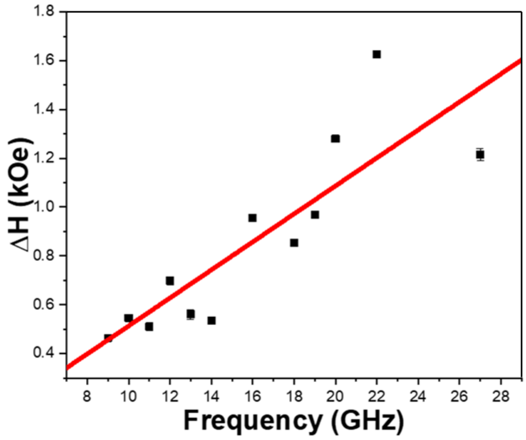

Figure 3.31: Frequency-dependent linewidth (ΔH) for the Co(8.1 nm)/Sb_2Te_3 heterostructure. The red line indicates the fit of the data with Eq.2.37. Figure taken from Ref.[135].

Furthermore, this enhanced value has been found to be almost one order of magnitude higher also as compared to Co/Pt heterostructures, as reported by Verhagen et al. [143]. In several cases, the enhanced damping parameter has been attributed to a possible SP effect from the FM to adjacent non-magnetic (NM) layers. Indeed, Ref.[136] underlines how the intrinsic damping of a FM could be influenced by a spin current flowing across the FM/NM interface, in terms of the spin-mixing conductance ($g^{T,eff}$) of a multilayer heterostructure. This picture is reinforced by considering the TEM and EDS analysis of the Co/Sb_2Te_3 interface (Fig. 3.17)[44], which rules out the presence of secondary phases that could impede the successful SP from Co to the Sb_2Te_3 topological insulator.

The results we obtained on the Co/Sb_2Te_3 and Co/Pt heterostructures demonstrated the possibility to exploit ALD to engineer the magnetic anisotropy of Co thin films by controlling their crystalline structure through the appropriate substrate selection. Interestingly, we also reported an enhanced Gilbert damping parameter (α) for Co/Sb_2Te_3 when compared to those typically reported for Co/Pt. A possible origin for this damping enhancement could be attributed to the establishment of spin currents across the Co/Sb_2Te_3 interface, exploiting the topological surface state of the Sb_2Te_3 TI (Section 2.2.3.5). In order to investigate on the origin of the α value in FM thin films when in contact with Sb_2Te_3, in the next sections we study the BFMR signals in FM/Sb_2Te_3 heterostructures as a function of the FM thickness. In particular, in order to optimize the interface sharpness and stability in terms of elemental interdiffusion, the epitaxial Sb_2Te_3 thin films described in Section 3.2 are employed.

3.3.2 BFMR comparison between polycrystalline Fe and Co on epitaxial Sb_2Te_3

As a next step towards the investigation of SCC effects in optimized (epitaxial) Sb_2Te_3 thin films (see Section 3.2.1), I compare here the BFMR of Au/Fe/Sb_2Te_3 and Au(5 nm)/Co(5 nm)/Sb_2Te_3 heterostructures, synthesized as described in Section 3.2.2. All the BFMR signals here reported are collected by means of a lock in amplifier as explained in Section 2.2.3.3 and thus fitted with Eq.2.34. In Fig. 3.32 (a) and (b), the acquired $f_{res}(H_{res})$ signals for the Au/Fe/Sb_2Te_3 and Au(5 nm)/Co(5 nm)/Sb_2Te_3 samples (black squares) are reported respectively. The red lines in Fig.3.32 indicate the fit of the datasets using the Kittel equation for the IP configuration (Eq.2.31). From this fit, I extracted the effective magnetization values for the 5 nm thick Fe and Co thin films, which are respectively $M_{eff}^{Fe} = 1172\ \pm 40\ emu/cm^3$ and $M_{eff}^{Co} = 569\ \pm 34\ emu/cm^3$. VSM measurements conducted on the same samples revealed that the values for the saturation magnetization are $M_s^{Fe} \sim 1092\ emu/cm^3$ and $M_s^{Co} \sim 1190\ emu/cm^3$ for Fe and Co respectively. It is important to notice that the M_s is reduced in both samples as compared to the tabulated values ($M_s^{Fe} \sim 1700\ emu/cm^3$, $M_s^{Co} \sim 1400\ emu/cm^3$), which is an indication of the presence of structural disorder or magnetic dead layers in our samples, but also a very frequent condition in the case of thin films. As introduced in Section 2.2.3.3, if M_{eff} and M_s are known, through Eq. 2.32 it is possible to extract the values for the surface magnetic anisotropy constant K_S in a FM film. As a result, we obtained $K_S^{Fe} = 0.34 \pm 0.01\ erg/cm^2$ and $K_S^{Co} = 0.99 \pm 0.01\ erg/cm^2$, values which reflect the influence of the surface-induced magnetic anisotropy.

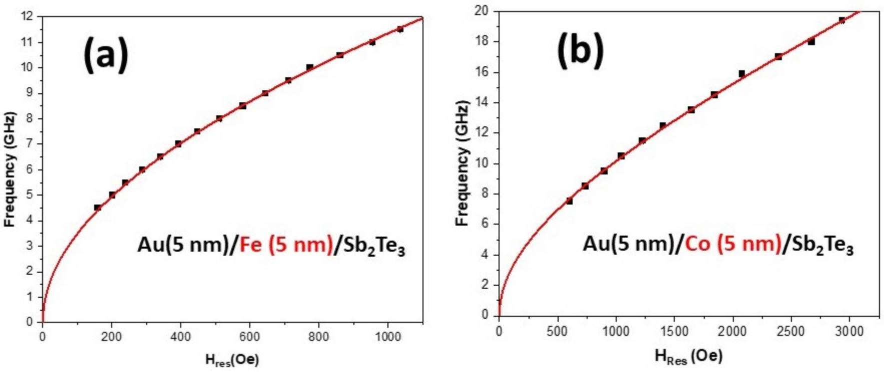

Figure 3.32: The $f_{res}(H_{res})$ dispersion for the samples (a) Au(5 nm)/Co(5 nm)/Sb_2Te_3 and (b) Au(5 nm)/Co(5 nm)/Sb_2Te_3 is reported. The evolution of the two curves (black squares) is well fitted with the Kittel equation (Eq.2.31)(red solid line). From the fit the M_{eff} and g-factor values are extracted for the two samples and reported in the text.

The latter values are in accordance with those reported in literature for similar FM thin films [134, 136]. K_s embeds all the surface-magnetic contributions, thus, in this case, coming from both the Au/FM and FM/Sb_2Te_3 interfaces. The same Kittel fits reported in Fig.3.32 allow the determination of the Fe and Co g-factors, yielding $g_{Fe} = 2.05 \pm 0.03$ and $g_{Co} = 2.54 \pm 0.06$. For the case of evaporated Co, the extracted g-factor value is compatible with that one obtained for the ALD-grown Co thin films ($g_{ALD-Co} = 2.4 \pm 0.2$) discussed in Section 3.1.3. The remarkable difference between the Fe and Co g-factors is supported by literature [68, 136] and in 3d transition metals correlated with their fine electronic structure, which depends on the interaction between the exchange Hamiltonian and the spin-orbit energy. [68] It has to be underlined here that the determination of the g-factor is challenging for the IP geometry due to the non-linearity of Eq. 2.31, thus measurements over a large frequency range are required to obtain reliable fits.

In Fig.3.33 (a) and (b), the frequency dependent linewidth of the BFMR signals for samples Au(5 nm)/Fe(5 nm)/Sb_2Te_3 and Au(5 nm)/Co(5 nm)/Sb_2Te_3 are reported respectively. From the linear interpolation of the data with Eq.2.37, the value of the damping parameter (α) and the inhomogeneous broadening (ΔH_0) are extracted for the two samples. As a result, it is obtained $\alpha_{Fe} = 0.022 \pm 0.001$, $\alpha_{Co} = 0.036 \pm 0.002$,

$\Delta H_0^{Fe} = 42 \pm 4\,Oe$ and $\Delta H_0^{Co} = 64 \pm 13\,Oe$. As explained in Section 2.2.3.5, the enhancement of the damping constant in the sample with Co could correspond to a higher spin mixing conductance ($g_{mix}^{\uparrow\downarrow}$, Eq. 2.41) in this sample and, as a consequence, to a SP effect at the Co/Sb_2Te_3 interface, when compared to the Fe/Sb_2Te_3 case.

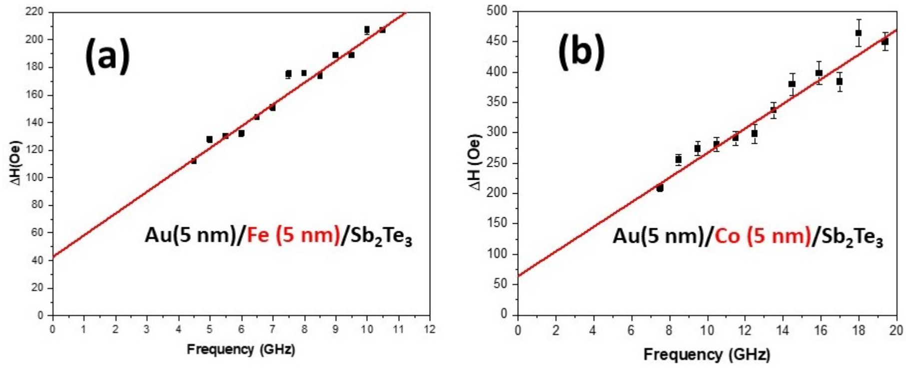

Figure 3.33: FMR signal linewidth (ΔH) as a function of the resonant frequency (f_{res}) for the samples (a) Au(5 nm)/Co(5 nm)/Sb_2Te_3 and (b) Au(5 nm)/Co(5 nm)/Sb_2Te_3. From the linear fit (red solid line, Eq. 2.37) are extracted the α and Δ_{H_0} values which are reported and discussed in the text.

In the following sections my focus is directed to get deeper insight into the origin of this apparent α enhancement in the Co/Sb_2Te_3 case. In particular, a thorough BFMR study as a function of Co thickness, and the influence of additional interlayers, are presented (Section 3.3.3).

3.3.3 Broadband-FMR in $Au/Co/epitaxial - Sb_2Te_3$ heterostructures

A series of Au(5 nm)/(Co(t)/Sb_2Te_3 samples, with nominal t = 2,4,5,6,7,10,15,30 nm, has been prepared by evaporating the Au(5nm/Co(t) bilayers on the top of the epitaxial MOCVD-deposited Sb_2Te_3 TI. In order to investigate on the magnetization dynamics in the Co thin films when in contact with the epitaxial Sb_2Te_3, a thorough BFMR study as a function of the Co thickness was performed. In Fig.3.34 (a) the evolution of the $f_{res}(H_{res})$ plots as a function of the Co thickness is shown. Here, for each Co thickness the acquired dataset (colored squares) was fitted with Eq.3.34 (red solid lines) and the M_{eff} and g-factor values extracted.

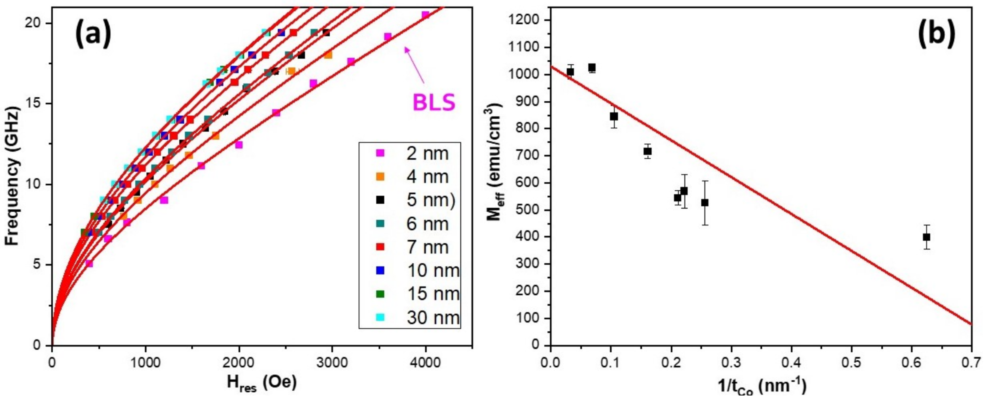

Figure 3.34: (a) Dependence of the $f_{res}(H_{res})$ signal as a function of the Co thickness (colored squares) in the Au(5nm)/Co(t)/Sb_2Te_3 samples. The solid red lines indicate the data fit with the Kittel equation for the IP geometry (Eq.2.31). (b) Values of M_{eff} extracted by the fits in (a) and plotted as a function of the inverse of the Co thickness ($1/t_{Co}$)) measured by XRR. From the fit with Eq.2.32 we have $M_s = 1030 \pm 70\,Oe$ and $K_s = 0.99 \pm 0.29\,erg/cm^2$.

The evolution of the Kittel fit as a function of the Co thickness is in accordance with similar measurements conducted by others [134, 136] and confirms the accurate Co-thickness control in our evaporator system (Section 3.2.2). Due to the weak FMR signals for the sample with Co(2 nm) (pink squares in Fig.3.34 (a)), in this case the $f_{res}(H_{res})$ signal was acquired by BLS measurements (Section 3.30). In Fig.3.34 (b) the values of M_{eff} extracted by the fit showed in Fig. 3.34(a) are plotted as a function of the inverse of the Co thickness. Here, from the fit of the data (black squares) using Eq.2.32 (red solid line), we obtained $M_s = 1030 \pm 70\,Oe$ and $K_s = 0.99 \pm 0.29\,erg/cm^2$. The M_s value extracted by BFMR results quite lower as compared the VSM measurement for the same samples (Fig.3.26), likely due to the reduced number of points in the graphic and their scattered linear dispersion. The M_{eff} value for each sample and further relevant parameters are summarized in Table 3.10, along with the nominal and real thicknesses of the Co thin films (measured by XRR, Section 2.2.2), the g-factor, ΔH_0 and α values. The K_s extracted by the $M_{eff}(1/t_{Co})$ curve and the Kittel curve from a single Co thickness (as for the sample with the 5 nm thick Co layer) have the same value, even if with a different error bar and confirms the reliability of the study. Beside the M_{eff} values, the g-factor for each Co thin film was calculated and reported in Table 3.10. The value of the extracted Co g-factors varies with the Co thickness but not with a clear trend. As already discussed, such variation can be attributed to both the difficulty to extract

Table 3.10: Summary of the main quantity extracted from the fits in Fig.3.34 and Fig.3.35.

Nom. Thick. (nm)	Real. Thick. t_{Co} (nm)	$t_{Co}{}^{-1}$ $(nm)^{-1}$	g-factor	M_{eff} (emu/cm^3)	ΔH_0 (Oe)	α (10^{-3})
2	1.6	0.625	2.45 ± 0.09	399 ± 44		
4	3.9	0.256	2.45 ± 0.14	526 ± 82	207 ± 19	44 ± 3
5	4.5	0.222	2.54 ± 0.1	569 ± 61	64 ± 13	36 ± 2
6	4.7	0.211	2.64 ± 0.05	545 ± 28	24 ± 7	30 ± 1
7	6.2	0.161	2.53 ± 0.04	716 ± 27	15 ±7	20 ± 1
10	9.5	0.105	2.46 ± 0.05	845 ± 41	11 ± 4	15 ± 0.6
15	14.5	0.069	2.34 ± 0.01	1024 ± 16	11 ± 2	12 ± 0.2
30	30	0.033	2.37 ± 0.03	1010 ± 28	25 ± 2	9.5 ± 0.3

this value from an IP FMR configuration and to possible modification of the Co interfaces properties (Section 3.3.1). Nevertheless, the g-factor values are in the range of $g^{Co} = 2.37 - 2.64$, which are typical for Co thin films. [136] In Fig.3.35(a) the $\Delta H(f_{res})$ curve as a function of the Co thickness is reported. According to Eq.2.37, from the slope of the linear fits showed in Fig.3.35(a) (red solid lines), it is possible to extract the value for the damping parameter α for each Co thickness (Table 3.10). Unfortunately, the quality of the FMR signal for the 2 nm sample was not enough to reasonably estimate the ΔH and α values.

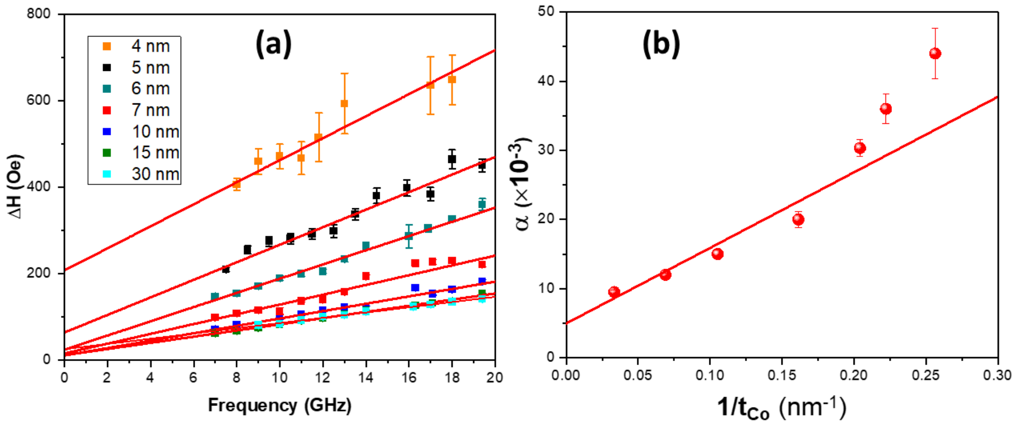

Figure 3.35: (a) FMR signal linewidth as a function of the resonant frequency for each Co thickness (colored squares) of the Au(5nm)/Co(t)/Sb_2Te_3 series. From the linear fit with Eq.2.37 (red solid lines) the α and ΔH_0 values were extracted. (b) Here the α values extracted from the fit in (a) are plotted as a function of the inverse of the Co thickness. The red line is the linear fit with Eq.2.41.

From the SP theory it is possible to link the trend of the α value as a function of the inverse of the thickness of a FM thin film extracting the $g_{eff}^{\uparrow\downarrow}$ value (Section 2.2.3.5), a quantity which is proportional to a spin current density flowing from the FM layer into the TI while the FMR is occurring. At a first glance, in order to calculate the $g_{eff}^{\uparrow\downarrow}$ value from our set of samples, in Fig.3.35(b) I plotted the α values extracted from Fig.3.35(a) (red circles), fitting their evolution with Eq.2.41. From this fit it results that $\alpha_{bulk} = 0.005 \pm\ 0.01$ and $g_{eff}^{\uparrow\downarrow} = 6.5 \pm\ 0.9 \cdot 10^{19} m^{-2}$. The α_{bulk} value results slightly lower than those reported in literature for Co thin films, usually in the range 0.008-0.011 [54, 134]. The extracted $g_{eff}^{\uparrow\downarrow}$ is comparable with many FM/TI or FM/HM systems and in this case also higher than in Co/Pt systems ($g_{mix}^{\uparrow\downarrow} = 4.5 \cdot 10^{19} m^{-2}$) [54], a benchmark in the context of SP.

However, it is clear from Fig.3.35(b), that for Co thickness below 6 nm the $\alpha(1/t_{Co})$ curve does not follow a linear trend. Despite the adopted fitting procedure is a standard for the interpretation of the $\alpha(1/t_{Co})$ curve in terms of SP effects across a FM/NM interface, the data collected in Fig.3.35(b) cannot be interpreted straightforwardly by means of Eq.2.41. The deviation from the linearity suggests the coexistence of additional contributions to α, which are predominant at lower thicknesses of the Co layer. A possible origin of the enhanced α values can be attributed to a magneto-structural disorder present in the Co films, which can be evaluated qualitatively by considering the inhomogeneous term ΔH_0. Indeed, for the thinnest samples the intercept with the y-axis is larger when compared to the thicker samples, indicating the presence of a higher magneto-structural disorder. As a consequence, the presence of impurities and defects in the Co thinner films could serve as scattering center for the precessing magnetization, which quickly damps towards the external magnetic field. On the other hand, the XRR and VSM measurements on these samples evidenced the high quality of the Co layer both by the structural and magnetic point of view (Section 3.2.2). Therefore, in order to attempt a more phenomenological description of the unconventional trend observed in Fig.3.35(b), we looked for a more comprehensive theoretical model. In a recent paper of L. Zhu *et al.*(2019) [54] the authors analysed the FMR response in several FM/HM nanometric heterostructures, pointing out that in the majority of the studied systems the SP is a relatively minor contribution to α, when measured in the gigahertz frequency region. Indeed, they suggested that two further terms have to be accounted to properly describe the $\alpha(1/t_{Co})$ curve, which are the Spin Memory Loss (SML) and Two-Magnon Scattering (TMS). The SML is an interface effect where the spin current pumped from the precessing magnetization in a FM crosses the interface with an adjacent layer can be partially backscattered. Recently, the main source of SML was attributed to the presence of an abrupt interruption (the interface) between a FM and a material with high SOC, such as HMs or TIs.[72] The other possible effect which needs to be taken into account is the TMS, which is an energy transfer mechanism between the FMR uniform mode and degenerate spin waves. [138, 143–146] As deeply discussed in Ref.[144, 147], the source of the TMS are defects and imperfections at the surfaces and interfaces of FM thin films, which act as a source of scattering. Indeed, the TMS is often related to the morphological and magnetic roughness at the FM/(HM or TI) interface. According to Ref.[54] the total damping can be seen as

$$\alpha = \alpha_{bulk} + \alpha_{SP} + \alpha_{TMS} \tag{3.5}$$

which explicated is expressed by the following parabolic function

$$\alpha = \alpha_{bulk} + (g^{\uparrow\downarrow}_{eff,mix} + g_{eff,SML})\frac{g\mu_B}{4\pi M_s}\frac{1}{t_{FM}} + \beta_{TMS}\frac{1}{t^2} \tag{3.6}$$

where $g^{\uparrow\downarrow}_{eff,mix}$ and $g_{eff,SML}$ are respectively the spin mixing conductance of the conventional SP theory (Eq.2.41) and the SML term taking into acount the spin current backflow at the FM/TI interface. The prefactor of the parabolic term β_{TMS} is the TMS coefficient, which is proportional to $(\frac{K_s}{M_s})^2$ and the density of the magnetic defects at the FM/(HM or TI) interface.[147] In Fig.3.36 the same dataset reported in Fig.3.35 is shown and fitted with Eq.3.6. In this thesis, we did not perform any measurement to separate the $g^{\uparrow\downarrow}_{eff,mix}$ from $g_{eff,SML}$ term of Eq.3.6, which are here treated as a single term renamed as $g_{eff,SP}$. Thus, from the global fit in Fig.3.36 we obtained $\alpha_{Bulk} = 0.0871$, $g_{eff,SP} = (0.8 \pm 1) \cdot 10^{19}\ m^{-2}$ and $\beta_{TMS} = (4.5 \pm 0.9) \cdot 10^{-19}\ m^{-2}$.

From this result emerges clearly how the values of the α_{Bulk} are now in accordance with the values generally reported for bulk Co,thus demonstrating how the inclusion of the TMS contribution is necessary in order to interpret our FMR data set, over the whole range of thicknesses. $g_{eff,SP}$ results drastically reduced as compared the value extracted with the conventional linear dispersion (Fig.3.35). Nevertheless, the $g_{eff,SP}$ is affected by a very high error bar, which is the natural consequence of the limited number of points in the linear region. It is very interesting to notice that, even if the SML contribution

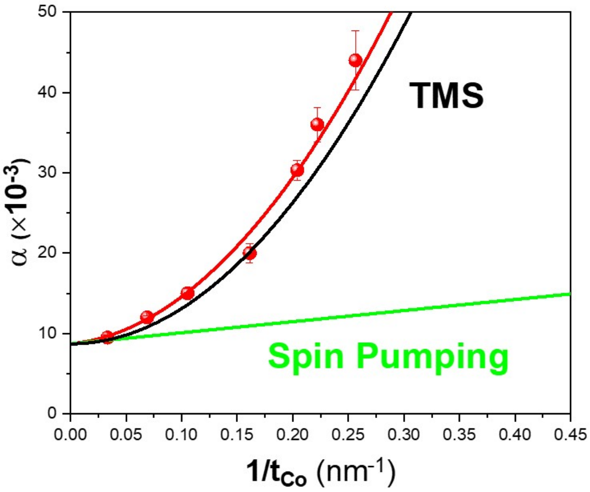

Figure 3.36: α vs. $1/t_{Co}$ dispersion (red circles), the same reported in Fig.3.35. The red solid line here indicate the fit of the collected points with Eq.3.6. The black and green lines indicate respectively the TMS and SP components extracted from the fit.

is expected to be large in systems characterized by high interface SOC, for our set of samples the linear region is very reduced as compared the parabolic one, suggesting that the SML is a negligible contribution to the FMR linewidth as compared to TMS. To our knowledge, so far the detection of TMS by means of BFMR measurements was observed only in FM/HM heterostructures.[54] Therefore, in this thesis I likely reported the first evidence of the importance of TMS also at the interface between FM and TI. As a result of the BFMR analysis on the Au/Co/Sb_2Te_3 samples, we learned that, within the detection limit of the XRR and VSM techniques, the overall quality of our evaporated Co thin films is good, but a more spatially confined chemical, structural and magnetic disorder at the Co/Sb_2Te_3 interface is likely present and turns out detrimental for the injection of pure spin currents from the Co into the Sb_2Te_3 layer (i.e. through TMS).
In order to test the possibility to reduce TMS contribution at the Co/Sb_2Te_3 interface, a set of Au(5 nm)/Co(t)/Au(5 nm)/Sb_2Te_3 samples has been produced, with t= 2.5, 4, 5,7,20 nm. In Fig.3.37(a) the Kittel curve for the Au(5 nm)/Co(t)/Au(5 nm)/Sb_2Te_3 samples is reported, where t = 2.5, 4, 5, 7, 20 nm are the nominal Co thicknesses.
Here, the evolution of the curves as a function of the Co thickness is in accordance with the same measurements discussed above. In Fig.3.37(b) the values of the M_{eff} extracted from the fit in Fig.3.37(a) are reported as a function of the inverse of the Co thickness

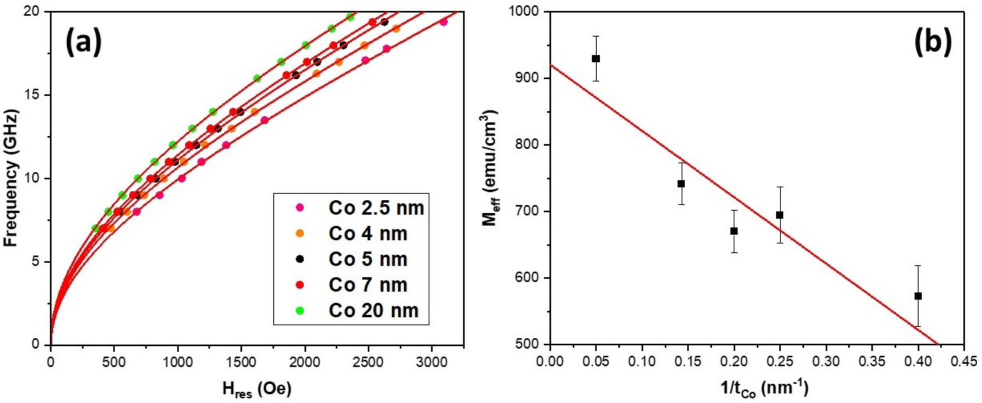

Figure 3.37: (a) Dependence of the $f_{res}(H_{res})$ signal as a function of the Co thickness (colored circles) in the Au(5nm)/Co(t)/Au(5nm)/Sb_2Te_3 samples. The solid red lines indicate the data fit with the Kittel equation reported in Eq.2.31. (b) Values of M_{eff} extracted by the fits in (a) and plotted as a function of the inverse of the Co thickness ($1/t_{Co}$)) (clack squares). From the fit with Eq.2.32 we have $M_s = 921 \pm\ 55\,Oe$ and $K_s = 0.58 \pm 0.18\,erg/cm^2$.

and fitted with Eq.2.32. As a result, we obtained $M_s = 921 \pm 55\ emu/cm^3$ and $K_s = 0.58{\pm}0.18\ erg/cm^2$. These values are quite lower than those extracted for the Co samples directly in contact with the Sb_2Te_3 layer. A possible reason can be attributed to the fcc crystalline structure of the Au substrate, which could promote the formation of a higher fraction of cubic crystalline grains in the polycrystalline film, as compared the same Co deposition on top of the hexagonal Sb_2Te_3. Indeed, as also reported in Ref.[136], for bulk fcc-Co $M_s \sim 1100\ emu/cm^3$, which is a lower than in the hex-Co ($M_s \sim 1400\ emu/cm^3$). On the other hand, the K_s values are in accordance with previous studies on Au/Co/Au sandwiches [133], suggesting that the Co magnetic moment remains close to the bulk value also for very thin Co thicknesses (down to 2.5 nm in this study). A confirmation of the homogeneity of the Co electronic structure over the whole range of thicknesses is given by the poorly dispersed values for the g-factors, which are all close to $g \sim 2.5$ (Table 3.11), compatible with typical values for Co thin films.[136, 148] In Fig.3.38(a) the $\Delta H(1/t_{Co})$ data for each Co thickness for the Au(5nm)/Co(t)/Au(5nm)/Sb_2Te_3 samples are reported (colored circles). As done previously for the set of Au/Co(t)/Sb_2Te_3 samples, the data are fitted with Eq.2.37 in order to extract the α and ΔH_0 values for each dataset. The obtained values are summarized in Table 3.11. A first remark concerns that here the ΔH_0 values are lower than those extracted for the Au/Co/Sb_2Te_3

heterostructures, indicating the higher magneto-structural quality of the Co thin films when grown on top of Au as compared to Sb_2Te_3.

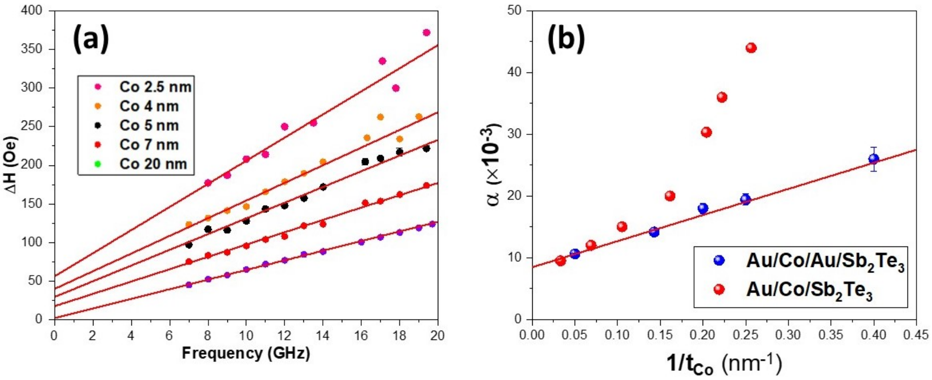

Figure 3.38: a) FMR signal linewidth as a function of the resonant frequency for each Co thickness (colored squares) of the Au(5nm)/Co(t)/Au(5nm)/Sb_2Te_3 samples. From the linear fit with Eq.2.37 (red solid lines) the α and ΔH_0 values were extracted. (b) A comparison between the α values reported in Fig.3.35 (red circles) and those extracted from the fit in (b) (blue circles). The red line indicates the linear fit of the blue circles with Eq.2.41, from which the α_{bulk} and $g_{eff}^{\uparrow\downarrow}$ values reported in the main text are extracted.

In Fig.3.38(b), the α values obtained from the linear fits in Fig.3.38(a) (blue circles) are plotted as a function of the inverse of the Co thickness and compared with the same values extracted from the Au/Co/Sb_2Te_3 samples reported in Fig.3.35(b) (red circles). As it is clear from Fig.3.38(b), for the Au/Co/Au/Sb_2Te_3 sample the parabolic component of the $\alpha(1/t_{Co})$ curve is completely suppressed within the examined thicknesses range, and the Au/Co/Au/Sb_2Te_3 data can be perfectly interpreted with Eq.2.41. No TMS is present with the insertion of the Au interlayer, and the extracted α values can be attributed to genuine SP from Co across the Au(5 nm) interlayer into the epitaxial Sb_2Te_3. From the fit the $\alpha_{bulk} = 0.0085 \pm\ 0.0002$ and $g_{eff}^{\uparrow\downarrow} = (2.11 \pm\ 0.12) \cdot 10^{19}\ m^{-2}$ are obtained. In this case, the extracted α_{Bulk} value is well in the range of the typical values for Co thin films [136] and the $g_{eff}^{\uparrow\downarrow}$ a value consistent with most of the (FM/HM or TI) systems (see below Fig.3.39 for a comparison between our data and those of interest in the literature). The main parameters extracted from the fits in Fig.3.37 and Fig.3.38 are summarized in Table 3.11. Anyway, it is important to highlight that through the FMR analysis discussed above, it is not possible to quantify the SML contribution affecting the slope of the linear fit of the blue points in Fig.3.38, which could lead to an overestimation of the $g_{eff}^{\uparrow\downarrow}$ value.

Table 3.11: Summary of the main quantity extracted from the fits in Fig.3.37 and Fig.3.38.

Nom. Thick. (nm)	${t_{Co}}^{-1}$ $(nm)^{-1}$	g-factor	M_{eff} (emu/cm^3)	ΔH_0 (Oe)	α (10^{-3})
2.5	0.4	2.48 ± 0.09	573 ± 46	67 ± 14	26 ± 2
4	0.25	2.43 ± 0.05	695 ± 42	39± 6	19 ± 0.9
5	0.2	2.58 ± 0.05	670 ± 32	30 ± 5	18 ± 0.8
7	0.14	2.54 ± 0.05	742 ± 31	17 ± 1.9	14 ± 0.3
20	0.05	2.45 ± 0.04	930± 34	2 ± 0.8	11 ± 0.2

In the context of the SP theory, to determine the $g_{eff}^{\uparrow\downarrow}$ parameter is crucial to calculate the efficiency of a SP process across a generic FM/NM interface (Section 2.2.3.5). Indeed, $g_{eff}^{\uparrow\downarrow}$ enters directly in the calculation of the generated spin current density in a FM as reported in Eq.2.42. From literature, it turned out that the most frequent values for $g_{eff}^{\uparrow\downarrow}$ in FM/HM, FM/TI and FM/Interlayer/(HM or TI) are typically in the range of $10^{18} - 10^{20}$ m^{-2}. In order to have a more complete picture, in Fig.3.39 the $g_{eff}^{\uparrow\downarrow}$ values for some of these systems reported in literature and calculated with different approaches are shown. As we can see, the $g_{eff}^{\uparrow\downarrow}$ values extracted from our samples are of the same order of magnitude of the majority of the reported heterostructures. If a FM thin film is in contact with a good spin sink NM layer, the generation of pure spin currents from the FM into NM should be related to a high value of the measured $g_{eff}^{\uparrow\downarrow}$ in this heterostructure (Eq.2.41). In principle, in a FM/Interlayer/NM structure, the spin transport could be dependent from the thickness of the interlayer, due to the finite value of λ_s(Eq.2.55). Therefore, the introduction of interlayers could be detrimental for an efficient spin transport from FMs into the NM layers. From a comparison between the reported $g_{eff}^{\uparrow\downarrow}$ values in Fig.3.39, it is not possible to identify a trend which can be used to clarify the role about the use of interlayers to generate higher spin currents.

The latter considerations suggest that the role of the intermixing between materials is the key aspect to consider. For instance, from the theory of TIs, we know that the topological surface states are robust against the disorder of non-magnetic origin (i.e. non-magnetic impurities), but clearly in FM/TI systems some intermixing occurs between the materials, possibly modifying the properties of the TI layer. [149, 150]

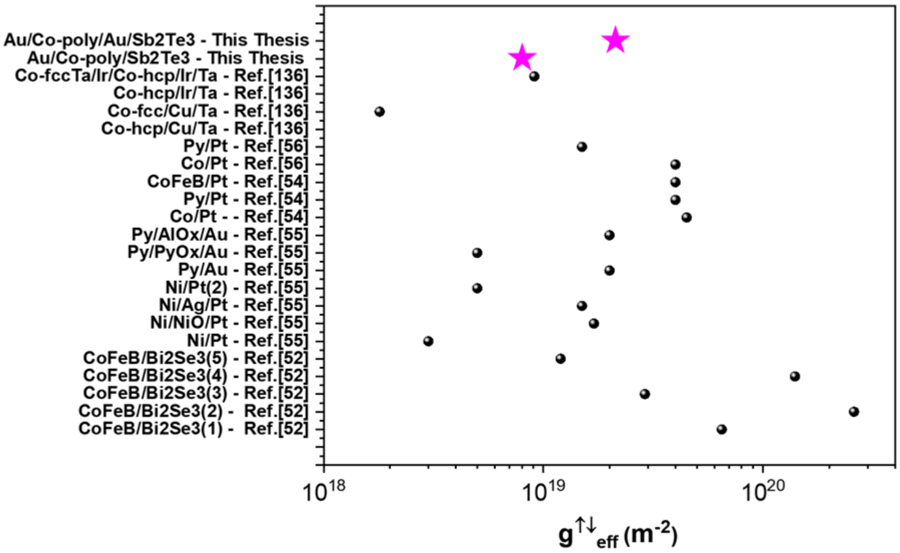

Figure 3.39: A collection of several $g^{\uparrow\downarrow}_{eff}$ values for different SP systems is shown (x-axis). On the y-axis the structure and the reference paper are indicated for each $g^{\uparrow\downarrow}_{eff}$ value. The pink stars indicate the $g^{\uparrow\downarrow}_{eff}$values extracted from the Au/Co/Sb_2Te_3 and Au/Co/Au/Sb_2Te_3 heterostructures studied in this thesis.

3.4 Spin Pumping in $Au/Co/Au/epitaxial{-}Sb_2Te_3$ heterostructures

In the following, the spin-to-charge conversion mechanism in the Au(5 nm)/Co(5 nm)/Au(5 nm)/Sb_2Te_3 heterostructure previously discussed in Section 3.3.3 is investigated through SP measurements. Moreover, in order to isolate the contribution associated to each layer of the stack, complementary SP measurements on Au(5 nm)/Co(5 nm)/Au(5 nm)/Si(111) and Co(5 nm)/Au(5 nm)/Si(111) were performed. Along this section, the latter samples are respectively indicated with S1, S2, S3.

In Fig. 3.40 (a) the DC voltage signal V_{mix} acquired for sample S1 is given for an RF-power of 73 mW and RF-frequency at 10.5 GHz (black circles). Here, the red circles represent the FMR signal for the same sample. Clearly, V_{mix} is related to the FMR response of the system (see Section 2.2.3.5).

According to the SP theory (see Section 2.2.3.5), if the direction of the applied mag-

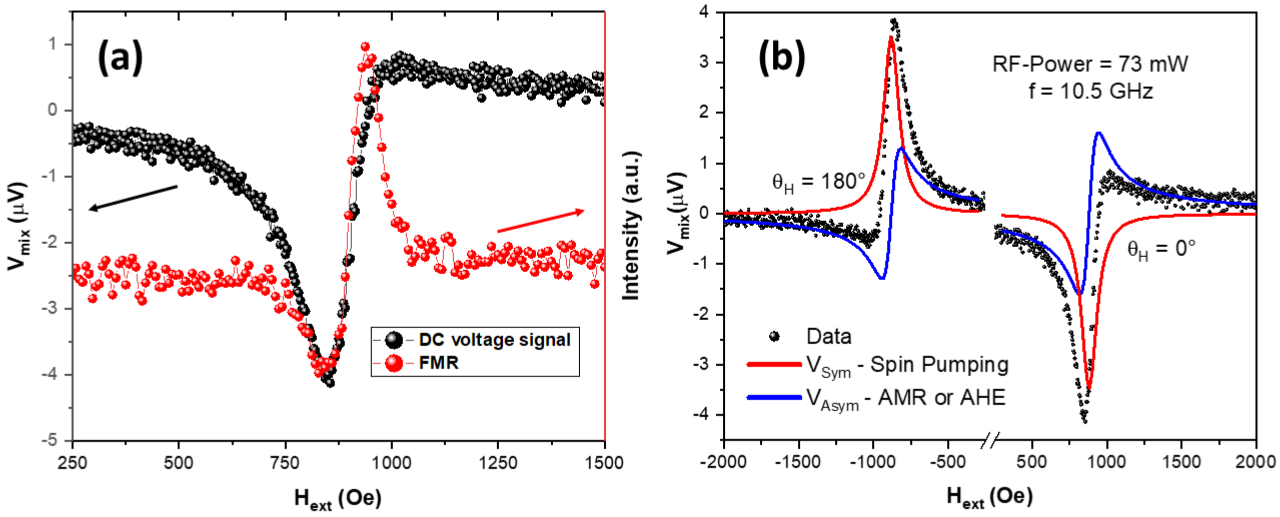

Figure 3.40: (a) SP DC voltage signal for sample S1 acquired at f = 10.5 GHz (black circles). The FMR signal at the same resonant frequency is acquired (red circles), showing the match of the resonant magnetic field as compared to the SP signal.(b) The same SP measurement reported in (a) is performed also for negative values of the external magnetic field. Here, it is evident as the asymmetric component V_{Asym} does not depend on the sign of the magnetic field, which is typical for rectification effects due to AMR and AHE. On the contrary, the symmetric component V_{Sym} changes the sign according to the sign of the magnetic field, indicating a magnetic field dependent spin accumulation. The latter condition is in accordance with SP effects.

netic field is reversed also the sign of the DC voltage relative to the SP contribution is reversed. In Fig. 3.40(b), a comparison of the V_{mix} spectra for S1 obtained for positive and negative magnetic fields is shown. The two curves (black circles) are fitted with the Lorentzian function reported in Eq.2.45, from which the symmetric (V_{Sym}) and anti-symmetric (V_{Asym}) parts are separated. As discussed in Section 2.2.3.5, V_{Asym} is originated from the AMR and the AHE of the Au/Co/Au trilayer and V_{Sym} from the spin-to-charge conversion. The V_{Sym} component can be also affected by the thermal Seebeck effect [48], thus in order to extract the DC signal arising only from the pure SP effect, we define an effective SP voltage as

$$V_{SP} = V_{Sym}^{eff} = \frac{V_{Sym}(+H_{ext}) - V_{Sym}(-H_{ext})}{2} \tag{3.7}$$

The value of V_{SP} extracted from the measurement in Fig.3.40(b) is $V_{SP} = 3.52\ \mu V$. The generated 2D charge current density can be calculated as

$$J_c^{2D} = \frac{V_{SP}}{WR} \tag{3.8}$$

where W and R are the width of the samples and their sheet resistance (see Section 2.2.3.5, Fig. 3.4). In particular, the R values for all the measured samples are extracted by independent four points measurements. In Table 3.12 the main parameters characterizing sample S1, S2 and S3 are reported.

Table 3.12: The stack, the main geometrical and electrical quantity needed to extract the SCC efficiency in the studied systems are reported. In the column indicating the samples stack the numbers in brackets represent the thicknesses of each layer expressed in nm. W indicate the width of each sample, R the sheet resistance, V_{Sym} the symmetric Lorentzian extracted from the fits in Fig.3.42 and J_c^{2D} the 2D charge current density generated during the SP experiment.

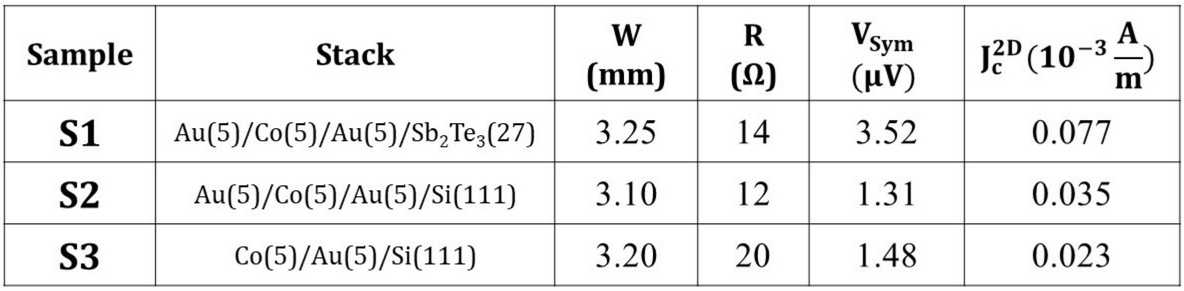

Sample	**Stack**	**W (mm)**	**R (Ω)**	**V_{Sym} (μV)**	**J_c^{2D} ($10^{-3}\frac{A}{m}$)**
S1	Au(5)/Co(5)/Au(5)/Sb_2Te_3(27)	3.25	14	3.52	0.077
S2	Au(5)/Co(5)/Au(5)/Si(111)	3.10	12	1.31	0.035
S3	Co(5)/Au(5)/Si(111)	3.20	20	1.48	0.023

In Fig.3.41(a) the V_{mix} value for sample S1 is reported at fixed frequency (10.5 GHz) as a function of the RF-power. In Fig.3.41(b), the V_{Sym} and V_{Asym} values extracted from the panel (a) are plotted as a function of the RF-power, showing their linear behavior. The SP arises as a consequence of the magnetization-precession relaxation, which generates a pure spin current in the FM layer proportional to the damping term of Eq.2.39. The DC component of J_S^{3D} is proportional to the projection of the $\vec{M} \times \frac{d\vec{M}}{dt}$ term on the external magnetic field direction. According to the SP theory [151], such projection is proportional to the square of the magnetization precession amplitude. Thus, J_S^{3D}, or the ISHE DC voltage signal as well, is proportional to the square of the magnetization precession amplitude or the square of the applied microwave amplitude. In virtue of that, the ISHE signal V_{Sym}, should be linear in the RF-power, which is consistent with the trend observed in Fig.3.41(b).

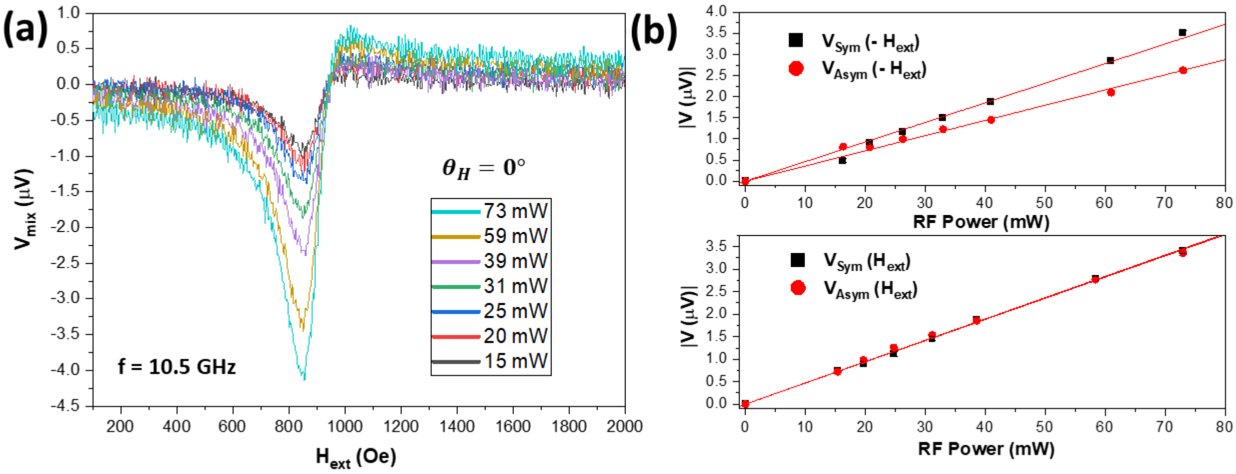

Figure 3.41: (a) The SP DC voltage plotted as a function of the RF-power. (b) Modulus of the V_{mix} symmetric and anti-symmetric components as a function of the RF-power acquired at negative (top panel) and positive (bottom panel) external magnetic fields. The linear evolution is consistent with the SP theory. [151]

The data fitted in Fig.3.40 and Fig.3.41 demonstrated the presence of SCC in sample S1, but the complexity of its structure makes difficult a straightforward identification of the precise role played by each layer.

As reported in Ref.[152], the Au has a non negligible θ_{SHE} which is expected to be in the range 0.0004 - 0.008. Therefore, a non zero contribution in the generated J_c^{2D} is expected from the Au layers composing S1. In order to isolate the effect of the Sb_2Te_3 layer, complementary samples S2 and S3 were produced. In Fig. 3.42 the $V_{mix}(H_{ext} - H_{res})$ curves for sample S1, S2 and S3 are reported. In order to compare the effective charge current density generated in each sample, in Fig. 3.42(b) the J_c^{2D} values for the sample reported in Fig.3.42(a) are extracted using the following parameters summarized in Table 3.12.

Comparing the J_c^{2D} values for sample S1 (black line) and S2 (blue line) in Fig.3.42(b)an enhancement of the 120% is observed, which demonstrates that the presence of the Sb_2Te_3 TI produces a clear extra contribution to the SCC. Moreover, the different J_c^{2D} values for samples S2 and S3 indicate that the spin current J_s^{3D} is simultaneously pumped from Co in both the Au layers. Thus, most likely, in sample S1 the spin current pumped into the Au capping layer is reflected back at the Au/air interface and subsequently absorbed by the Sb_2Te_3 substrate. Considering that λ_s for Co and Au is $\sim 10\ nm$ and

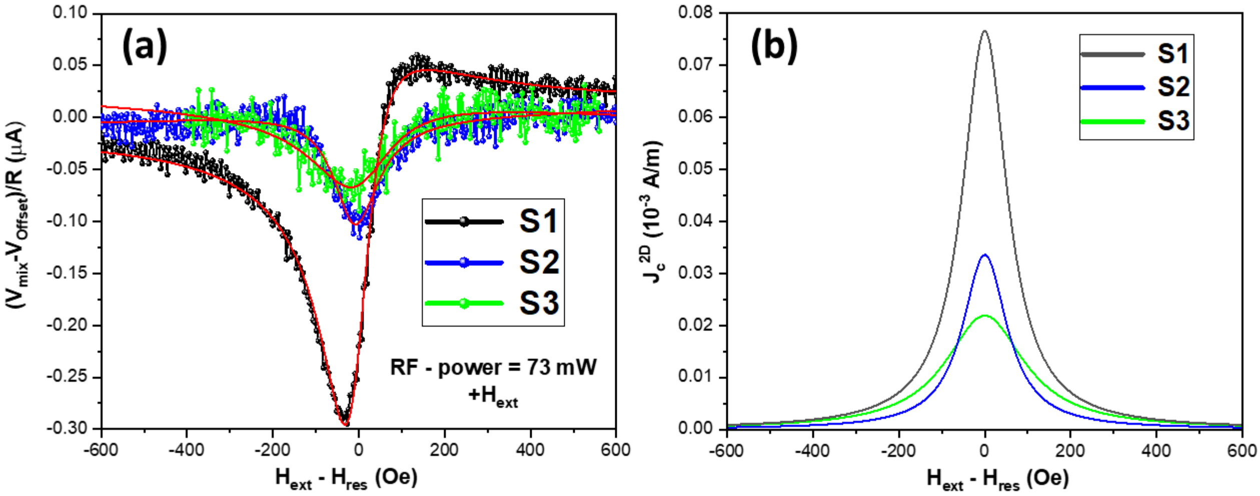

Figure 3.42: (a) V_{mix} signal acquired for samples S1 (black dots), S2 (blue dots) and S3 (green dots) and normalized for the R value for each sample. (b) 2D charge current density extracted by the V_{Sym} component of the V_{mix} signals reported in (a) and calculated using Eq. 3.8.

$\sim 35\ nm$ respectively [82, 153], a tentative sketch of the J_s^{3D} scheme in S1, S2 and S3 is depicted in Fig. 3.43. Here, the J_s^{3D} back-flows for the Au/Sb_2Te_3 and Au/Si(111) interfaces are not considered.

As discussed is Section 2.2.3.5, the SCC efficiency in a FM/TI heterostructure is proportional to the ratio $\propto \frac{J_c^{2D}}{J_s^{3D}}$, where J_s^{3D} depends on the $g_{eff}^{\uparrow\downarrow}$ as reported in Eq. 2.41. In order to extract the additional contribution to spin pumping (and therefore to SCC) purely coming from the the Sb_2Te_3 layer, the $g_{eff,Sb_2Te_3}^{\uparrow\downarrow}$ was calculated by taking the difference between the $g_{eff}^{\uparrow\downarrow}$ for sample S1 and that in the reference S2 one as depicted in Eq.3.9, and similarly as previously reported. [52, 53, 58, 82, 154]

$$g_{eff,Sb_2Te_3}^{\uparrow\downarrow} = \frac{2M_s\gamma\ t_{Co}}{g\mu_B f}(\Delta H_{S1} - \Delta H_{S2}) \tag{3.9}$$

In the latter equation, $\Delta H_{S1} = 66.9 \pm 0.7\ Oe$ and $\Delta H_{S2} = 63.9 \pm 1.1\ Oe$ are the HWHM of the SP signals for S1 and S2 extracted from the data showed in Fig. 3.42(a), being $\Delta H_{S1} - \Delta H_{S2} \sim 3\ Oe$. A lower $\Delta H_{S1} - \Delta H_{S2} \sim 1\ Oe$ is obtained by extracting the linewidth from the FMR signals at 10.5 GHz for the two samples, but a larger experimental error prevents to draw firm conclusions. Therefore, by considering

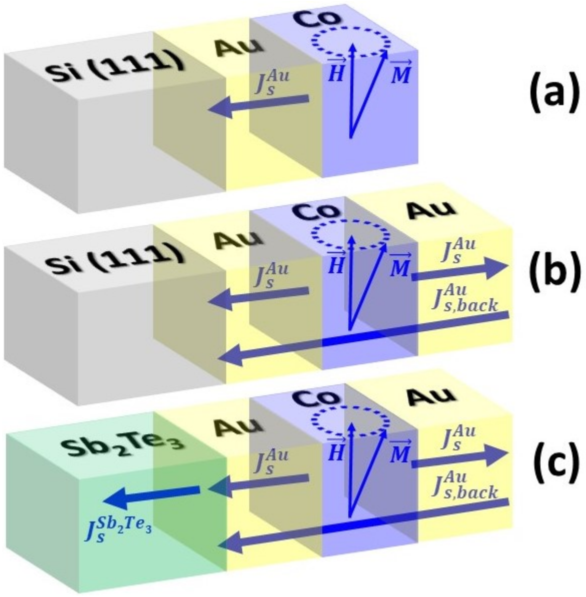

Figure 3.43: A sketch of the stack of samples S1 (a), S2 (b) and S3 (c) is shown and a possible model of the generated J_s^{3D} currents in each system is reported.

the (more conservative) estimation of $\Delta H_{S1} - \Delta H_{S2} \sim 3\ Oe$ to calculate $g^{\uparrow\downarrow}_{eff,Sb_2Te_3}$ a $g^{\uparrow\downarrow}_{eff,Sb_22Te_3} = 1.78 \times 10^{18} m^{-2}$ is obtained, by using the M_s, γ and g parameters extracted from the BFMR measurements reported in Fig.3.37 for $t_{Co} = 5\ nm$. The corresponding value of the 3D pure spin current injected in the Sb_2Te_3 layer is $J_s^{3D} = 1.32 \times 10^5\ Am^{-2}$. For sample S3 the HWHM is larger than S1 and S2, likely due to the lack of a capping layer which favored the partial oxidation of the Co film. Indeed, the disorder introduced in the Co crystalline structure is reflected on the magnetic properties of the Co film provoking an enhancement of the α value, which is connected to the larger ΔH.

In Section 2.2.3.5, we discussed two possible models to describe the SCC efficiency in a FM/TI systems. If the spin diffusion in the TI layer is neglected, the spin current generated in the FM layer will be fully absorbed by the surface/interface states of the FM/TI heterostucture according to the EE description (see Section 2.52). On the contrary, if also the bulk states of the TI contribute in the SCC, the spin diffusion in the TI layer must be taken into account in terms of the ISHE (see Section 2.48). In absence of further insights about the nature of the SCC in the studied systems, in this thesis the

SCC efficiency for sample S1 is extracted following both approaches.

If the SCC in sample S1 involves solely the surface states of the Sb_2Te_3 TI, according to the EE model (see Eq.2.52) the SCC efficiency is $\lambda_{IEE} = 0.6\ nm$. This value for the Sb_2Te_3 TI is surprisingly high, being one order of magnitude larger than the majority of the chalcogenide-based TIs reported in literature, and typically grown by MBE (see Section 1.4). However, as introduced in Section 2.52, for a TI it turns out that $\lambda_{IEE} = \lambda_{mf}$, which is in this case in the nanometer range, constituting the upper limit for the electronic ballistic transport across the Sb_2Te_3/Au interface. Interestingly, this value is lower than those reported for free standing Sb_2Te_3 surfaces, where λ_{mf} can reach several tens of nanometers, as reported in Ref.[155]. In the latter work, the Fermi velocity for the electrons flowing in the TSS of a crystalline Sb_2Te_3 3D-TI thin film was extracted from scanning tunnel spectroscopy measurements as being $v_f \sim 4.3 \times 10^5\ m/s$. Using this value and the λ_{IEE} extracted by the SP experiments conducted on sample S1, a relaxation time $\tau_p \sim 1.4\ fs$ is obtained. Despite of being non-FM, the Au interlayer in the Au/Co/Au/Sb_2Te_3 system is therefore effective to suppress undesired effects at the Co/Sb_2Te_3 interface (such as TMS, see Section 3.3.3). On the other hand, the presence of a metallic layer in contact with the Sb_2Te_3 layer could introduce additional relaxation mechanisms for the electronic current generated in the Sb_2Te_3 TSS with the adjacent metallic layer. In view of that, as proposed for instance in Ref. [49, 60], the use of an insulating interlayer could be a better strategy, preserving more efficiently the TSS and consequently pushing the λ_{IEE} towards higher values.

Alternatively to a pure 2D charge current generation, if the SCC efficiency is attributed to the (bulk) ISHE, the value of θ_{SHE} can be obtained through Eq.2.57. It has to be underlined that, through the SP measurements reported in this thesis only the $\theta_{SHE}\lambda_s$ is a measurable quantity, therefore an independent estimation of the λ_s is needed to extract the θ_{SHE} value. In order to quantify λ_s, magnetotransport measurements on the bare Sb_2Te_3 TI were performed (not shown). By extrapolating the low temperature magnetotransport data at RT, a phase coherence length $l_\phi = 22\ nm$ is extracted. As deeply discussed in Ref. [156], in general l_ϕ is different from λ_s, but as a first approximation, we assumed that $l_\phi \simeq \lambda_s$. As a result, $\theta_{SHE}^{\lambda_s=22\ nm} \sim 0.05$, which is consistent with values extracted for chalchogenide-based TIs for instance in Ref.[38, 52] and two order of magnitude larger than in Ref.[157]. However, in several works the λ_s value is assumed starting from many different hypothesis [55, 157] or from values reported by someone else in literature (Sup.Info of Ref.[52]), and in very few cases directly calculated. The latter condition makes difficult to identify a universal approach to compare our results with those found in literature. Therefore, in order to provide a more general description of our system and its potentiality, we considered also a lower $\lambda_s = 5\ nm$ for the Sb_2Te_3 TI, a typical value assumed for other more studied chalcogenide-based TI such as Bi_2Te_3 and Bi_2Se_3.[52] According to the latter condition, we calculated $\theta_{SHE}^{\lambda_s=5\ nm} \sim 0.12$. The $0.05 < \theta_{SHE} < 0.12$ range provides a realistic forecast for the θ_{SHE} value in our 30 nm thick MOCVD-grown Sb_2Te_3 TI, demonstrating that it is very competitive in terms of SCC efficiency with those already reported in literature.[32, 158]

Chapter 4

Conclusions

This thesis summarizes the main scientific results that I collected during my three years long PhD career. During this period, I spent my efforts in studying the chemical-structural and magnetic properties of Fe and Co thin films in contact with the Sb_2Te_3 3D-TI, in order to obtain an efficient SCC at the (Fe,Co)/Sb_2Te_3 interface for application in spintronics.
In Chapter 1, I provided an overview on the general concepts concerning the evolution of the spintronic devices throughout the history, with particular care in the description of the state of the art of the most promising spintronic devices studied in the recent literature (see Section 1.4). The possible industrial transfer of the technology discussed in this thesis covered a central role during my research activity, therefore the production of the Sb_2Te_3 and parts of the FM thin films was performed using large-area (4 inch) chemical methods (i.e. MOCVD, ALD) as reported in Chapter 2. In this chapter, also the basics of XRD/XRR, FMR and SP-FMR were discussed, being the main techniques that I personally adopted for the samples characterization.

Chapter 3 is divided in four main sections, where I presented the results obtained on the (Fe,Co)/granular-Sb_2Te_3, Au/Co/epitaxial-Sb_2Te_3 and Au/Co/Au/epitaxial-Sb_2Te_3 heterostructures.
In Section 3.1, I studied the chemical-structural and magnetic properties of the Fe/granular-Sb_2Te_3 interface, evidencing a marked intermixing between the materials and a general tendency of Fe atoms in forming the FeTe compound. Subsequently, rapid and mild

thermal treatments performed on the granular-Sb_2Te_3 substrate prior to Fe deposition demonstrated to stabilize a sharper and chemically stable Fe/granular-Sb_2Te_3 interface. In the same section, ALD-grown Co thin films were studied when in contact with the granular-Sb_2Te_3 substrate, showing the possibility to produce high quality Co/granular-Sb_2Te_3 interface and the area selectivity of the deposition process.

In Section 3.2, the possibility to improve the structural quality of the Sb_2Te_3 thin films through thermal treatments was deeply discussed. Here, an enhancement of the Sb_2Te_3 thin film texturization was observed, leading the initial Sb_2Te_3 granular fashion towards a nearly single crystalline structure. Moreover, the integration of Fe and Co thin films with the epitaxial-Sb_2Te_3 was discussed and the improved chemical-structural and magnetic properties of the Fe,Co/epitaxial-Sb_2Te_3 heterostructures were pointed out in comparison with similar systems with the granular-Sb_2Te_3.

In order to investigate on the magnetization dynamics in Co/Sb_2Te_3 systems, their FMR response was analyzed in Section 3.3. What emerged from this study can be summarized in three points:

1. The use of the ALD to deposit metallic Co thin films on top of the granular Sb_2Te_3 turned out to be a valid strategy to tune the structural properties of Co which are inherently related to its magnetic anisotropy;
2. The use of epitaxial Sb_2Te_3 thin films and a Au capping layer to produce Au/Co/epitaxial-Sb_2Te_3 heterostructures gave the possibility to investigate on the spin transport across the Co/epitaxial-Sb_2Te_3 interface (i.e. spin pumping). As a result, the magnetization dynamics in such a system was explained considering a dominant TMS contribution likely arising due to the presence of an unwanted magnetic roughness at the Co/epitaxial-Sb_2Te_3 interface;
3. The introduction of a Au interlayer at the Co/epitaxial-Sb_2Te_3 interface was shown to be beneficial for the complete suppression of the TMS contribution evidenced in the structure without the Au interlayer, producing sharper and "magnetically cleaner" interfaces;

In Section 3.4, SP-FMR experiments on the optimized Au/Co/Au/epitaxial-Sb_2Te_3 heterostructures are discussed, highlighting the role played by the Sb_2Te_3 3D-TI in the SP process. This system was studied adopting two theoretical models for the data interpretation, which, in both cases, showed the high SCC efficiency achieved in such system ($\lambda_{IEE} = 0.6\ nm$ and $\theta_{SHE} = 0.05 - 0.12$).

Bibliography

[1] Toru Baji. “Evolution of the GPU Device widely used in AI and Massive Parallel Processing”. In: *2018 IEEE Electron Devices Technology and Manufacturing Conference, EDTM 2018 - Proceedings* (2018), pp. 7–9. DOI: `10.1109/EDTM.2018.8421507`.

[2] A M Tashtoush. “The Key to Prosperity for the Development of Prosthetic Technology Through Micro-Nanotechnology”. In: *Acta Materialia Turcica* 4.July (2020), pp. 16–24.

[3] J.M.D. Coey and T.R. Ni Mhíocháin. “History of Magnetism”. In: *Reference Module in Materials Science and Materials Engineering*. Elsevier, 2016. ISBN: 978-0-12-803581-8. DOI: `10.1016/b978-0-12-803581-8.01110-3`. URL: `http://www.sciencedirect.com/science/article/pii/B9780128035818011103`.

[4] J. M.D. Coey. “Magnetism in future”. In: *Journal of Magnetism and Magnetic Materials* 226-230.PART II (2001), pp. 2107–2112. ISSN: 03048853. DOI: `10.1016/S0304-8853(01)00023-3`.

[5] Yongbing Xu, David D. Awschalom, and Junsaku Nitta. *Handbook of spintronics*. 2015, pp. 1–1596. ISBN: 9789400768925. DOI: `10.1007/978-94-007-6892-5`.

[6] *Albert Fert - Nobel Lecture: The Origin, Development and Future of Spintronics*. URL: `https://www.nobelprize.org/prizes/physics/2007/fert/lecture/`.

[7] Stuart Parkin et al. “Magnetic Tunnel Junctions”. In: *Handbook of Magnetism and Advanced Magnetic Materials*. 2007, pp. 1–7. DOI: `10.1002/9780470022184.hmm509`.

[8] J. C. Slonczewski. “Current-driven excitation of magnetic multilayers”. In: *Journal of Magnetism and Magnetic Materials* 159.1-2 (1996). ISSN: 03048853. DOI: `10.1016/0304-8853(96)00062-5`.

[9] Hao Cai et al. “High performance MRAM with spin-transfer-torque and voltage-controlled magnetic anisotropy effects”. In: *Applied Sciences (Switzerland)* 7.9 (2017). ISSN: 20763417. DOI: `10.3390/app7090929`.

[10] Stuart S.P. Parkin, Masamitsu Hayashi, and Luc Thomas. *Magnetic domain-wall racetrack memory.* 2008. DOI: `10.1126/science.1145799`. URL: `http://science.sciencemag.org/`.

[11] A. Digiacomo et al. “Engineering Domain-Wall Motion in Co-Fe- B/Mg O Ultra-thin Films with Perpendicular Anisotropy Using Patterned Substrates with Sub-nanometer Step Modulation”. In: *Physical Review Applied* 10.6 (2018), p. 64053. ISSN: 23317019. DOI: `10.1103/PhysRevApplied.10.064053`.

[12] R. Lo Conte et al. “Role of B diffusion in the interfacial Dzyaloshinskii-Moriya interaction in Ta/Co20 F e60 B20/MgO nanowires”. In: *Physical Review B - Condensed Matter and Materials Physics* 91.1 (2015), pp. 1–9. ISSN: 1550235X. DOI: `10.1103/PhysRevB.91.014433`.

[13] W. S. Zhao et al. “Magnetic domain-wall racetrack memory for high density and fast data storage”. In: *ICSICT 2012 - 2012 IEEE 11th International Conference on Solid-State and Integrated Circuit Technology, Proceedings* (2012), pp. 7–10. DOI: `10.1109/ICSICT.2012.6466687`.

[14] C. Burrowes et al. “Low depinning fields in Ta-CoFeB-MgO ultrathin films with perpendicular magnetic anisotropy”. In: *Applied Physics Letters* 103.18 (2013). ISSN: 00036951. DOI: `10.1063/1.4826439`.

[15] L. Herrera Diez et al. “Enhancement of the Dzyaloshinskii-Moriya interaction and domain wall velocity through interface intermixing in Ta/CoFeB/MgO”. In: *Physical Review B* 99.5 (2019), pp. 1–9. ISSN: 24699969. DOI: `10.1103/PhysRevB.99.054431`.

[16] Frances Hellman et al. “Interface-induced phenomena in magnetism”. In: *Reviews of Modern Physics* 89.2 (June 2017), p. 25006. ISSN: 15390756. DOI: `10.1103/RevModPhys.89.025006`. arXiv: `1607.00439`.

[17] Jairo Sinova et al. "Spin Hall effects". In: *Reviews of Modern Physics* 87.4 (Oct. 2015), pp. 1213–1260. ISSN: 15390756. DOI: `10.1103/RevModPhys.87.1213`.

[18] A. R. Mellnik et al. "Spin-transfer torque generated by a topological insulator". In: *Nature* 511.7510 (July 2014), pp. 449–451. ISSN: 14764687. DOI: `10.1038/nature13534`.

[19] Anjan Soumyanarayanan et al. *Emergent phenomena induced by spin-orbit coupling at surfaces and interfaces.* Nov. 2016. DOI: `10.1038/nature19820`. arXiv: `1611.09521`.

[20] Joseph Sklenar et al. "Perspective: Interface generation of spin-orbit torques". In: *Journal of Applied Physics* 120.18 (Nov. 2016), p. 180901. ISSN: 10897550. DOI: `10.1063/1.4967391`. URL: `http://aip.scitation.org/doi/10.1063/1.4967391`.

[21] Luqiao Liu et al. "Spin-torque switching with the giant spin hall effect of tantalum". In: *Science* 336.6081 (May 2012), pp. 555–558. ISSN: 10959203. DOI: `10.1126/science.1218197`. arXiv: `1203.2875`.

[22] K. Ando et al. "Electric manipulation of spin relaxation using the spin hall effect". In: *Physical Review Letters* 101.3 (July 2008), p. 036601. ISSN: 00319007. DOI: `10.1103/PhysRevLett.101.036601`. URL: `https://journals-aps-org.proxy.unimib.it/prl/abstract/10.1103/PhysRevLett.101.036601`.

[23] Luqiao Liu et al. "Spin-torque ferromagnetic resonance induced by the spin Hall effect". In: *Physical Review Letters* 106.3 (Jan. 2011), p. 036601. ISSN: 00319007. DOI: `10.1103/PhysRevLett.106.036601`. arXiv: `1011.2788`. URL: `https://journals-aps-org.proxy.unimib.it/prl/abstract/10.1103/PhysRevLett.106.036601`.

[24] M. Z. Hasan and C. L. Kane. "Colloquium: Topological insulators". In: *Reviews of Modern Physics* 82.4 (2010), pp. 3045–3067. ISSN: 00346861. DOI: `10.1103/RevModPhys.82.3045`. URL: `https://link.aps.org/doi/10.1103/RevModPhys.82.3045`.

[25] Mengyun He, Huimin Sun, and Qing Lin He. *Topological insulator: Spintronics and quantum computations.* 2019. DOI: `10.1007/s11467-019-0893-4`. URL: `http://link.springer.com/10.1007/s11467-019-0893-4`.

[26] Yoichi Ando. *Topological insulator materials.* 2013. DOI: `10.7566/JPSJ.82.102001`. arXiv: `1304.5693`. URL: `http://journals.jps.jp/doi/10.7566/JPSJ.82.102001`.

[27] Jan Seidel. *Nanoelectronics based on topological structures.* 2019. DOI: `10.1038/s41563-019-0301-z`. URL: `http://www.nature.com/articles/s41563-019-0301-z`.

[28] Joel E. Moore. *The birth of topological insulators.* 2010. DOI: `10.1038/nature08916`. URL: `http://www.nature.com/articles/nature08916`.

[29] Nguyen Huynh Duy Khang, Yugo Ueda, and Pham Nam Hai. "A conductive topological insulator with large spin Hall effect for ultralow power spin–orbit torque switching". In: *Nature Materials* 17.9 (Sept. 2018), pp. 808–813. ISSN: 14764660. DOI: `10.1038/s41563-018-0137-y`. arXiv: `1709.07684`.

[30] O. Gomonay, M. Kläui, and J. Sinova. "Manipulating antiferromagnets with magnetic fields: Ratchet motion of multiple domain walls induced by asymmetric field pulses". In: *Applied Physics Letters* 109.14 (2016). ISSN: 00036951. DOI: `10.1063/1.4964272`. arXiv: `1608.05967`. URL: `http://dx.doi.org/10.1063/1.4964272`.

[31] L. Baldrati et al. "Spin transport in multilayer systems with fully epitaxial NiO thin films". In: *Physical Review B* 98.1 (2018), p. 14409. ISSN: 24699969. DOI: `10.1103/PhysRevB.98.014409`. arXiv: `1802.01844`. URL: `https://doi.org/10.1103/PhysRevB.98.014409`.

[32] Yi Wang, Rajagopalan Ramaswamy, and Hyunsoo Yang. *FMR-related phenomena in spintronic devices.* July 2018. DOI: `10.1088/1361-6463/aac7b5`.

[33] Shuyuan Shi et al. *All-electric magnetization switching and Dzyaloshinskii–Moriya interaction in WTe2/ferromagnet heterostructures.* 2019. DOI: `10.1038/s41565-019-0525-8`. URL: `https://doi.org/10.1038/s41565-019-0525-8`.

[34] Haijun Zhang et al. "Topological insulators in Bi 2 Se 3, Bi 2 Te 3 and Sb 2 Te 3 with a single Dirac cone on the surface". In: *Nature Physics* 5.6 (June 2009), pp. 438–442. ISSN: 17452473. DOI: `10.1038/nphys1270`.

[35] Y. L. Chen et al. "Experimental realization of a three-dimensional topological insulator, Bi2Te3". In: *Science* 325.5937 (2009), pp. 178–181. ISSN: 00368075. DOI: `10.1126/science.1173034`. arXiv: `arXiv:0904.1829v1`.

[36] Y. Xia et al. “Observation of a large-gap topological-insulator class with a single Dirac cone on the surface”. In: *Nature Physics* 5.6 (2009), pp. 398–402. ISSN: 17452481. DOI: `10.1038/nphys1274`.

[37] Lee A. Walsh et al. “Interface Chemistry of Contact Metals and Ferromagnets on the Topological Insulator Bi2Se3”. In: *Journal of Physical Chemistry C* 121.42 (2017), pp. 23551–23563. ISSN: 19327455. DOI: `10.1021/acs.jpcc.7b08480`. URL: `https://pubs.acs.org/doi/10.1021/acs.jpcc.7b08480`.

[38] Hao Wu et al. “Room-Temperature Spin-Orbit Torque from Topological Surface States”. In: *Physical Review Letters* 123.20 (2019), p. 207205. ISSN: 10797114. DOI: `10.1103/PhysRevLett.123.207205`. URL: `https://doi.org/10.1103/PhysRevLett.123.207205`.

[39] N. Peranio et al. “Room-temperature MBE deposition, thermoelectric properties, and advanced structural characterization of binary Bi 2Te 3 and Sb 2Te 3 thin films”. In: *Journal of Alloys and Compounds* 521 (Apr. 2012), pp. 163–173. ISSN: 09258388. DOI: `10.1016/j.jallcom.2012.01.108`.

[40] Yi Wang et al. “Room temperature magnetization switching in topological insulator-ferromagnet heterostructures by spin-orbit torques”. In: *Nature Communications* 8.1 (Dec. 2017). ISSN: 20411723. DOI: `10.1038/s41467-017-01583-4`.

[41] Jörn Kampmeier et al. “Selective area growth of Bi2Te3 and Sb2Te3 topological insulator thin films”. In: *Journal of Crystal Growth* 443 (June 2016), pp. 38–42. ISSN: 00220248. DOI: `10.1016/j.jcrysgro.2016.03.012`.

[42] Martino Rimoldi et al. “Epitaxial and large area Sb2Te3thin films on silicon by MOCVD”. In: *RSC Advances* 10.34 (2020), pp. 19936–19942. ISSN: 20462069. DOI: `10.1039/d0ra02567d`. URL: `http://xlink.rsc.org/?DOI=D0RA02567D`.

[43] H. C.M. Knoops et al. “Atomic Layer Deposition”. In: *Handbook of Crystal Growth: Thin Films and Epitaxy: Second Edition.* Ed. by T Kuech. Vol. 3. Netherlands: Elsevier, 2015, pp. 1101–1134. ISBN: 9780444633057. DOI: `10.1016/B978-0-444-63304-0.00027-5`.

[44] Emanuele Longo et al. “ALD growth of ultra-thin Co layers on the topological insulator Sb2Te3”. In: *Nano Research* 13.2 (2020), pp. 570–575. ISSN: 19980000. DOI: `10.1007/s12274-020-2657-4`.

[45] R. Mantovan et al. “Fe3-δO4/MgO/Co magnetic tunnel junctions synthesized by full in situ atomic layer and chemical vapour deposition”. In: *Journal of Physics D: Applied Physics* 47.10 (2014), p. 102002. ISSN: 00223727. DOI: `10.1088/0022-3727/47/10/102002`. URL: `http://stacks.iop.org/0022-3727/47/i=10/a=102002?key=crossref.6202386c7faecd218457a199ca6b7e9e`.

[46] Marie Blandine Martin et al. “Sub-nanometer atomic layer deposition for spintronics in magnetic tunnel junctions based on graphene spin-filtering membranes”. In: *ACS Nano* 8.8 (Aug. 2014), pp. 7890–7895. ISSN: 1936086X. DOI: `10.1021/nn5017549`.

[47] Ivan S. Maksymov and Mikhail Kostylev. *Broadband stripline ferromagnetic resonance spectroscopy of ferromagnetic films, multilayers and nanostructures.* May 2015. DOI: `10.1016/j.physe.2014.12.027`.

[48] Ken Ichi Uchida et al. “Observation of longitudinal spin-Seebeck effect in magnetic insulators”. In: *Applied Physics Letters* 97.17 (2010). ISSN: 00036951. DOI: `10.1063/1.3507386`.

[49] J. C. Rojas-Sánchez et al. “Spin to Charge Conversion at Room Temperature by Spin Pumping into a New Type of Topological Insulator: α -Sn Films”. In: *Physical Review Letters* 116.9 (Mar. 2016). ISSN: 10797114. DOI: `10.1103/PhysRevLett.116.096602`.

[50] J. C.Rojas Sánchez et al. “Spin-to-charge conversion using Rashba coupling at the interface between non-magnetic materials”. In: *Nature Communications* 4 (2013), pp. 1–7. ISSN: 20411723. DOI: `10.1038/ncomms3944`.

[51] V. M. Edelstein. “Spin polarization of conduction electrons induced by electric current in two-dimensional asymmetric electron systems”. In: *Solid State Communications* 73.3 (1990), pp. 233–235. ISSN: 00381098. DOI: `10.1016/0038-1098(90)90963-C`.

[52] Mahdi Jamali et al. “Giant Spin Pumping and Inverse Spin Hall Effect in the Presence of Surface and Bulk Spin-Orbit Coupling of Topological Insulator Bi2Se3”. In: *Nano Letters* 15.10 (2015), pp. 7126–7132. ISSN: 15306992. DOI: `10.1021/acs.nanolett.5b03274`. URL: `https://pubs.acs.org/sharingguidelines`.

[53] Mahendra Dc et al. “Room-temperature spin-to-charge conversion in sputtered bismuth selenide thin films via spin pumping from yttrium iron garnet”. In: *Applied Physics Letters* 114.10 (2019). ISSN: 00036951. DOI: `10.1063/1.5054806`. URL: `http://dx.doi.org/10.1063/1.5054806`.

[54] Lijun Zhu, Daniel C. Ralph, and Robert A. Buhrman. “Effective Spin-Mixing Conductance of Heavy-Metal-Ferromagnet Interfaces”. In: *Physical Review Letters* 123.5 (Aug. 2019), p. 57203. ISSN: 10797114. DOI: `10.1103/PhysRevLett.123.057203`. arXiv: `1905.01577`. URL: `https://link.aps.org/doi/10.1103/PhysRevLett.123.057203`.

[55] B. L. Zink et al. “Efficient spin transport through native oxides of nickel and permalloy with platinum and gold overlayers”. In: *Physical Review B* 93.18 (May 2016). ISSN: 24699969. DOI: `10.1103/PhysRevB.93.184401`.

[56] Weifeng Zhang et al. “Role of transparency of platinum-ferromagnet interfaces in determining the intrinsic magnitude of the spin Hall effect”. In: *Nature Physics* 11.6 (2015), pp. 496–502. ISSN: 17452481. DOI: `10.1038/nphys3304`.

[57] K. Kondou et al. “Fermi-level-dependent charge-to-spin current conversion by Dirac surface states of topological insulators”. In: *Nature Physics* 12.11 (Nov. 2016), pp. 1027–1031. ISSN: 17452481. DOI: `10.1038/nphys3833`.

[58] J. B.S. Mendes et al. “Dirac-surface-state-dominated spin to charge current conversion in the topological insulator (Bi 0.22 Sb 0.78) 2 Te 3 films at room temperature”. In: *Physical Review B* 96.18 (2017), pp. 1–7. ISSN: 24699969. DOI: `10.1103/PhysRevB.96.180415`.

[59] J. B.S. Mendes et al. “Efficient spin to charge current conversion in the 2D semiconductor MoS2 by spin pumping from yttrium iron garnet”. In: *Applied Physics Letters* 112.24 (2018). ISSN: 00036951. DOI: `10.1063/1.5030643`. URL: `http://dx.doi.org/10.1063/1.5030643`.

[60] Frédéric Bonell et al. “Control of Spin-Orbit Torques by Interface Engineering in Topological Insulator Heterostructures”. In: *Nano Letters* 20.8 (2020), pp. 5893–5899. ISSN: 15306992. DOI: `10.1021/acs.nanolett.0c01850`. arXiv: `2009.08215`.

[61] Haijun Zhang et al. “Topological insulators in Bi 2 Se 3, Bi 2 Te 3 and Sb 2 Te 3 with a single Dirac cone on the surface”. In: *Nature Physics* 5.6 (June 2009), pp. 438–442. ISSN: 17452473. DOI: `10.1038/nphys1270`.

[62] Marissa M. Kerrigan, Joseph P. Klesko, and Charles H. Winter. “Low Temperature, Selective Atomic Layer Deposition of Cobalt Metal Films Using Bis(1,4-di-tert-butyl-1,3-diazadienyl)cobalt and Alkylamine Precursors”. In: *Chemistry of Materials* 29.17 (2017), pp. 7458–7466. ISSN: 15205002. DOI: `10.1021/acs.chemmater.7b02456`. URL: `https://pubs.acs.org/doi/10.1021/acs.chemmater.7b02456`.

[63] Mikhail Chubarov et al. “In-plane x-ray diffraction for characterization of monolayer and few-layer transition metal dichalcogenide films”. In: *Nanotechnology* 29.5 (2018). ISSN: 13616528. DOI: `10.1088/1361-6528/aaa1bd`.

[64] Jean Daillant and Alain Gibaud, eds. *X-Ray and Neutron Reflectivity: Principles and Applications (Lecture Notes in Physics Monographs)*. Lecture notes in physics N.s. M, Monographs 58. Springer, 1999, p. 331. ISBN: 3540661956. URL: `http://www.amazon.com/X-Ray-Neutron-Reflectivity-Principles-Applications/dp/3540661956`.

[65] J. Als-Nielsen and D. McMorrow. *Elements of modern X-ray physics*. Vol. 55. 3. 2002, p. 63. ISBN: 9780470973950. DOI: `10.1063/1.1472397`.

[66] L. LANDAU and E. LIFSHITZ. “On the theory of the dispersion of magnetic permeability in ferromagnetic bodies”. In: *Perspectives in Theoretical Physics*. Ed. by L P PITAEVSKI. Amsterdam: Pergamon, 1992, pp. 51–65. ISBN: 978-0-08-036364-6. DOI: `10.1016/b978-0-08-036364-6.50008-9`. URL: `http://www.sciencedirect.com/science/article/pii/B9780080363646500089`.

[67] N W Ashcroft and N D Mermin. *{S}olid {S}tate {P}hysics*. Holt-Saunders, 1976.

[68] Michael Farle. “Ferromagnetic resonance of ultrathin metallic layers”. In: *Reports on Progress in Physics* 61.7 (July 1998), pp. 755–826. ISSN: 00344885. DOI: `10.1088/0034-4885/61/7/001`.

[69] Z. Celinski, K. B. Urquhart, and B. Heinrich. "Using ferromagnetic resonance to measure the magnetic moments of ultrathin films". In: *Journal of Magnetism and Magnetic Materials* 166.1-2 (1997), pp. 6–26. ISSN: 03048853. DOI: `10.1016/S0304-8853(96)00428-3`.

[70] Michael Feld et al. "Observation of a pairing pseudogap in a two-dimensional Fermi gas". In: *Nature* 480.7375 (2011), pp. 75–78. ISSN: 00280836. DOI: `10.1038/nature10627`. arXiv: `1110.2418`. URL: `http://epub.uni-regensburg.de/14960/1/Woltersdorf-PhD04.pdf`.

[71] Benjamin Buford, Pallavi Dhagat, and Albrecht Jander. "A technique for error estimation of linewidth and damping parameters extracted from ferromagnetic resonance measurements". In: *Journal of Applied Physics* 117.17 (May 2015), 17E109. ISSN: 10897550. DOI: `10.1063/1.4908301`.

[72] Kai Chen and Shufeng Zhang. "Spin pumping in the presence of spin-orbit coupling". In: *Physical Review Letters* 114.12 (Mar. 2015). ISSN: 10797114. DOI: `10.1103/PhysRevLett.114.126602`.

[73] D. C. Ralph and M. D. Stiles. "Spin transfer torques". In: *Journal of Magnetism and Magnetic Materials* 320.7 (2008), pp. 1190–1216. ISSN: 03048853. DOI: `10.1016/j.jmmm.2007.12.019`. arXiv: `0711.4608`.

[74] Mark H. Fischer et al. "Spin-torque generation in topological insulator based heterostructures". In: *Physical Review B* 93.12 (Mar. 2016), p. 125303. ISSN: 24699969. DOI: `10.1103/PhysRevB.93.125303`. arXiv: `1305.1328`.

[75] Yi Wang et al. "Topological surface states originated spin-orbit torques in Bi2Se3". In: *Physical Review Letters* 114.25 (2015), p. 257202. ISSN: 10797114. DOI: `10.1103/PhysRevLett.114.257202`. URL: `https://link.aps.org/doi/10.1103/PhysRevLett.114.257202`.

[76] Bo Han et al. "Determination of the Spin-Orbit Torques in Ferromagnetic-Heavy-Metal Bilayers Using Harmonic Longitudinal Voltage Measurements". In: *Physical Review Applied* 13.1 (2020), p. 1. ISSN: 23317019. DOI: `10.1103/PhysRevApplied.13.014065`. URL: `https://doi.org/10.1103/PhysRevApplied.13.014065`.

[77] Yaroslav Tserkovnyak, Arne Brataas, and Gerrit E.W. Bauer. “Enhanced Gilbert Damping in Thin Ferromagnetic Films”. In: *Physical Review Letters* 88.11 (2002), p. 4. ISSN: 10797114. DOI: `10.1103/PhysRevLett.88.117601`. arXiv: `0110247 [cond-mat]`.

[78] Yaroslav Tserkovnyak, Arne Brataas, and Gerrit E.W. Bauer. “Spin pumping and magnetization dynamics in metallic multilayers”. In: *Physical Review B - Condensed Matter and Materials Physics* 66.22 (2002), pp. 1–10. ISSN: 1550235X. DOI: `10.1103/PhysRevB.66.224403`. arXiv: `0208091 [cond-mat]`.

[79] S. Mizukami, Y. Ando, and T. Miyazaki. “The study on ferromagnetic resonance linewidth for NM/80NiFe/NM (NM = Cu, Ta, Pd and Pt) films”. In: *Japanese Journal of Applied Physics, Part 1: Regular Papers and Short Notes and Review Papers* 40.2 A (2001), pp. 580–585. ISSN: 00214922. DOI: `10.1143/jjap.40.580`. URL: `https://iopscience.iop.org/article/10.1143/JJAP.40.580`.

[80] J. C.Rojas Sánchez et al. “Spin-to-charge conversion using Rashba coupling at the interface between non-magnetic materials”. In: *Nature Communications* 4 (2013), pp. 1–7. ISSN: 20411723. DOI: `10.1038/ncomms3944`.

[81] Mahendra Dc et al. “Observation of High Spin-to-Charge Conversion by Sputtered Bismuth Selenide Thin Films at Room Temperature”. In: *Nano Letters* 19.8 (2019), pp. 4836–4844. ISSN: 15306992. DOI: `10.1021/acs.nanolett.8b05011`.

[82] O. Mosendz et al. “Quantifying spin hall angles from spin pumping: Experiments and theory”. In: *Physical Review Letters* 104.4 (2010), pp. 1–4. ISSN: 00319007. DOI: `10.1103/PhysRevLett.104.046601`. arXiv: `0911.2725`.

[83] M. I. Dyakonov and V. I. Perel. “Current-induced spin orientation of electrons in semiconductors”. In: *Physics Letters A* 35.6 (1971), pp. 459–460. ISSN: 03759601. DOI: `10.1016/0375-9601(71)90196-4`.

[84] Jairo Sinova et al. “Universal intrinsic spin Hall effect”. In: *Physical Review Letters* 92.12 (2004), pp. 1–4. ISSN: 00319007. DOI: `10.1103/PhysRevLett.92.126603`. arXiv: `0307663 [cond-mat]`.

[85] Ka Shen, G. Vignale, and R. Raimondi. “Microscopic theory of the inverse Edelstein effect”. In: *Physical Review Letters* 112.9 (2014), pp. 1–5. ISSN: 10797114. DOI: `10.1103/PhysRevLett.112.096601`.

[86] Y. K. Kato et al. “Current-induced spin polarization in strained semiconductors”. In: *Physical Review Letters* 93.17 (2004), pp. 8–11. ISSN: 00319007. DOI: `10.1103/PhysRevLett.93.176601`.

[87] A. Yu Silov et al. “Current-induced spin polarization at a single heterojunction”. In: *Applied Physics Letters* 85.24 (2004), pp. 5929–5931. ISSN: 00036951. DOI: `10.1063/1.1833565`.

[88] Yu. A. Bychkov and E. I. Rashba. *Properties of a 2D electron gas with lifted spectral degeneracy.* 1984.

[89] C. Gorini et al. “Non-Abelian gauge fields in the gradient expansion: Generalized Boltzmann and Eilenberger equations”. In: *Physical Review B - Condensed Matter and Materials Physics* 82.19 (2010), pp. 1–11. ISSN: 10980121. DOI: `10.1103/PhysRevB.82.195316`. arXiv: `1003.5763`.

[90] H T C Threshold. “Spin-galvanic effect”. In: 417.May (2002), pp. 153–156. DOI: `10.1038/nature747.1.`.

[91] Christian R. Ast et al. “Giant spin splitting through surface alloying”. In: *Physical Review Letters* 98.18 (May 2007). ISSN: 10797114. DOI: `10.1103/PhysRevLett.98.186807`.

[92] S. Zhang and A. Fert. “Conversion between spin and charge currents with topological insulators”. In: *Physical Review B* 94.18 (2016), pp. 1–5. ISSN: 24699969. DOI: `10.1103/PhysRevB.94.184423`.

[93] Yi Wang et al. “Determination of intrinsic spin Hall angle in Pt”. In: *Applied Physics Letters* 105.15 (Oct. 2014), p. 152412. ISSN: 00036951. DOI: `10.1063/1.4898593`.

[94] Praveen Deorani et al. “Observation of inverse spin hall effect in bismuth selenide”. In: *Physical Review B - Condensed Matter and Materials Physics* 90.9 (2014), p. 94403. ISSN: 1550235X. DOI: `10.1103/PhysRevB.90.094403`.

[95] Shigeru Suzuki, Yohei Takahashi, and Yoshio Waseda. “A feasible SIMS study for characterizing ferric oxyhydroxides formed on the iron surface using deuterium”. In: *Materials Transactions* 44.7 (2003), pp. 1400–1404. ISSN: 13459678. DOI: `10.2320/matertrans.44.1400`.

[96] Silvia Tacchi et al. “Angular dependence of magnetic normal modes in NiFe antidot lattices with different lattice symmetry”. In: *IEEE Transactions on Magnetics*. Vol. 46. 6. June 2010, pp. 1440–1443. DOI: `10.1109/TMAG.2009.2039775`.

[97] Giovanni Carlotti and Gianluca Gubbiotti. “Magnetic properties of layered nanostructures studied by means of Brillouin light scattering and the surface magneto-optical Kerr effect”. In: *Journal of Physics Condensed Matter* 14.35 (2002), pp. 8199–8233. ISSN: 09538984. DOI: `10.1088/0953-8984/14/35/303`.

[98] H. P. Gunnlaugsson. “Spreadsheet based analysis of Mössbauer spectra”. In: *Hyperfine Interactions* 237.1 (2016), pp. 13–18. ISSN: 15729540. DOI: `10.1007/s10751-016-1271-z`.

[99] R. Mantovan et al. “Mössbauer spectroscopy study of interfaces for spintronics”. In: *Hyperfine Interactions* 191.1-3 (2009), pp. 41–46. ISSN: 03043843. DOI: `10.1007/s10751-009-9982-z`.

[100] R. Mantovan et al. “CEMS characterisation of Fe/high-κ oxide interfaces”. In: *Hyperfine Interactions* 169.1-3 (2006), pp. 1349–1353. ISSN: 03043843. DOI: `10.1007/s10751-006-9449-4`.

[101] A. Zenkevich et al. “Fe/BaTiO3 interface: Band alignment and chemical properties”. In: *Applied Physics Letters* 99.18 (Oct. 2011), p. 182905. ISSN: 00036951. DOI: `10.1063/1.3657769`. URL: `http://aip.scitation.org/doi/10.1063/1.3657769`.

[102] E. Longo et al. “Chemical, structural and magnetic properties of the Fe/Sb2Te3 interface”. In: *Journal of Magnetism and Magnetic Materials* 474 (2019), pp. 632–636. ISSN: 03048853. DOI: `10.1016/j.jmmm.2018.12.009`.

[103] Emanuele Longo et al. “Fe/Sb2Te3 Interface Reconstruction through Mild Thermal Annealing”. In: *Advanced Materials Interfaces* 7.19 (2020), p. 2000905. ISSN: 21967350. DOI: `10.1002/admi.202000905`. URL: `https://onlinelibrary.wiley.com/doi/abs/10.1002/admi.202000905`.

[104] Raimondo Cecchini et al. *Weak Antilocalization in Granular Sb2Te3 Thin Films Deposited by MOCVD*. 2018. DOI: `10.1002/pssr.201800155`. URL: `http://doi.wiley.com/10.1002/pssr.201800155`.

[105] J. B. Ward and V. H. McCann. “On the 57Fe Mossbauer spectra of FeTe and Fe2Te 3”. In: *Journal of Physics C: Solid State Physics* 12.5 (1979), pp. 873–879. ISSN: 00223719. DOI: `10.1088/0022-3719/12/5/016`.

[106] Y. Mizuguchi et al. “FeTe as a candidate material for new iron-based superconductor”. In: *Physica C: Superconductivity and its Applications* 469.15-20 (Oct. 2009), pp. 1027–1029. ISSN: 09214534. DOI: `10.1016/j.physc.2009.05.177`.

[107] Jacek Gurgul et al. “Layer-by-layer epitaxial growth of polar FeO(111) thin films on MgO(111)”. In: *Surface Science* 606.7-8 (2012), pp. 711–714. ISSN: 00396028. DOI: `10.1016/j.susc.2011.12.012`.

[108] J. Steger and E. Kostiner. “Mössbauer effect study of FeSb2”. In: *Journal of Solid State Chemistry* 5.1 (1972), pp. 131–135. ISSN: 1095726X. DOI: `10.1016/0022-4596(72)90020-5`.

[109] Sarmita Majumder et al. “Interfacial reactions at Fe/topological insulator spin contacts”. In: *Journal of Vacuum Science & Technology B, Nanotechnology and Microelectronics: Materials, Processing, Measurement, and Phenomena* 35.4 (July 2017), 04F105. ISSN: 2166-2746. DOI: `10.1116/1.4991331`.

[110] Hongyu An et al. “Giant spin-torque generation by heavily oxidized Pt”. In: *Physical Review B* 98.1 (2018), pp. 1–5. ISSN: 24699969. DOI: `10.1103/PhysRevB.98.014401`.

[111] A. Ruiz-Calaforra et al. “The role of the non-magnetic material in spin pumping and magnetization dynamics in NiFe and CoFeB multilayer systems”. In: *Journal of Applied Physics* 117.16 (2015). ISSN: 10897550. DOI: `10.1063/1.4918909`. URL: `http://dx.doi.org/10.1063/1.4918909`.

[112] S. Manna et al. “Interfacial superconductivity in a bi-collinear antiferromagnetically ordered FeTe monolayer on a topological insulator”. In: *Nature Communications* 8.1 (Apr. 2017), p. 14074. ISSN: 20411723. DOI: `10.1038/ncomms14074`. arXiv: `1606.03249`.

[113] Qing Lin He et al. “Two-dimensional superconductivity at the interface of a Bi2 Te3 /FeTe heterostructure”. In: *Nature Communications* 5.1 (Sept. 2014), p. 4247. ISSN: 20411723. DOI: `10.1038/ncomms5247`.

[114] Ivana Vobornik et al. “Observation of distinct bulk and surface chemical environments in a topological insulator under magnetic doping”. In: *Journal of Physical Chemistry C* 118.23 (June 2014), pp. 12333–12339. ISSN: 19327455. DOI: `10.1021/jp502729u`.

[115] Marissa M. Kerrigan et al. “Substrate selectivity in the low temperature atomic layer deposition of cobalt metal films from bis(1,4-di- tert -butyl-1,3-diazadienyl)cobalt and formic acid”. In: *Journal of Chemical Physics* 146.5 (2017), p. 52813. ISSN: 00219606. DOI: `10.1063/1.4968848`. URL: `http://aip.scitation.org/doi/10.1063/1.4968848`.

[116] Joseph P. Klesko, Marissa M. Kerrigan, and Charles H. Winter. “Low Temperature Thermal Atomic Layer Deposition of Cobalt Metal Films”. In: *Chemistry of Materials* 28.3 (2016), pp. 700–703. ISSN: 15205002. DOI: `10.1021/acs.chemmater.5b03504`. URL: `https://pubs.acs.org/doi/10.1021/acs.chemmater.5b03504`.

[117] A. Taylor and R. W. Floyd. “Precision measurements of lattice parameters of non-cubic crystals”. In: *Acta Crystallographica* 3.4 (July 1950), pp. 285–289. ISSN: 0365-110X. DOI: `10.1107/s0365110x50000732`. URL: `https://doi.org/10.1107/S0365110X50000732`.

[118] A. Lamperti et al. “Interface width evaluation in thin layered CoFeB/MgO multilayers including Ru or Ta buffer layer by X-ray reflectivity”. In: *Thin Solid Films* 533 (2013), pp. 79–82. ISSN: 00406090. DOI: `10.1016/j.tsf.2012.11.130`. URL: `http://www.sciencedirect.com/science/article/pii/S0040609012016318`.

[119] L. K. Ono et al. “Formation and thermal stability of platinum oxides on size-selected platinum nanoparticles: Support effects”. In: *Journal of Physical Chemistry C* 114.50 (2010), pp. 22119–22133. ISSN: 19327447. DOI: `10.1021/jp1086703`.

[120] E. Dynowska et al. “Structural investigation of ultrathin Pt/Co/Pt trilayer films under EUV irradiation”. In: *Nuclear Instruments and Methods in Physics Research, Section B: Beam Interactions with Materials and Atoms* 364 (2015), pp. 33–39. ISSN: 0168583X. DOI: `10.1016/j.nimb.2015.07.116`. URL: `http://www.sciencedirect.com/science/article/pii/S0168583X15007053`.

[121] M Singh. “High-Temperature X-Ray Diffraction Study on Co7BSnss Alloy”. In: 165 (1985), pp. 165–168.

[122] Alberto Debernardi, Claudia Wiemer, and Marco Fanciulli. “Epitaxial phase of hafnium dioxide for ultrascaled electronics”. In: *Physical Review B - Condensed Matter and Materials Physics* 76.15 (2007), pp. 1–7. ISSN: 10980121. DOI: `10.1103/PhysRevB.76.155405`.

[123] Annelies Delabie et al. “Atomic layer deposition of hafnium oxide on germanium substrates”. In: *Journal of Applied Physics* 97.6 (2005). ISSN: 00218979. DOI: `10.1063/1.1856221`.

[124] Mitsuru Ohtake et al. “Preparation and characterization of Co single-crystal thin films with hcp, fcc and bcc structures”. In: *Journal of Applied Physics* 109.7 (2011). ISSN: 00218979. DOI: `10.1063/1.3537817`.

[125] Abhishek Banerjee et al. “Granular topological insulators”. In: *Nanoscale* 9.20 (2017), pp. 6755–6764. ISSN: 20403372. DOI: `10.1039/c7nr01355h`. arXiv: `1604.03767`.

[126] P. I. Kuznetsov et al. “MOVPE deposition of Sb2Te3 and other phases of Sb-Te system on sapphire substrate”. In: *Journal of Crystal Growth* 471 (2017), pp. 1–7. ISSN: 00220248. DOI: `10.1016/j.jcrysgro.2017.05.002`. URL: `http://www.sciencedirect.com/science/article/pii/S0022024817303226`.

[127] A. Giani et al. “Growth of Bi2Te3 and Sb2Te3 thin films by MOCVD”. In: *Materials Science and Engineering B: Solid-State Materials for Advanced Technology* 64.1 (1999), pp. 19–24. ISSN: 09215107. DOI: `10.1016/S0921-5107(99)00142-7`. URL: `http://www.sciencedirect.com/science/article/pii/S0921510799001427`.

[128] David Nminibapiel et al. “ Growth of Nanolaminates of Thermoelectric Bi 2 Te 3 /Sb 2 Te 3 by Atomic Layer Deposition ”. In: *ECS Journal of Solid State Science and Technology* 3.4 (2014), P95–P100. ISSN: 2162-8769. DOI: `10.1149/2.014404jss`.

[129] Georg Bendt et al. “Structural and thermoelectrical characterization of epitaxial Sb2Te3 high quality thin films grown by thermal evaporation”. In: *Semiconductor Science and Technology* 33.10 (Aug. 2018), p. 105002. ISSN: 13616641. DOI: `10.1088/1361-6641/aad7a3`. URL: `https://doi.org/10.1088%7B%5C%%7D2F1361-6641%7B%5C%%7D2Faad7a3`.

[130] F. Rieger et al. “Transition into a phonon glass in crystalline thermoelectric (S b1-x B ix)2 T e3 films”. In: *Physical Review Materials* 4.2 (Feb. 2020), p. 25402. ISSN: 24759953. DOI: `10.1103/PhysRevMaterials.4.025402`. URL: `https://link.aps.org/doi/10.1103/PhysRevMaterials.4.025402`.

[131] Frédéric Bonell et al. “Growth of Twin-Free and Low-Doped Topological Insulators on BaF2(111)”. In: *Crystal Growth and Design* 17.9 (2017), pp. 4655–4660. ISSN: 15287505. DOI: `10.1021/acs.cgd.7b00525`. URL: `https://pubs.acs.org/doi/10.1021/acs.cgd.7b00525`.

[132] Hong Jun Gao et al. “Toward a detailed understanding of Si(111)- 7×7 surface and adsorbed ge nanostructures: Fabrications, structures, and calculations”. In: *Journal of Nanomaterials* 2008.1 (2008). ISSN: 16874110. DOI: `10.1155/2008/874213`.

[133] C. Chappert et al. “Ferromagnetic resonance studies of very thin cobalt films on a gold substrate”. In: *Physical Review B* 34.5 (Sept. 1986), pp. 3192–3197. ISSN: 01631829. DOI: `10.1103/PhysRevB.34.3192`.

[134] A. Ghosh et al. “Dependence of nonlocal Gilbert damping on the ferromagnetic layer type in ferromagnet/Cu/Pt heterostructures”. In: *Applied Physics Letters* 98.5 (Jan. 2011), p. 52508. ISSN: 00036951. DOI: `10.1063/1.3551729`. arXiv: `1011.5868`.

[135] Emanuele Longo et al. “Ferromagnetic resonance of Co thin films grown by atomic layer deposition on the Sb2Te3 topological insulator”. In: *Journal of Magnetism and Magnetic Materials* 509 (Sept. 2020), p. 166885. ISSN: 03048853. DOI: `10.1016/j.jmmm.2020.166885`.

[136] M. Tokaç et al. “Interfacial Structure Dependent Spin Mixing Conductance in Cobalt Thin Films”. In: *Physical Review Letters* 115.5 (July 2015). ISSN: 10797114. DOI: `10.1103/PhysRevLett.115.056601`.

[137] G. R. Harp et al. “Unusual stability of fcc Co(110)/Cu(110)”. In: *Physical Review B* 48.23 (Dec. 1993), pp. 17538–17544. ISSN: 01631829. DOI: `10.1103/PhysRevB.48.17538`.

[138] B. Heinrich, J. F. Cochran, and R. Hasegawa. “FMR linebroadening in metals due to two-magnon scattering”. In: *Journal of Applied Physics* 57.8 (1985), pp. 3690–3692. ISSN: 00218979. DOI: `10.1063/1.334991`.

[139] C. Wiemer et al. “Combining grazing incidence X-ray diffraction and X-ray reflectivity for the evaluation of the structural evolution of HfO2 thin films with annealing”. In: *Thin Solid Films*. Vol. 450. 1. Feb. 2004, pp. 134–137. DOI: `10.1016/j.tsf.2003.10.057`.

[140] D. Weller et al. “Orientation dependence of the polar Kerr effect in fcc and hcp Co”. In: *Physical Review Letters* 72.13 (Mar. 1994), pp. 2097–2100. ISSN: 00319007. DOI: `10.1103/PhysRevLett.72.2097`.

[141] Akira Yoshihara et al. “Brillouin light scattering from spin waves in epitaxial hcp Co films”. In: *Physical Review B - Condensed Matter and Materials Physics* 67.13 (Apr. 2003). ISSN: 1550235X. DOI: `10.1103/PhysRevB.67.134435`.

[142] J. M.L. Beaujour et al. “Ferromagnetic resonance study of polycrystalline cobalt ultrathin films”. In: *Journal of Applied Physics* 99.8 (2006), pp. 3–5. ISSN: 00218979. DOI: `10.1063/1.2151832`. arXiv: `0509036 [cond-mat]`.

[143] T. G.A. Verhagen et al. “Temperature dependence of spin pumping and Gilbert damping in thin Co/Pt bilayers”. In: *Journal of Physics Condensed Matter* 28.5 (Feb. 2016), p. 56004. ISSN: 1361648X. DOI: `10.1088/0953-8984/28/5/056004`.

[144] M. J. Hurben and C. E. Patton. “Theory of two magnon scattering microwave relaxation and ferromagnetic resonance linewidth in magnetic thin films”. In: *Journal of Applied Physics* 83.8 (1998), pp. 4344–4365. ISSN: 00218979. DOI: `10.1063/1.367194`.

[145] J. Lindner et al. “Two-magnon damping in thin films in case of canted magnetization: Theory versus experiment”. In: *Physical Review B - Condensed Matter and Materials Physics* 80.22 (2009), p. 224421. ISSN: 10980121. DOI: `10.1103/PhysRevB.80.224421`. URL: `https://link.aps.org/doi/10.1103/PhysRevB.80.224421`.

[146] Sheng Jiang et al. “Ferromagnetic resonance linewidth and two-magnon scattering in Fe1-xGdx thin films”. In: *AIP Advances* 7.5 (May 2017), p. 56029. ISSN: 21583226. DOI: `10.1063/1.4978004`.

[147] Antonio Azevedo et al. “Extrinsic contributions to spin-wave damping and renormalization in thin <math display="inline"> <mrow> <msub> <mrow> <mi mathvariant="normal">Ni</mi> </mrow> <mrow> <mn>50</mn> </mrow> </msub> </mrow> <mrow> <msub> <mrow> <mi mathvariant="normal">Fe</mi>”. In: *Physical Review B* 62.9 (2000), pp. 5331–5333. ISSN: 0163-1829. URL: `http://link.aps.org/doi/10.1103/PhysRevB.62.5331`.

[148] Li Zhou et al. “Synthesis and Evaluation of Magnetic Thin Films”. In: *IEEE Transactions on Magnetics* 29.6 (Nov. 1993), pp. 3052–3054. ISSN: 19410069. DOI: `10.1109/20.281114`.

[149] A. K. Kaveev et al. “Band gap opening at the Dirac point in co/bisbtese2(0001) system”. In: *arXiv* 2.0001 (2019), pp. 2–7.

[150] A. K. Kaveev et al. “Energy-Gap Opening Near the Dirac Point after the Deposition of Cobalt on the (0001) Surface of the Topological Insulator BiSbTeSe2”. In: *Semiconductors* 54.9 (2020), pp. 1051–1055. ISSN: 10906479. DOI: `10.1134/S1063782620090146`.

[151] Yaroslav Tserkovnyak et al. “Nonlocal magnetization dynamics in ferromagnetic heterostructures”. In: *Reviews of Modern Physics* 77.4 (2005), pp. 1375–1421. ISSN: 00346861. DOI: `10.1103/RevModPhys.77.1375`. arXiv: `0409242 [cond-mat]`.

[152] Miren Isasa et al. “Temperature dependence of spin diffusion length and spin Hall angle in Au and Pt”. In: *Physical Review B - Condensed Matter and Materials Physics* 91.2 (2015), pp. 1–7. ISSN: 1550235X. DOI: `10.1103/PhysRevB.91.024402`.

[153] G. Zahnd et al. “Spin diffusion length and polarization of ferromagnetic metals measured by the spin-absorption technique in lateral spin valves”. In: *Physical Review B* 98.17 (2018), p. 174414. ISSN: 24699969. DOI: `10.1103/PhysRevB.98.174414`. URL: `https://doi.org/10.1103/PhysRevB.98.174414`.

[154] Z. Feng et al. “Spin Hall angle quantification from spin pumping and microwave photoresistance”. In: *Physical Review B - Condensed Matter and Materials Physics* 85.21 (2012), pp. 1–7. ISSN: 10980121. DOI: `10.1103/PhysRevB.85.214423`.

[155] Yeping Jiang et al. “Landau quantization and the thickness limit of topological insulator thin films of Sb 2Te 3”. In: *Physical Review Letters* 108.1 (2012), pp. 2–6. ISSN: 00319007. DOI: `10.1103/PhysRevLett.108.016401`.

[156] Jack Bass and William P. Pratt. “Spin-diffusion lengths in metals and alloys, and spin-flipping at metal/metal interfaces: An experimentalist’s critical review”. In: *Journal of Physics Condensed Matter* 19.18 (2007). ISSN: 09538984. DOI: `10.1088/0953-8984/19/18/183201`.

[157] Praveen Deorani et al. “Observation of inverse spin hall effect in bismuth selenide”. In: *Physical Review B - Condensed Matter and Materials Physics* 90.9 (Sept. 2014). ISSN: 1550235X. DOI: `10.1103/PhysRevB.90.094403`.

[158] Jiahao Han et al. “Roomerature Spin-Orbit Torque Switching Induced by a Topological Insulator”. In: *Physical Review Letters* 119.7 (2017), pp. 1–5. ISSN: 10797114. DOI: `10.1103/PhysRevLett.119.077702`. arXiv: `1703.07470`.